Immersogeometric cardiovascular fluid–structure interaction analysis with divergence-conforming B-splines

David Kamensky[a,*], Ming-Chen Hsu[b], Yue Yu[c], John A. Evans[d], Michael S. Sacks[a],
Thomas J. R. Hughes[a]

[a] *Center for Cardiovascular Simulation, Institute for Computational Engineering and Sciences, The University of Texas at Austin, 201 East 24th St, Stop C0200, Austin, TX 78712, USA*
[b] *Department of Mechanical Engineering, Iowa State University, 2025 Black Engineering, Ames, IA 50011, USA*
[c] *Department of Mathematics, Lehigh University, Christmas–Saucon Hall, 14 E. Packer Ave, Bethlehem, PA 18015, USA*
[d] *Department of Aerospace Engineering Sciences, University of Colorado at Boulder, 429 UCB, Boulder, CO 80309, USA*

Abstract

This paper uses a divergence-conforming B-spline fluid discretization to address the long-standing issue of poor mass conservation in immersed methods for computational fluid–structure interaction (FSI) that represent the influence of the structure as a forcing term in the fluid subproblem. We focus, in particular, on the immersogeometric method developed in our earlier work, analyze its convergence for linear model problems, then apply it to FSI analysis of heart valves, using divergence-conforming B-splines to discretize the fluid subproblem. Poor mass conservation can manifest as effective leakage of fluid through thin solid barriers. This leakage disrupts the qualitative behavior of FSI systems such as heart valves, which exist specifically to block flow. Divergence-conforming discretizations can enforce mass conservation exactly, avoiding this problem. To demonstrate the practical utility of immersogeometric FSI analysis with divergence-conforming B-splines, we use the methods described in this paper to construct and evaluate a computational model of an *in vitro* experiment that pumps water through an artificial valve.

Keywords: Fluid–structure interaction; Bioprosthetic heart valve; Immersogeometric analysis; Isogeometric analysis; Divergence-conforming B-splines; Immersed boundary method

---

Contents

1 Introduction **3**

2 Mathematical model and immersogeometric discretization of FSI **6**

---

[*] Corresponding author
Email address: `kamensky@ices.utexas.edu` (David Kamensky)

The final publication is available at Elsevier via http://dx.doi.org/10.1016/j.cma.2016.07.028

2.1 A mathematical model of fluid–thin structure interaction 6
    2.1.1 Augmented Lagrangian formulation of FSI 6
    2.1.2 Fluid subproblem 7
    2.1.3 Thin structure subproblem 8
2.2 Divergence-conforming B-spline discretization of the fluid subproblem 11
    2.2.1 Construction for rectangular domains 12
    2.2.2 Generalization to non-rectangular domains 14
    2.2.3 Stabilization of advection 15
2.3 Isogeometric discretization of the structure subproblem 16
2.4 Discretization of surface integrals 17
2.5 Discretization of fluid–structure coupling 18
    2.5.1 Separation of normal and tangential fluid–structure coupling 18
    2.5.2 Time integration algorithm 20
    2.5.3 Block iterative solution of the implicit problem 23
    2.5.4 Discussion 24

3 Convergence of the semi-implicit integration **27**
3.1 Scalar parabolic model problem 27
    3.1.1 Scalar parabolic problem statement 27
    3.1.2 Semi-implicit time integration 29
    3.1.3 Convergence of the regularized problem 30
    3.1.4 Uniform bound in $H^{3/2-\epsilon}(\Omega)$ 32
    3.1.5 Spatial discretization of the modified equation 34
    3.1.6 Semi-discrete convergence for $r = 0$ 36
    3.1.7 Discretization in time 40
    3.1.8 Numerical experiment: scalar parabolic problem 42
3.2 Extension to related linear problems 45
    3.2.1 Unsteady Stokes flow 45
    3.2.2 Numerical experiment: linearized Taylor–Green vortex 47
    3.2.3 Coupled second-order problems 47
3.3 Extrapolation to Navier–Stokes flow 49
    3.3.1 Taylor–Green vortex 49
    3.3.2 Translating Taylor–Green vortex 50
    3.3.3 Infinite Reynolds number 51

4 Block iterative convergence **52**
4.1 A generic model problem 53
4.2 Application to FSI 56
4.3 Relation to Newton iteration 58
4.4 Numerical test 59

5 An FSI benchmark problem **60**
5.1 Problem definition 61
5.2 Immersogeometric discretizations with div-conforming B-splines 61
5.3 Comparison of results 63
5.4 Block iterative convergence 64

6 Heart valve closing under physiological pressure **65**
6.1 Test problem definition 66
6.2 Discretization 66
6.3 Results 68

7 Simulating an *in vitro* experiment **69**
7.1 Description of the experiment 71
  7.1.1 The acrylic tube 72
  7.1.2 The valve 74
7.2 Mathematical model of the experiment 75
  7.2.1 Fluid subproblem 75
  7.2.2 Structure subproblem 75
7.3 Discretization of the mathematical model 78
7.4 Comparison of results 78

8 Conclusions and further work **81**

Appendix A Scaling stabilization parameters to improve mass conservation **82**

Appendix B Hessian of the discrete velocity **86**

1. Introduction

Analysis of thin structures immersed in incompressible fluid remains a prominent research topic in the computational mechanics community. Practical instances of this problem include parachute dynamics [1, 2], flying insects [3, 4], and the valves regulating blood flow through the heart [5–21]. The last topic mentioned, heart valve fluid–structure interaction (FSI), has received much attention in the past few years due to both the unique combination of challenges it poses to computational mechanicians and the practical benefits to be reaped from improved understanding of heart valve FSI dynamics. The need for and progress on FSI analysis of native and prosthetic heart valves was recently reviewed in [22].

In our earlier work on heart valve FSI, we developed a computational method for fluid–thin structure interaction that was initially described in [16] and refined in [17, 18, 23]. For reasons explained in the cited references, we developed an immersed method for FSI, in which the fluid and structure meshes are not required to match at the fluid–structure interface. In [16–18, 23], we discretized the thin structure isogeometrically, using non-uniform rational B-spline (NURBS) basis functions [24] to represent both the geometry and the displacement solution. Hughes et al. [25] introduced isogeometric analysis (IGA) as a paradigm for streamlining the process of generating analysis meshes from design geometries. Aside from its potential to eliminate unnecessary labor from the design-through-analysis pipeline [26–28], IGA has attracted attention due to the improvements in solution quality that follow from incorporation of exact design geometry and smooth solution spaces into engineering analysis [29–33]. These benefits are evident in the analysis of fluid mechanics [25, 34–36] and sliding contact problems [37–39], both of which are important to the dynamics of heart valves. Further, smooth, spline-based analysis spaces permit thin-shell formulations without rotational degrees of freedom, leading to simple, efficient, and robust methods for shell structure analysis [40–43].

Hughes et al. [25] initially presented IGA as a unification of isoparametric finite element analysis and spline-based geometry design, as reflected by its name. An alternate way of incorporating geometry into analysis is to capture it on an unfitted background mesh [26, 44–46]. We introduced the term *immersogeometric analysis* in [16] to identify this emerging trend, and applied it to our methods for coupling isogeometric structure discretizations to fluid solutions on unfitted meshes.

Our earlier work [16] on immersogeometric FSI analysis used a stabilized finite element discretization of the fluid subproblem. This formulation enforces incompressibility weakly: the discrete fluid velocity solution is not, in general, exactly solenoidal. Weak enforcement of mass conservation is sufficient for many problems and, following the pioneering work of Taylor and collaborators [47–49], stabilized finite elements form the backbone of several leading platforms for vascular computational fluid dynamics (CFD) in both academia (SimVascular [50, 51] and CRIMSON [52, 53]) and industry (HeartFlow, Inc. [54, 55]). Stabilized finite element formulations for incompressible flow have also underpinned countless studies on vascular FSI [56, 57], boundary conditions for vascular flows [58, 59], and optimization in cardiovascular modeling [60]. We found, however, that immersing thin structures in such fluid discretizations can lead to truly catastrophic violations of mass conservation. In [16, Section 4.4.1], we showed that mass loss in heart valve simulations could lead to larger aortic flows during diastole than systole.[1] The "solution" proposed in [16] was to apply an *ad hoc* scaling to the stabilization parameters of the formulation. We include, in Appendix A of the present paper, an explanation of why this scaling improves approximations of hydrostatic solutions with steep pressure gradients. However, we do not have a clear guide for how to select the scaling parameter and we have no guarantee that it avoids locking or other instabilities if the scaling carried to an extreme. Further, as pointed out in [16, Remark 13], scaling stabilization parameters to improve mass conservation makes the discrete problem more difficult to solve. Requiring analysts to tinker with the stabilization scaling for each new problem to figure out how much performance and stability should be sacrificed to obtain acceptable mass conservation is obviously not ideal.

The problem of poor mass conservation in immersed boundary discretizations was recognized early on by Peskin and Printz [61], who observed the same phenomenon of effective leakage through immersed surfaces and offered a solution in the context of a specific numerical framework. Galvin et al. [62] clarified that the underlying issue is, in fact, the combination of weak mass conservation and large irrotational source terms, of which thin immersed structures supporting pressure jumps are a prime example.[2] The solution offered by [62] was similar to our own, namely, to multiply a grad-div stabilization term by a large factor, with the caveat that scaling by too large a factor may degrade solution quality[3] and discrete problem conditioning. Galvin et al. point out, however, that divergence-conforming discretizations of incompressible flow can circumvent the issue entirely, citing the Scott–Vogelius element [64] as an example. Divergence-conforming discretizations deliver pointwise divergence-free velocity solutions by posing the weak problem over spaces forming a discrete de Rahm complex [65] in which the divergence operator maps velocities into the pressure space.

In this paper, we build upon a recently-developed divergence-conforming B-spline discretization for incompressible flow [36, 66, 67] to resolve the issue of mass loss in immersed FSI analysis. To fix ideas, we focus our discussion on the semi-implicit method for immersed fluid–structure coupling proposed in [16] and improved in [23]. Section 2 reviews the problem setting and describes our discretization. In the divergence-conforming setting, incompressible flow can be viewed at the discrete level as an unconstrained parabolic problem posed over a divergence-free velocity function space. Invoking the analogy to unconstrained parabolic problems, Sections 3 and 4

---

[1] For readers unfamiliar with cardiovascular physiology, this means that the computed flow field is totally unphysical; the aortic valve typically blocks flow through the aorta during diastole.

[2] This is a distinct problem from poor mass conservation in CFD/FSI discretizations that activate and deactivate fluid subproblem unknowns as a bulky immersed structure moves through the fluid mesh. In this paper, we focus on the thin structure case, in which the structure manifests as a concentrated force on the fluid subproblem.

[3] An interesting exception is discussed in [63]; for Taylor–Hood elements refined in a particular pattern, the solution resulting from extreme grad-div stabilization approaches that of a Scott–Vogelius discretization.

analyze the convergence of our numerical method when it is used to apply Dirichlet boundary conditions along immersed boundaries in linear parabolic model problems. Numerical experiments indicate that convergence is, in practice, better than predicted by the analysis, even for nonlinear problems. To demonstrate the practical robustness of divergence-conforming immersogeometric analysis, we apply it to FSI problems relevant to cardiovascular simulation. In Section 5, we compare its accuracy to a boundary-fitted reference solution of a benchmark problem consisting of a simplified, 2D, non-coapting heart valve. Then, in Section 6, we use the divergence-conforming immersogeometric approach to simulate a 3D valve opening and closing under physiological pressure levels. The results illustrate how strong enforcement of mass conservation ensures that the qualitative features of difficult incompressible flow and FSI solutions will be captured without problem-specific tuning or extreme mesh refinement. We also use this problem to demonstrate that these benefits remain largely intact through the algebraic approximations needed for practical 3D simulations, with loose algebraic tolerances resulting in only minor deviations from incompressibility. As a further example, Section 7 applies the technologies discussed in this paper to simulation of an *in vitro* experiment that pumped water through an artificial heart valve. Lastly, Section 8 summarizes the benefits and future challenges of using divergence-conforming B-splines for immersogeometric FSI analysis.

2. Mathematical model and immersogeometric discretization of FSI

This section introduces a mathematical description of the problem of fluid–thin structure interaction and describes our immersogeometric discretization of it, using divergence-conforming B-splines for the fluid subproblem. The discretization of fluid–structure coupling is essentially the same as that introduced in [23], but we present it here, in full, for completeness, using a notation that clearly relates it to the analogous linear model problems of Section 3.

2.1. A mathematical model of fluid–thin structure interaction

We consider a thin shell structure, modeled using Kirchhoff–Love theory, interacting with an incompressible Newtonian fluid. The subproblems are coupled through kinematic and traction compatibility conditions along the fluid–solid interface. Due to its thinness, the structure is modeled geometrically as a $(d-1)$-dimensional surface embedded in the d-dimensional fluid domain.

2.1.1. Augmented Lagrangian formulation of FSI

Our starting point is the augmented Lagrangian framework for FSI [68], which we specialize to the case of thin structures. Denote the region occupied by incompressible Newtonian fluid by $\Omega_1 \subset \mathbb{R}^d$, where d is the number of space dimensions. The structure geometry at time t is modeled by the surface $\Gamma_t \subset \Omega_1$, with dimension $d-1$. Let $\mathbf{u}_1$ and p denote the fluid's velocity and pressure.

Let $\mathbf{y}$ denote the structure's displacement from some reference configuration, Γ_0, and $\mathbf{u}_2 \equiv \dot{\mathbf{y}}$ denote the velocity of the structure. The fluid–structure kinematic constraint that $\mathbf{u}_1 = \mathbf{u}_2$ on Γ_t is enforced using the augmented Lagrangian

$$\int_{\Gamma_t} \boldsymbol{\lambda} \cdot (\mathbf{u}_1 - \mathbf{u}_2)\, d\Gamma + \frac{1}{2}\int_{\Gamma_t} \beta |\mathbf{u}_1 - \mathbf{u}_2|^2 \, d\Gamma \,, \tag{1}$$

where $\boldsymbol{\lambda}$ is a Lagrange multiplier and $\beta \geq 0$ is a penalty parameter. The resulting variational problem is: Find $\mathbf{u}_1 \in \mathcal{S}_u$, $p \in \mathcal{S}_p$, $\mathbf{y} \in \mathcal{S}_d$, and $\boldsymbol{\lambda} \in \mathcal{S}_\ell$ such that, for all test functions $\mathbf{w}_1 \in \mathcal{V}_u$, $q \in \mathcal{V}_p$, $\mathbf{w}_2 \in \mathcal{V}_d$, and $\delta\boldsymbol{\lambda} \in \mathcal{V}_\ell$

$$\begin{aligned}
B_1(\{\mathbf{u}_1, p\}, \{\mathbf{w}_1, q\}) - F_1(\{\mathbf{w}_1, q\}) + \int_{\Gamma_t} \mathbf{w}_1 \cdot \boldsymbol{\lambda}\, d\Gamma + \int_{\Gamma_t} \mathbf{w}_1 \cdot \beta(\mathbf{u}_1 - \mathbf{u}_2)\, d\Gamma &= 0 \,, &(2)\\
B_2(\mathbf{y}, \mathbf{w}_2) - F_2(\mathbf{w}_2) - \int_{\Gamma_t} \mathbf{w}_2 \cdot \boldsymbol{\lambda}\, d\Gamma - \int_{\Gamma_t} \mathbf{w}_2 \cdot \beta(\mathbf{u}_1 - \mathbf{u}_2)\, d\Gamma &= 0 \,, &(3)\\
\int_{\Gamma_t} \delta\boldsymbol{\lambda} \cdot (\mathbf{u}_1 - \mathbf{u}_2)\, d\Gamma &= 0 \,, &(4)
\end{aligned}$$

where $\mathcal{S}_u$, $\mathcal{S}_p$, $\mathcal{S}_d$, and $\mathcal{S}_\ell$ are trial solution spaces for the fluid velocity, fluid pressure, structural displacement, and Lagrange multiplier solutions, respectively. $\mathcal{V}_u$, $\mathcal{V}_p$, $\mathcal{V}_d$, and $\mathcal{V}_\ell$ are the corresponding test function spaces. B_1, B_2, F_1, and F_2 are the semi-linear forms and linear functionals corresponding to the (weak) fluid and structural dynamics problems.

2.1.2. *Fluid subproblem*

As mentioned above, the weak fluid subproblem is defined to be incompressible and Newtonian:

$$\begin{aligned}
B_1(\{\mathbf{u}, p\}, \{\mathbf{w}, q\}) &= \int_{\Omega_1} \mathbf{w} \cdot \rho_1 \left(\left.\frac{\partial \mathbf{u}}{\partial t}\right|_{\mathbf{x}} + \mathbf{u} \cdot \boldsymbol{\nabla}\mathbf{u} \right) d\Omega + \int_{\Omega_1} \boldsymbol{\varepsilon}(\mathbf{w}) : \boldsymbol{\sigma}_1 \, d\Omega \\
&\quad + \int_{\Omega_1} q \boldsymbol{\nabla} \cdot \mathbf{u}\, d\Omega - \gamma \int_{\Gamma_{1\mathbf{h}}} \mathbf{w} \cdot \rho_1 \{\mathbf{u} \cdot \mathbf{n}_1\}_- \mathbf{u}\, d\Gamma \,, &(5)\\
F_1(\{\mathbf{w}, q\}) &= \int_{\Omega_1} \mathbf{w} \cdot \rho_1 \mathbf{f}_1 \, d\Omega + \int_{\Gamma_{1\mathbf{h}}} \mathbf{w} \cdot \mathbf{h}_1 \, d\Gamma \,, &(6)
\end{aligned}$$

where ρ_1 is the fluid mass density, $\boldsymbol{\varepsilon}$ is the symmetric gradient operator, $\boldsymbol{\sigma}_1 = -p\mathbf{I} + 2\mu\boldsymbol{\varepsilon}(\mathbf{u})$, where μ is the dynamic viscosity, $\mathbf{f}_1$ is a prescribed body force, and $\mathbf{h}_1$ is a prescribed traction on $\Gamma_{1\mathbf{h}} \subset \partial\Omega_1$. $\partial(\cdot)/\partial t|_{\mathbf{x}}$ indicates time differentiation with respect to a fixed point $\mathbf{x}$ in Ω_1. The last term of (5) is not usually considered to be part of the weak Navier–Stokes problem, but it enhances the stability of the problem in cases where flow enters through the Neumann boundary $\Gamma_{1\mathbf{h}}$ [59], frequently encountered in cardiovascular simulations. The function $\{\cdot\}_-$ isolates the negative part of its argument, i.e.

$$\{x\}_- = \begin{cases} 0 & x > 0 \\ x & \text{otherwise} \end{cases} \; . \tag{7}$$

The coefficient γ controls the strength of this stabilizing term and $\mathbf{n}_1$ is the outward-facing normal to Ω_1. This term is often viewed as a detail of the discretization, but γ is typically $O(1)$, in which case the perturbation introduced by this stabilization is a modification of the mathematical model; it will not converge to zero with refinement of the discretization. The stabilizing effect of this term can be understood by observing that the choice of $\gamma \geq 1$ hides any non-coercive contributions from advection (after integration by parts). Smaller values may be desired, though, in situations where flow is supposed to enter through $\Gamma_{1\mathbf{h}}$, e.g. when modeling pressure-driven flow through an artery.

2.1.3. Thin structure subproblem

Following the Kirchhoff–Love thin shell kinematic hypotheses (see, e.g. [40, 42, 69]), we define B_2 and F_2 from the structure subproblem as

$$B_2(\mathbf{y}, \mathbf{w}) = \int_{\Gamma_t} \mathbf{w} \cdot \rho_2 h_{\text{th}} \left. \frac{\partial^2 \mathbf{y}}{\partial t} \right|_{\mathbf{X}} d\Gamma + \int_{\Gamma_0} \int_{-h_{\text{th}}/2}^{h_{\text{th}}/2} D_{\mathbf{w}} \mathbf{E} : \mathbf{S} \, d\xi^3 d\Gamma \tag{8}$$

and

$$F_2(\mathbf{w}) = \int_{\Gamma_t} \mathbf{w} \cdot \rho_2 h_{\text{th}} \mathbf{f}_2 \, d\Gamma + \int_{\Gamma_t} \mathbf{w} \cdot \mathbf{h}^{\text{net}} \, d\Gamma \; , \tag{9}$$

where ρ_2 is the structure mass density, $\mathbf{f}_2$ is a prescribed body force, h_{th} is the thickness of the shell, ξ^3 is a through-thickness coordinate, and we have referred the elasticity term to the reference configuration (cf. [70, (1.80)]). $\mathbf{E}$ is the Green–Lagrange strain tensor corresponding to the displacement $\mathbf{y}$, $D_{\mathbf{w}}\mathbf{E}$ is its functional derivative in the direction of $\mathbf{w}$, viz.

$$D_{\mathbf{w}} \mathbf{E}(\mathbf{y}) = \left. \frac{d}{d\epsilon} \mathbf{E}(\mathbf{y} + \epsilon \mathbf{w}) \right|_{\epsilon=0} \; , \tag{10}$$

and $\mathbf{S}$ is the second Piola–Kirchhoff stress tensor, depending on $\mathbf{E}$. The last term of F_2 sums the prescribed tractions on the two sides of Γ_t: $\mathbf{h}^{\text{net}} = \mathbf{h}(\xi^3 = -h_{\text{th}}/2) + \mathbf{h}(\xi^3 = +h_{\text{th}}/2)$. $\partial(\cdot)/\partial t|_{\mathbf{X}}$ indicates time differentiation with respect to a fixed material point, $\mathbf{X} \in \Gamma_0$.

The Green–Lagrange strain $\mathbf{E}$ is simplified to depend entirely on the shell structure's midsurface displacement, $\mathbf{y} : \Gamma_0 \to \mathbb{R}^d$, so as to reduce the dimension of the solid mechanics problem. Stating the precise dependence of $\mathbf{E}$ on $\mathbf{y}$ requires some notation. We assume, for now, that $d = 3$ (so that Γ_t is a 2D surface), as the specialization to $d = 2$ (i.e. a 2D beam theory in which Γ_t is a 1D curve) is straightforward. First, consider a coordinate chart on Γ_0, mapping points $\mathbf{X}$ of the midsurface to coordinate pairs (ξ^1, ξ^2) (in a sufficiently regular manner for the following discussion to make sense). Then allow a third coordinate ξ^3 to parameterize material points extruded in the normal direction to Γ_0. Letting Greek letter indices have the range $\{1,2\}$, define covariant basis vectors

$$\mathbf{A}_\alpha = \frac{\partial \mathbf{X}}{\partial \xi^\alpha}\ , \quad \mathbf{A}_3 = \frac{\mathbf{A}_1 \times \mathbf{A}_2}{|\mathbf{A}_1 \times \mathbf{A}_2|} \tag{11}$$

and

$$\mathbf{a}_\alpha = \frac{\partial \mathbf{x}}{\partial \xi^\alpha}\ , \quad \mathbf{a}_3 = \frac{\mathbf{a}_1 \times \mathbf{a}_2}{|\mathbf{a}_1 \times \mathbf{a}_2|} \tag{12}$$

on the reference and deformed configurations, where $\mathbf{x}(\mathbf{X}(\xi^1,\xi^2)) = \mathbf{y}(\mathbf{X}(\xi^1,\xi^2)) + \mathbf{X}(\xi^1,\xi^2)$ is the deformed position of the midsurface material point $\mathbf{X}$ that is mapped to coordinates (ξ^1,ξ^2). The corresponding contravariant basis vectors $\mathbf{A}^i$ and $\mathbf{a}^i$ are such that

$$\mathbf{A}^i \cdot \mathbf{A}_j = \mathbf{a}^i \cdot \mathbf{a}_j = \delta^i{}_j\ . \tag{13}$$

These basis vectors can be used to provide formulas for the midsurface metric tensor

$$g_{\alpha\beta} = \mathbf{a}_\alpha \cdot \mathbf{a}_\beta\ , \tag{14}$$

$$G_{\alpha\beta} = \mathbf{A}_\alpha \cdot \mathbf{A}_\beta \tag{15}$$

and curvature coefficients

$$b_{\alpha\beta} = -\mathbf{a}_\alpha \cdot \frac{\partial \mathbf{a}_3}{\partial \xi^\beta} = \frac{\partial \mathbf{a}_\alpha}{\partial \xi^\beta} \cdot \mathbf{a}_3\ , \tag{16}$$

$$B_{\alpha\beta} = -\mathbf{A}_\alpha \cdot \frac{\partial \mathbf{A}_3}{\partial \xi^\beta} = \frac{\partial \mathbf{A}_\alpha}{\partial \xi^\beta} \cdot \mathbf{A}_3\ . \tag{17}$$

$G_{\alpha\beta}$, $g_{\alpha\beta}$, $B_{\alpha\beta}$, and $b_{\alpha\beta}$ are then used to define the in-plane components of the simplified Green–Lagrange strain at a point $(\mathbf{X},\xi^3)$ in $\Gamma_0 \times (-h_{\text{th}}/2, h_{\text{th}}/2)$:

$$E_{\alpha\beta} = \varepsilon_{\alpha\beta} + \xi^3 \kappa_{\alpha\beta}\ , \tag{18}$$

where

$$\varepsilon_{\alpha\beta} = \frac{1}{2}(g_{\alpha\beta} - G_{\alpha\beta})\ , \quad \kappa_{\alpha\beta} = B_{\alpha\beta} - b_{\alpha\beta}\ , \tag{19}$$

with respect to the basis $\mathbf{A}^\alpha \otimes \mathbf{A}^\beta$. While not strictly necessary, we find it most convenient to transform these components into a local Cartesian coordinate system. This ensures compatibility with tensor component formulas found in references assuming Cartesian coordinate systems, thereby expediting the implementation of constitutive relations found in the engineering literature. The local Cartesian basis vectors $\{\hat{\mathbf{I}}_j\}_{j=1}^3$ and $\{\hat{\mathbf{i}}_j\}_{j=1}^3$ are obtained by performing Gram–Schmidt orthonormalization of the covariant basis vectors $\{\mathbf{A}_j\}_{j=1}^3$ and $\{\mathbf{a}_j\}_{j=1}^3$, as in [42, (2.43)–(2.45)]. This ensures that the third coordinate remains out-of-plane, i.e. $\hat{\mathbf{I}}_3 = \mathbf{A}_3$ and $\hat{\mathbf{i}}_3 = \mathbf{a}_3$. For the components of the Green–Lagrange strain, this transformation is computed by (cf. [42, (3.41)])

$$E_{\alpha\beta} \leftarrow E_{\gamma\delta}\left(\hat{\mathbf{I}}_\gamma \cdot \mathbf{A}^\alpha\right)\left(\hat{\mathbf{I}}_\delta \cdot \mathbf{A}^\beta\right) . \tag{20}$$

For the remainder of the discussion on the structure subproblem we assume, unless stated otherwise, that tensor components are given in such a local Cartesian basis, so that all indexes can be written as subscripts without ambiguity.

Remark 1. The formula (20) differs from [42, (3.41)]. The formula [42, (3.41)] is stated in terms of contravariant basis vectors that vary through the thickness of the structure. However, [42] tacitly assumes (20) in the analytical integration of bending moments through the thickness (see [42, (3.38) and (3.39)]). This can be construed as a thin-shell approximation of the “shifter tensor” defined by [71, (63)]. Alternatively, the thin shell formulations of [69] and [72] do not make this approximation. The FSI analysis techniques of this paper are independent of how exactly the shell subproblem is formulated.

Remark 2. The components $E_{\alpha 3}$ and $E_{3\alpha}$ are assumed to be zero as part of the Kirchhoff–Love model. The component E_{33} must remain nonzero to obtain reasonable agreement with 3D elasticity for plane stress problems. E_{33} is made unique by introducing the assumption that $S_{33} = 0$. Given $\mathbf{y}$ (and thus all components of $\mathbf{E}$ aside form E_{33}) the scalar equation $S_{33}(\mathbf{E}) = 0$ can be solved for the unknown E_{33}. The exact expression for E_{33} in terms of $\mathbf{y}$ will therefore depend on the constitutive model expressing $\mathbf{S}$ as a function of $\mathbf{E}$.

Remark 3. For problems in which $d = 2$, the relevant restriction of this shell theory can be obtained by simply extruding the curve Γ_0 out of the plane to form a 2D shell, but constraining all displacements in the out-of-plane direction. This (rather than Euler–Bernoulli theory) is the model that we use for 2D problems involving “beams” in this paper.

No special limitations on constitutive modeling are introduced by the use of Kirchhoff–Love shell theory. For simplicity, we model structures as hyperelastic, meaning that

$$\mathbf{S} = \frac{\partial \Psi}{\partial \mathbf{E}} , \tag{21}$$

where Ψ is some functional mapping strains to scalar energy densities [73, Chapter 6]. The simplest example of a strain energy functional is motivated by a formal extension of linearized elasticity:

$$\Psi = \frac{1}{2}\mathbf{E} : \boldsymbol{C} : \mathbf{E} \quad \Rightarrow \quad \mathbf{S} = \boldsymbol{C} : \mathbf{E}\,, \tag{22}$$

where $\boldsymbol{C}$ is a rank-four elasticity tensor. In the case where $\boldsymbol{C}$ corresponds to an isotropic material and can be derived from a Young's modulus E and Poisson ratio ν, this model is referred to as a St. Venant–Kirchhoff material. The St. Venant–Kirchhoff model is popular for its simplicity, but suffers from instabilities in compression [73, Section 6.5, Exercise 4]. A model that is more accurate for soft tissue and rubber is the incompressible neo-Hookean model:

$$\Psi = \frac{\mu_s}{2}(\mathrm{tr}\mathbf{C} - 3) + p\left((\det\mathbf{C})^{1/2} - 1\right)\,, \tag{23}$$

where $\mu_s > 0$ is the single material parameter, known as the shear modulus, $\mathbf{C} = 2\mathbf{E} + \mathbf{I}$ is the right Cauchy–Green deformation tensor and p is a Lagrange multiplier to enforce the constraint of incompressibility.

Remark 4. The incompressible neo-Hookean model is a special case of the structural constitutive model for soft tissues introduced by Fan and Sacks [74]. Fan and Sacks use an incompressible neo-Hookean term in their strain energy functional to model the effects of extra-cellular matrix, alongside other terms to model the effects of collagen fibers.

2.2. *Divergence-conforming B-spline discretization of the fluid subproblem*

The fluid subproblem may be isolated by setting $\mathbf{w}_2 = \delta\boldsymbol{\lambda} = \mathbf{0}$, which yields (2), in which the structure velocity $\mathbf{u}_2$ and the Lagrange multiplier $\boldsymbol{\lambda}$ should be viewed as prescribed data. As stated in Section 1, we aim to totally eliminate mass loss in the discrete fluid solution by using a so-called "structure-preserving", "divergence-conforming", or "div-conforming" discretization. In such discretizations, the divergence of every function in the discrete velocity space is a member of the discrete pressure space. If this property is satisfied, then a solution $\mathbf{u}_1^h$ of the Galerkin discrete problem will satisfy the weak continuity equation for the test function $q^h = \nabla\cdot\mathbf{u}_1^h$, which implies pointwise mass conservation:

$$\begin{aligned}
&\forall q^h \in \mathcal{V}_p^h\left((q^h, \nabla\cdot\mathbf{u}_1^h)_{L^2(\Omega_1)} = 0\right) \quad \text{and} \quad \nabla\cdot\mathbf{u}_1^h \in \mathcal{V}_p^h && (24)\\
&\Rightarrow (\nabla\cdot\mathbf{u}_1^h, \nabla\cdot\mathbf{u}_1^h)_{L^2(\Omega_1)} = 0 && (25)\\
&\Rightarrow \|\nabla\cdot\mathbf{u}_1^h\|^2_{L^2(\Omega_1)} = 0 && (26)\\
&\Rightarrow \nabla\cdot\mathbf{u}_1^h(\mathbf{x}) = 0 \qquad \text{for a.e. } \mathbf{x} \in \Omega_1\,. && (27)
\end{aligned}$$

A discretization of this type was developed for Stokes and Navier–Stokes flows by Evans and Hughes [36, 66, 67]. Evans and Hughes used B-splines to construct velocity and pressure spaces satisfying the necessary properties, then directly posed the weak problem $B_1(\{\mathbf{u}_1^h, p^h\}, \{\mathbf{w}_1^h, q^h\}) = F_1(\{\mathbf{w}_1^h, q^h\})$ over these discrete spaces (augmenting it with Nitsche's method to enforce no-slip boundary conditions). A caveat to the above reasoning is that, to truly obtain velocities that conform to the incompressibility constraint, one would need to solve the discrete algebraic problem *exactly*, which is almost always impractical for real problems. We demonstrate in the 3D numerical examples of Sections 6 and 7, however, that the benefits of divergence-conforming discretizations are robust enough to persist through commonly-used approximations in the assembly and solution of the discrete problem.

As mentioned above, Evans and Hughes used Nitsche's method to enforce no-slip boundary conditions in a strongly consistent manner that allows for optimal convergence to sufficiently-regular solutions. For the immersogeometric computations of this paper, the regularity of the fluid velocity solution is always low (at most $H^{3/2-\epsilon}(\Omega_1)$) and we use, for simplicity,[4] a "naive" velocity penalization, i.e. we alter the problem to be

$$B_1(\{\mathbf{u}_1, p\}, \{\mathbf{w}_1, q\}) + C_{\text{pen}} \int_{\Gamma_{\text{pen}}} (\mathbf{u}_1 - \mathbf{g}) \cdot \mathbf{w}_1 \, d\Gamma = F_1(\{\mathbf{w}_1, q\}) \ , \tag{28}$$

where $C_{\text{pen}} > 0$ is a penalty parameter and $\mathbf{g}$ is the desired velocity on $\Gamma_{\text{pen}} \subset \partial\Omega_1$. If the normal component of the Dirichlet boundary condition is strongly enforced (i.e. built directly into the spaces in which $\mathbf{u}_1$ and $\mathbf{w}_1$ live), the formulation (28) can be used unaltered to penalize just the tangential portion of the boundary condition. If the penalty constant C_{pen} scales like μ/h, then this remains weakly consistent with the Navier–Stokes problem.

Div-conforming B-splines for incompressible flow are a specific application of a narrow subset of discrete de Rahm complexes. This is an important topic not only for approximation of incompressible flows but for computational electromagnetics and magnetohydrodynamics as well. In this paper, we focus exclusively on the application to incompressible flow, with an eye toward implementation. Readers interested in generalizations and theoretical aspects should refer to [65] for a discussion of discrete exterior calculus and [75, 76] for its development within IGA.

2.2.1. *Construction for rectangular domains*

Suppose, for now, that Ω_1 is an axis-aligned d-dimensional rectangle. Then physical space can serve directly as a d-variate B-spline parameter space. Define a d-variate scalar B-spline space for the pressure on Ω_1. Then, for $1 \leq i \leq d$, we can k-refine the pressure space once in the i^{th} parametric direction to obtain a scalar space for the i^{th} Cartesian velocity component. Due to well-known properties of B-splines under differentiation [24], the i^{th} partial derivative of the i^{th}

---

[4] Actually, the consistency of Nitsche's method relies on having an exact velocity solution in $H^{3/2+\epsilon}(\Omega_1)$ (cf. [66, Section 7.2]), which is marginally more regular than we would expect from an immersed boundary approach.

velocity component will then be in the pressure space. The scalar basis functions of the d velocity component spaces can be multiplied by their respective unit vectors to obtain a vector-valued basis for the discrete velocity space. The divergence of a vector-valued velocity function will therefore be a sum of d scalar functions in the pressure space.

A statement of all possible structure-preserving B-spline spaces can (after defining the appropriate notation) be written in a compact formula, as in [66, Section 5.2]. In the notation of the cited reference, the velocity space is $\widehat{\mathcal{RT}}_h$ and the pressure space is $\widehat{\mathcal{W}}_h$. Following the terminology of [66], if the pressure space has polynomial degree k' in all directions, we say that the entire pressure and velocity discretization is of degree k', despite the presence of $(k' + 1)$-degree splines in the velocity component spaces.

To clarify the construction, we spell out an example of degree $k' = 1$. Suppose $d = 2$ and the pressure space has degree one $(= k')$ in both the x_1 and x_2 directions. Its (open) knot vectors in the x_1 and x_2 directions are both

$$(1, 1, 2, 3, 4, 5, 6, 7, 7)\ . \tag{29}$$

Then the scalar B-spline space $\mathcal{S}_{u_1}$ for the x_1 component of $\mathbf{u}_1$ would have knot vector

$$(1, 1, 1, 2, 3, 4, 5, 6, 7, 7, 7) \tag{30}$$

and degree two $(= k' + 1)$ in the x_1 direction and knot vector

$$(1, 1, 2, 3, 4, 5, 6, 7, 7) \tag{31}$$

and degree one $(= k')$ in the x_2 direction. The partial derivative $\frac{\partial}{\partial x_1}$ maps functions from this space to the pressure space. Vector-valued basis functions for the velocity are obtained by multiplying the scalar basis functions of $\mathcal{S}_{u_1}$ by the unit vector $\mathbf{e}_1$. Similarly, the space $\mathcal{S}_{u_2}$ for the x_2 component of $\mathbf{u}_1$ would have knot vector

$$(1, 1, 2, 3, 4, 5, 6, 7, 7) \tag{32}$$

and degree one in the x_1 direction and knot vector

$$(1, 1, 1, 2, 3, 4, 5, 6, 7, 7, 7) \tag{33}$$

and degree two in the x_2 direction. The corresponding vector-valued velocity basis functions are obtained by multiplying scalar basis functions of S_{u_2} by $\mathbf{e}_2$. The extensions to higher polynomial orders, more space dimensions, different knot multiplicities, periodic domains, and so on should be straightforward.

2.2.2. *Generalization to non-rectangular domains*

Div-conforming B-splines are not limited to rectangular domains. A point $\mathbf{X}$ in a rectangular parametric domain $\widehat{\Omega}$ may be mapped to a point $\mathbf{x}$ in a non-rectangular physical domain Ω, using a motion $\mathbf{x} = \boldsymbol{\phi}(\mathbf{X})$. (The regularity requirements of this mapping are given in [66, Section 4.3], with some differences in notation.) To obtain divergence-conforming velocity and pressure spaces on the physical domain Ω, vector-valued velocity basis functions defined on $\widehat{\Omega}$ can be pushed forward using the Piola transform [77]. For an arbitrary parametric-space velocity function $\widehat{\mathbf{u}}$, its physical-space counterpart $\mathbf{u}$ is

$$\mathbf{u}(\mathbf{x}) = \frac{1}{J(\mathbf{X})}\mathbf{F}(\mathbf{X})\widehat{\mathbf{u}}(\mathbf{X}) \,, \tag{34}$$

where, using Cartesian index notation [73, Section 1.1] and symbols analogous to those frequently seen in nonlinear elasticity, $\mathbf{F}$ is the deformation gradient of $\boldsymbol{\phi}$, viz.

$$\mathbf{F} = \frac{\partial \boldsymbol{\phi}}{\partial \mathbf{X}} \quad \Longleftrightarrow \quad F_{iJ} = \frac{\partial \phi_i}{\partial X_J} = \phi_{i,J} \,, \tag{35}$$

and J is the determinant of $\mathbf{F}$. Using Nanson's formula and integration by parts, this implies the well-known Piola identity

$$\operatorname{div} \mathbf{u} = \frac{1}{J}\mathrm{DIV}\,\widehat{\mathbf{u}} \,, \tag{36}$$

where

$$\operatorname{div} \mathbf{u} = \frac{\partial u_j}{\partial x_j} = u_{j,j} \quad \text{and} \quad \mathrm{DIV}\,\widehat{\mathbf{u}} = \frac{\partial \widehat{u}_B}{\partial X_B} = \widehat{u}_{B,B} \,. \tag{37}$$

(For readers unfamiliar with this identity, it also follows easily from (40), derived below.) To ensure pointwise divergence-free velocity solutions, we would like the divergence of every pushed-forward velocity function to exist in the pushed-forward pressure space. Recall that, for every $\widehat{\mathbf{u}}$ in the parametric velocity space, there exists $\widehat{q}$ in the parametric pressure space such that $\widehat{q} = \mathrm{DIV}\,\widehat{\mathbf{u}}$. Then, in view of (36), the parametric pressure space function should be pushed forward by

$$q(\mathbf{x}) = \frac{1}{J(\mathbf{X})}\widehat{q}(\mathbf{X}) \,, \tag{38}$$

so that $q = \operatorname{div} \mathbf{u}$ and the argument (24)–(27) remains valid.

The weak Navier–Stokes equations involve the spatial gradient of the pushed-forward velocity $\mathbf{u}$, viz. $u_{i,j}$. Given the B-spline control point values for components of $\widehat{\mathbf{u}}$, it is only immediately straightforward to evaluate $\widehat{u}_{A,B}$. We derive here a formula for the physical velocity gradient in terms of the $\mathbf{X}$-derivatives of $\widehat{\mathbf{u}}(\mathbf{X})$ and $\boldsymbol{\phi}(\mathbf{X})$. We use the identity

$$\frac{\partial J}{\partial F_{iA}} = J F^{-1}_{Ai} \,, \tag{39}$$

which is equivalent to [73, (1.241)]. Underlines and colors are purely for visual clarity.

$$
\begin{aligned}
u_{i,j} &= \left(\frac{1}{J} F_{iA} \hat{u}_A\right)_{,j} \\
&= \left\{ \left(\frac{1}{J}\right)_{,j} F_{iA} + \frac{1}{J} F_{iA,j} \right\} \hat{u}_A + \frac{1}{J} F_{iA} \hat{u}_{A,j} \\
&= \left\{ \left(\frac{-1}{J^2} \frac{\partial J}{\partial F_{\ell B}} \frac{\partial F_{\ell B}}{\partial X_C} \frac{\partial X_C}{\partial x_j} \right) F_{iA} + \frac{1}{J} \frac{\partial F_{iA}}{\partial X_C} \frac{\partial X_C}{x_j} \right\} \hat{u}_A + \frac{1}{J} F_{iA} \frac{\partial \hat{u}_A}{\partial X_C} \frac{\partial X_C}{\partial x_j} \\
&= \left\{ \frac{-1}{J^2} \frac{\partial J}{\partial F_{\ell B}} F_{\ell B,C} F^{-1}_{Cj} F_{iA} + \frac{1}{J} F_{iA,C} F^{-1}_{Cj} \right\} \hat{u}_A + \frac{1}{J} F_{iA} \hat{u}_{A,C} F^{-1}_{Cj} \\
&= \left\{ \frac{-1}{\underline{\underline{J}}} F^{-1}_{B\ell} F_{\ell B,C} \underline{F^{-1}_{Cj}} F_{iA} + \frac{1}{\underline{\underline{J}}} F_{iA,C} \underline{F^{-1}_{Cj}} \right\} \hat{u}_A + \frac{1}{\underline{\underline{J}}} F_{iA} \hat{u}_{A,C} \underline{F^{-1}_{Cj}} \\
&= \frac{1}{\underline{\underline{J}}} \left(\left\{ -F^{-1}_{B\ell} F_{\ell B,C} F_{iA} + F_{iA,C} \right\} \hat{u}_A + F_{iA} \hat{u}_{A,C} \right) \underline{F^{-1}_{Cj}} \,.
\end{aligned}
\tag{40}
$$

By substituting j for i and invoking the symmetry of $\boldsymbol{\phi}$'s Hessian, one may easily derive (36) from the last line of (40). The Laplacian of the pushed-forward velocity, $\Delta \mathbf{u} = u_{i,jj} \mathbf{e}_i$, is required for some numerical schemes, such as the streamline upwind Petrov–Galerkin (SUPG) method [78]. Although we do not require the Laplacian for the methods used in this paper, we direct the reader to Appendix B for a derivation of a formula for the second derivatives of velocity components, $u_{i,jk}$.

Remark 5. Div-confomring B-splines may be used on wider classes of geometries by joining deformed rectangular meshes together with a discontinuous Galerkin approach, as described in [66, Section 6.5], but this possibility is not exploited in the present work.

2.2.3. *Stabilization of advection*

Galerkin's method is not necessarily stable for practically-coarse discretizations of high-Reynolds-number flows. The Galerkin discretization used by Evans and Hughes can be straightforwardly augmented to include SUPG stabilization [78] (but *without* its frequent accomplice pressure stabilizing Petrov–Galerkin (PSPG) [79], which would clearly disrupt the pointwise mass conservation). However, the appearance of the pressure gradient in the momentum equation residual removes the property of the Galerkin approximation that the error in the velocity solution is independent of pressure interpolation error [67, (6.32)]. This property is valuable in the presence of immersed boundaries that induce large discontinuities in the exact pressure solution. In this paper, we stabilize div-conforming discretizations in a weakly-consistent manner, by introducing an $O(h)$

streamline diffusion. Specifically, we add

$$+\sum_e(\tau\rho_1\mathbf{u}_1^h\cdot\nabla\mathbf{u}_1^h,\mathbf{u}_1^h\cdot\nabla\mathbf{w}_1^h)_{L^2(\Omega^e)} \tag{41}$$

to $B_1(\{\mathbf{w}_1^h,q^h\},\{\mathbf{u}_1^h,p^h\})$, where $\{\Omega^e\}_{e=1}^{N_{\mathrm{el}}}$ are the N_{el} Bézier elements of the B-spline mesh and

$$\tau=\begin{cases}\left(\mathbf{u}_1^h\cdot\mathbf{G}\mathbf{u}_1^h\right)^{-1/2} & \mathbf{u}_1^h\cdot\mathbf{G}\mathbf{u}_1^h>0\\ 0 & \text{otherwise}\end{cases}\ . \tag{42}$$

The components of $\mathbf{G}$ are defined in an element Ω^e by

$$G_{ij}=\frac{\partial\xi_i}{\partial x_k}\frac{\partial\xi_j}{\partial x_k}\ , \tag{43}$$

where $\boldsymbol{\xi}\in(-1,1)^d$ is a normalized parametric coordinate in Ω^e that is mapped to a physical point $\mathbf{x}\in\Omega_1$. While this form of stabilization is only weakly consistent, we do not expect high order convergence rates from immersed boundary discretizations (of the type used in this paper), due to low-order interpolation errors. The stabilization term (41) should therefore not harm asymptotic convergence rates. Further, the artificial diffusion acts only in the flow direction, and is minimally disruptive to laminar solutions.

2.3. Isogeometric discretization of the structure subproblem

Setting $\mathbf{w}_1=\delta\boldsymbol{\lambda}=\mathbf{0}$ isolates the structure subproblem (3), in which $\mathbf{u}_2$ and $\boldsymbol{\lambda}$ are considered prescribed data. The resulting thin shell subproblem can be stably discretized using Galerkin's method. However, this has rarely been done prior to the introduction of IGA, because, for $B_2(\mathbf{w},\mathbf{y})$ to remain bounded, $\mathbf{w}$ and $\mathbf{y}$ need to be in $H^2(\Gamma)$; the formulation involves $L^2(\Gamma)$ inner products of second derivatives of test and trial functions. This essentially corresponds to the constraint that discrete spaces be subsets of $C^1(\Gamma)$.[5] Traditional finite element spaces do not satisfy this constraint. However, IGA spline spaces can be as smooth as the geometry allows.

Approximate enforcement of FSI kinematics can permit structural self-intersection in discrete solutions. To prevent this, we augment the structure subproblem with a penalty contact method described in [16, Section 5.2]. In summary (and with minor changes in notation), we collocate sliding contact constraints at quadrature points of the structure mid-surface and enforce them with opposing pairs of penalty forces. The magnitudes of these quadrature point forces are given by the

---

[5] This is not strictly mandated by the Sobolev embedding theorem unless the dimension of Γ is one (cf. [80, Theorem 5.4, Case C], with $j=1$, $p=2$, and $m=1$), but any practical discrete subspace of $H^2(\Gamma)$ composed of piecewise polynomial functions will be smooth.

formula

$$w\begin{cases} \dfrac{k_\mathrm{c}}{2h_\mathrm{c}}(d+h_\mathrm{c})^2 & , \quad d\in(-h,0) \\[2ex] \dfrac{k_\mathrm{c}h_\mathrm{c}}{2}+k_\mathrm{c}d & , \quad d\geq 0 \\[2ex] 0 & , \quad \text{otherwise} \end{cases} , \tag{44}$$

where w is the weight of the quadrature point, d is the (signed) penetration depth, k_c is the contact penalty stiffness, and h_c is a length scale over which penalty forces are smoothed to improve convergence. Penetrations of $|d| > c_\mathrm{c}$ are ignored. The parameter $c_\mathrm{c} \geq h_\mathrm{c}$ is a cutoff to avoid spurious non-local interactions. Using a quadrature rule to choose locations and weights of the contact elements ensures that parallel surfaces experience uniform pressure.

2.4. Discretization of surface integrals

Evaluation of integrals over Γ_t deserves some remark, since Γ_t does not conform to boundaries of the fluid elements $\{\Omega^e\}$. We employ a variant of the approach used by Düster et al. [81] to integrate immersed boundary traction in finite cell solutions of solid mechanics problems. Specifically, we define Gaussian quadrature rules on elements of the reference configuration Γ_0 of the immersed boundary. These rules are then weighted by the Jacobian determinant of the mapping from Γ_0 to Γ_t. For a quasi-uniform fluid mesh with element diameters bounded above and below by h, this practice suggests that surface quadrature elements should be of diameter $O(h)$, but we do not enforce this condition strictly in computations. The fact that the surface quadrature elements are not aligned with the mesh cells is certainly a "variational crime" [82, Sections 4.3, 4.4], although studies from the literature on finite cell methods [83–85] suggest that it is only a misdemeanor, as the influence of quadrature errors on co-dimension-one boundaries is small relative to the effects of errors in volume quadrature.

The integrals evaluated with this approximate quadrature rule involve traces of functions defined on the fluid domain. To evaluate these traces, we must locate the quadrature points of the surface in the parameter space of the background mesh. The physical location, $\mathbf{x}_g \in \mathbb{R}^d$, of an integration point can be obtained straightforwardly by evaluating the surface parameterization. Finding the point $\mathbf{X}_g \in \mathbb{R}^d$ that the fluid mesh parameterization maps to $\mathbf{x}_g$ requires solving a system of d equations to invert the mapping from the fluid mesh parameter space to physical space.

If the fluid is represented on a rectangular grid, this inversion is trivial. If the B-spline parametric space is mapped to the physical domain using some function $\boldsymbol{\phi}$ (in the notation of Section 2.2.2), we need to implement $\boldsymbol{\phi}^{-1}$. For some mappings, an analytical form of $\boldsymbol{\phi}^{-1}$ is available, but, more typically, we implement a Newton iteration on the parameter space. Given an implementation of $\boldsymbol{\phi}^{-1}$, however, one still cannot (efficiently) evaluate the fluid solution fields at $\mathbf{X}_g = \boldsymbol{\phi}^{-1}(\mathbf{x}_g)$. Efficient evaluation of spline functions requires knowledge of which basis functions have the parametric point $\mathbf{X}_g$ in their supports. This reduces to the problem of determining which Bézier element the parametric point $\mathbf{X}_g$ lies in. The tensor product structure of the B-spline space allows for an efficient solution of this problem by performing a binary search along each parametric direction.

2.5. Discretization of fluid–structure coupling

The augmented Lagrangian coupling the fluid and structure subproblems is discretized using a semi-implicit time integration scheme. The penalty term is treated implicitly and the Lagrange multiplier is updated explicitly. This method circumvents difficulties of fully-implicit coupling, while forbidding leakage through the structure in steady-state solutions and retaining the stability that eludes fully-explicit approaches. This section describes the spatial discretization of the fluid–structure kinematic constraint and the solution algorithm used to advance the coupled FSI system through time. Section 2.5.4 provides some interpretation of the discretization and its relation to other methods of enforcing fluid–structure boundary conditions. A precise analysis of the semi-implicit time integration algorithm is carried out in the context of linearized model problems in Section 3.

2.5.1. Separation of normal and tangential fluid–structure coupling

The constraint that $\mathbf{u}_1 = \mathbf{u}_2$ on Γ can be formally separated into two constraints: the no-penetration constraint on the normal velocities

$$\mathbf{u}_1 \cdot \mathbf{n}_2 = \mathbf{u}_2 \cdot \mathbf{n}_2 \tag{45}$$

and the no-slip constraint on the tangential velocities

$$\mathbf{u}_1 - (\mathbf{u}_1 \cdot \mathbf{n}_2)\,\mathbf{n}_2 = \mathbf{u}_2 - (\mathbf{u}_2 \cdot \mathbf{n}_2)\,\mathbf{n}_2\ , \tag{46}$$

where $\mathbf{n}_2$ is the normal vector to Γ_t (i.e. $\mathbf{a}_3$ defined in (12)). These constraints are enforced by the normal and tangential components of the multiplier field $\boldsymbol{\lambda}$ and the penalty force $\beta\,(\mathbf{u}_1 - \mathbf{u}_2)$.

The no-penetration constraint is critical to the qualitative structure of solutions. In the application to heart valve analysis, for instance, the valve leaflets must be able to stop flow when the valve is closed. The no-slip constraint is less essential and its strong enforcement may even be detrimental to the qualitative character of discrete solutions on coarse meshes [86–89].[6] We therefore

---

[6] The cited works attribute improved solution quality to the tangential slippage allowed by weak boundary condi-

discretize these two constraints differently. For the no-penetration constraint, we discretize a scalar Lagrange multiplier field on Γ, which we denote $\lambda = \boldsymbol{\lambda} \cdot \mathbf{n}_2$. For the no-slip constraint, we approximate the tangential component of $\boldsymbol{\lambda}$ by a weakly-consistent penalty force. The weakly-consistent penalty approximation of the tangential constraint may be seen as a degenerate case of Nitsche's famous strongly-consistent penalty method [90], as we explained in [16, Section 4.1]. Because the structure midsurface Γ_t can cut through the fluid domain in arbitrary ways, we do not attempt to construct inf-sup stable combinations of velocity and multiplier spaces. Instead, we circumvent the inf-sup condition by regularizing the no-penetration constraint residual:

$$(\mathbf{u}_1 - \mathbf{u}_2) \cdot \mathbf{n}_2 \quad \rightarrow \quad (\mathbf{u}_1 - \mathbf{u}_2) \cdot \mathbf{n}_2 - \frac{r}{\beta}\lambda \,, \tag{47}$$

where $r \geq 0$ is a dimensionless constant. This is essentially the perturbed Lagrangian approach that has previously been used to stabilize contact problems [91]. Much as the slip penalization can be derived as a degenerate case of Nitsche's method [16, Section 4.1], the regularization of the no-penetration constraint can be viewed as a degenerate case of strongly-consistent Barbosa–Hughes stabilization [92].

The problem that we proceed to discretize in time is then: Find $\mathbf{u}_1 \in \mathcal{S}_u$, $p \in \mathcal{S}_p$, $\mathbf{y} \in \mathcal{S}_d$, and $\lambda \in \mathcal{S}_\ell$ such that, for all test functions $\mathbf{w}_1 \in \mathcal{V}_u$, $q \in \mathcal{V}_p$, $\mathbf{w}_2 \in \mathcal{V}_d$, and $\delta\lambda \in \mathcal{V}_\ell$

$$\begin{aligned}
& B_1(\{\mathbf{w}_1, q\}, \{\mathbf{u}_1, p\}; \hat{\mathbf{u}}) - F_1(\{\mathbf{w}_1, q\}) + B_2(\mathbf{w}_2, \mathbf{y}) - F_2(\mathbf{w}_2) \\
& \quad + \int_{\Gamma_t} (\mathbf{w}_1 - \mathbf{w}_2) \cdot \lambda \mathbf{n}_2 \, d\Gamma && (48) \\
& \quad + \int_{\Gamma_t} (\mathbf{w}_1 - \mathbf{w}_2) \cdot \tau^B_{\text{NOR}} \left((\mathbf{u}_1 - \mathbf{u}_2) \cdot \mathbf{n}_2 \right) \mathbf{n}_2 \, d\Gamma && (49) \\
& \quad + \int_{\Gamma_t} (\mathbf{w}_1 - \mathbf{w}_2) \cdot \tau^B_{\text{TAN}} \left((\mathbf{u}_1 - \mathbf{u}_2) - \left((\mathbf{u}_1 - \mathbf{u}_2) \cdot \mathbf{n}_2 \right) \mathbf{n}_2 \right) \, d\Gamma && (50) \\
& \quad + \int_{\Gamma_t} \delta\lambda \cdot \left((\mathbf{u}_1 - \mathbf{u}_2) \cdot \mathbf{n}_2 - \frac{r\lambda}{\tau^B_{\text{NOR}}} \right) d\Gamma \;=\; 0 \,, && (51)
\end{aligned}$$

where we split the penalty term from the original variational problem into normal and tangential components. Based on dimensional analysis and the expectation that no-slip conditions vanish in the inviscid limit, we propose to scale the tangential penalty like

$$\tau^B_{\text{TAN}} = C_{\text{TAN}} \frac{\mu}{h} \,, \tag{52}$$

---

tions on coarse meshes. Obviously it is impossible for flow fields on either side of an immersed boundary to both slip in independent directions if they are represented on a single mesh, but we observe that excessive enforcement of tangential boundary conditions leads to Gibbs-like phenomena in the tangential velocity profile, which can generate spurious eddies.

where C_{TAN} is a dimensionless $O(1)$ constant and h is a measure of the fluid element diameter, with units of length. To ensure that the normal penalty does not disappear in the inviscid limit, we propose that it scale like

$$\tau^B_{\text{NOR}} = \max\left\{C^{\text{inert}}_{\text{NOR}}\frac{\rho_1 h}{\Delta t}, C^{\text{visc}}_{\text{NOR}}\frac{\mu}{h}\right\}\ , \tag{53}$$

where $C^{\text{inert}}_{\text{NOR}}$ and $C^{\text{visc}}_{\text{NOR}}$ are dimensionless constants and Δt is a time scale associated with the temporal discretization. The formulas (52) and (53) are guidelines for estimating the appropriate orders of magnitude for penalty values rather than strict rules. General purpose formulas for computing penalty parameters on nonuniform and/or anisotropic meshes might substitute the length scale h with $1/\sqrt{\mathbf{n}_2 \cdot \mathbf{G}\mathbf{n}_2}$ (with $\mathbf{G}$ defined by (43)), to incorporate local and directional information about the fluid mesh. However, the development and testing of such formulas is beyond the scope of this paper.

2.5.2. *Time integration algorithm*

This section states the semi-implicit time stepping procedure for the fully-discrete fluid–structure system. We compute approximate fluid structure and interface multiplier solutions at discrete time levels, indexed by n and separated by steps of size Δt. Suppose that, at step n, the discrete fluid velocity is defined by a vector of coefficients $\mathbf{U}^n$, the fluid acceleration by $\dot{\mathbf{U}}^n$, the fluid pressure by $\mathbf{P}^n$, and the structure displacement, velocity, and acceleration by $\mathbf{Y}^n$, $\dot{\mathbf{Y}}^n$, and $\ddot{\mathbf{Y}}^n$, respectively. We refer to the multiplier at time level n as λ^n, considering it a function defined over Γ_t, with the understanding that it is represented discretely as a set of samples at quadrature points of the (Lagrangian) integration rule on Γ_t. (Recall Section 2.4.) Considering the solution variables at time level n known, the first step of the algorithm is to construct a system of equations for all $(n+1)$-level unknowns, excluding λ^{n+1}, which is initially set equal to λ^n:

$$\text{Res}\left(\mathbf{U}^{n+\alpha_f}, \dot{\mathbf{U}}^{n+\alpha_m}, \mathbf{Y}^{n+\alpha_f}, \dot{\mathbf{Y}}^{n+\alpha_f}, \ddot{\mathbf{Y}}^{n+\alpha_m}, \mathbf{P}^{n+1}, \lambda^{n+1}(=\lambda^n)\right) = \mathbf{0}\ , \tag{54}$$

$$\mathbf{U}^{n+1} = \mathbf{U}^n + \Delta t\left((1-\gamma)\dot{\mathbf{U}}^n + \gamma\dot{\mathbf{U}}^{n+1}\right)\ , \tag{55}$$

$$\dot{\mathbf{U}}^{n+\alpha_m} = \dot{\mathbf{U}}^n + \alpha_m\left(\dot{\mathbf{U}}^{n+1} - \dot{\mathbf{U}}^n\right)\ , \tag{56}$$

$$\mathbf{U}^{n+\alpha_f} = \mathbf{U}^n + \alpha_f\left(\mathbf{U}^{n+1} - \mathbf{U}^n\right)\ , \tag{57}$$

$$\mathbf{Y}^{n+1} = \mathbf{Y}^n + \Delta t\dot{\mathbf{Y}}^n + \frac{\Delta t^2}{2}\left((1-2\beta)\ddot{\mathbf{Y}}^n + 2\beta\ddot{\mathbf{Y}}^{n+1}\right)\ , \tag{58}$$

$$\dot{\mathbf{Y}}^{n+1} = \dot{\mathbf{Y}}^n + \Delta t\left((1-\gamma)\ddot{\mathbf{Y}}^n + \gamma\ddot{\mathbf{Y}}^{n+1}\right)\ , \tag{59}$$

$$\ddot{\mathbf{Y}}^{n+\alpha_m} = \ddot{\mathbf{Y}}^n + \alpha_m\left(\ddot{\mathbf{Y}}^{n+1} - \ddot{\mathbf{Y}}^n\right)\ , \tag{60}$$

$$\dot{\mathbf{Y}}^{n+\alpha_f} = \dot{\mathbf{Y}}^n + \alpha_f\left(\dot{\mathbf{Y}}^{n+1} - \dot{\mathbf{Y}}^n\right)\ , \tag{61}$$

$$\mathbf{Y}^{n+\alpha_f} = \mathbf{Y}^n + \alpha_f\left(\mathbf{Y}^{n+1} - \mathbf{Y}^n\right)\ , \tag{62}$$

where α_m, α_f, β, and γ are parameters of the time integration scheme. The function Res(...) is the nonlinear residual corresponding to the discretization of (51) with $\delta\lambda = 0$. The multiplier test function is set to zero to exclude the FSI kinematic constraint equation. Because λ^{n+1} is held fixed, including this constraint would lead to an ill-posed system with more equations than unknowns. While the multiplier is considered fixed in this problem, the penalty terms are still treated implicitly. This penalty-coupled problem is resolved by a block iterative procedure, which alternates between solving for fluid and structure increments. This algorithm is described further in Section 2.5.3. The formulas (54)–(62) are based on the generalized-α method of time integration [93]. In past work using this method [16–18, 23], we followed Bazilevs et al. [94, Section 4.4], by working within a subset of second-order generalized-α methods parameterized by as single scalar, $\rho_\infty \in [0, 1]$, which controls numerical damping and defines the four free parameters as

$$\alpha_m = \frac{1}{2}\left(\frac{3-\rho_\infty}{1+\rho_\infty}\right) , \tag{63}$$

$$\alpha_f = \frac{1}{1+\rho_\infty} , \tag{64}$$

$$\gamma = \frac{1}{2} + \alpha_m - \alpha_f , \tag{65}$$

$$\beta = \frac{1}{4}\left(1 + \alpha_m + \alpha_f\right)^2 . \tag{66}$$

For a discussion of the effects of this parameter on stabilized finite element computations of unsteady Navier–Stokes, see the work of Jansen et al. [95]. In this work, for simplicity, and for direct analogy to the linear model problems analyzed in Section 3, we select the generalized-α parameters as

$$\alpha_m = \alpha_f = \gamma = \beta = 1 , \tag{67}$$

which leads to the first-order backward Euler method. (The overall accuracy of the semi-implicit algorithm is first-order, but integrating the fluid subproblem with a second-order method may improve the representation of unsteady turbulent flow features.) Because the system (54)–(62) does not include the fluid–structure kinematic constraint, the (regularized) α-level constraint residual

$$R^{n+\alpha} = \left(\left(\mathbf{u}_1^h\right)^{n+\alpha_f} - \left(\mathbf{u}_2^h\right)^{n+\alpha_f}\right) \cdot \mathbf{n}_2^{n+\alpha_f} - \frac{r\lambda^{n+1}}{\tau^B_{\text{NOR}}} \tag{68}$$

is not necessarily zero on $\Gamma_{t+\alpha_f}$. In (68), $\left(\mathbf{u}_1^h\right)^{n+\alpha_f}$ is the fluid velocity defined by coefficients $\mathbf{U}^{n+\alpha_f}$, $\left(\mathbf{u}_2^h\right)^{n+\alpha_f}$ is the structure velocity defined by coefficients $\dot{\mathbf{Y}}^{n+\alpha_f}$, and $\mathbf{n}_2^{n+\alpha_f}$ is the normal to $\Gamma_{t+\alpha_f}$, as determined by the displacement coefficients $\mathbf{Y}^{n+\alpha_f}$.

To motivate the development of the multiplier update step, consider the case of $r = 0$. If $R^{n+\alpha} = 0$ and $r = 0$, then the normal component of the α-level penalty force, $\tau^B_{\text{NOR}} R^{n+\alpha}$, will be zero and the normal α-level fluid–structure force will be due only to the Lagrange multiplier, λ^{n+1}. This suggests the explicit update

$$\lambda^{n+1} \leftarrow \lambda^{n+1} + \tau^B_{\text{NOR}} R^{n+\alpha} \,, \tag{69}$$

in which λ^{n+1} is set equal to the α-level fluid–structure forcing. Equations (54)–(62) are of course no longer satisfied with the updated λ^{n+1}, but we may attempt to iterate the steps

1. Solve (54)–(62) with λ^{n+1} fixed.
2. Upate λ^{n+1} by (69):
$$\lambda^{n+1} = \lambda^{n} + \tau^B_{\text{NOR}} R^{n+\alpha} \,. \tag{70}$$

until $\|R^{n+\alpha}\|_{L^2(\Gamma_t)}$ is converged to some tolerance. Note that, in the case of $r > 0$, (70) is an implicit formula, because $R^{n+\alpha}$ depends on λ^{n+1}. It can be trivially recast in explicit form, though:

$$\lambda^{n+1} = \frac{\lambda^n + \tau^B_{\text{NOR}} \left(\left(\mathbf{u}^h_1\right)^{n+\alpha_f} - \left(\mathbf{u}^h_2\right)^{n+\alpha_f} \right) \cdot \mathbf{n}^{n+\alpha_f}_2}{1+r} \,. \tag{71}$$

As explained in [16, Section 4.2.1], the $r = 0$ case of this iteration corresponds to the classic augmented Lagrangian algorithm of Hestenes [96] and Powell [97], which is an implicit variant of the well-known Uzawa iteration [98, 99] for solving saddle point problems. For $r = 0$, though, the convergence criterion of $\|R^{n+\alpha}\|_{L^2(\Gamma_t)} < \epsilon$ is too strict to arrive at a non-locking solution; it effectively demands pointwise constraint satisfaction between the non-matching discrete velocity spaces of the fluid and structure. Our earlier study [16] found accordingly that the iteration did not typically converge, but we circumvented this difficulty by truncating to a single pass, leading to the semi-implicit time marching scheme of first solving (54)–(62) with $\lambda^{n+1} = \lambda^n$, then updating λ^{n+1} by (70) and continuing directly to the next time step. This time splitting approach proved effective for transient problems, but may be expected to run into difficulties in problems that approach steady solutions and choosing $r > 0$ can improve robustness.

Although the stabilization provided by choosing $r > 0$ affords the possibility of fully-implicit time integration, which is typically recommended for complex FSI problems [70], semi-implicit integration procedures can greatly reduce computational cost. The present semi-implicit algorithm is in fact stable, in an energetic sense, even when $r = 0$. This is discussed physically in [23, Section 3.2] and analyzed mathematically in the context of linear model problems in Section 3. This is in contrast to “staggered” or “loosely coupled” FSI methods which are notoriously unstable, especially when the fluid is incompressible or the structure is light [100]. The use of $r > 0$ allows for robustness even when energy is continuously added to the system, as through an inhomogeneous boundary condition. Some caution is warranted, however, in perturbing the kinematic constraint. Section 3.1 of [23] provides an illustrative example of the effects of this consistency error that can be used to estimate its impact.

2.5.3. Block iterative solution of the implicit problem

The implicit step of the semi-implicit time integration algorithm of Section 2.5.2 amounts to a penalty regularization of fluid–structure coupling, with a prescribed loading $\lambda^n \mathbf{n}^{n+\alpha_f}$ along $\Gamma^{n+\alpha_f}$. Because the penalty is not solely responsible for fluid–structure coupling, its value can be moderate, rendering the regularized problem much easier to solve than fully-implicit fluid–structure coupling. We find that a simple block-iterative procedure that alternates between computing fluid and structure solution increments is practical, even for "difficult" applications, such as heart valve simulation, in which a light structure interacts with a heavy, incompressible fluid.

Let $R_\mathrm{f}(u_\mathrm{f}, u_\mathrm{s})$ denote the nonlinear residual for the fully-discrete fluid subproblem at a particular time step, which depends on the discrete fluid and structure solutions, u_f and u_s. Likewise, $R_\mathrm{s}(u_\mathrm{f}, u_\mathrm{s})$ is the residual for the discrete structure subproblem. Then the block-iterative procedure to find a root of $(R_\mathrm{f}, R_\mathrm{s})$ is to start with predictors for u_f and u_s, then repeat the steps

1. Assemble $R_\mathrm{s}(u_\mathrm{f}, u_\mathrm{s})$ and a (typically approximate) tangent matrix, $A_\mathrm{s} \approx \partial R_\mathrm{s}/\partial u_\mathrm{s}$.
2. Solve $A_\mathrm{s} \Delta u_\mathrm{s} = -R_\mathrm{s}$ for the structure solution increment.
3. Update the structure solution: $u_\mathrm{s} \leftarrow u_\mathrm{s} + \Delta u_\mathrm{s}$.
4. Assemble $R_\mathrm{f}(u_\mathrm{f}, u_\mathrm{s})$ and $A_\mathrm{f} \approx \partial R_\mathrm{f}/\partial u_\mathrm{f}$. Note that the assembly uses the updated structure solution u_s.
5. Solve the linear system $A_\mathrm{f} \Delta u_\mathrm{f} = -R_\mathrm{f}$ for the fluid solution increment.
6. Update the fluid solution: $u_\mathrm{f} \leftarrow u_\mathrm{f} + \Delta u_\mathrm{f}$.

In problems where one subproblem's solution is prescribed (as in the examples of Section 3.3), this algorithm becomes Newton iteration for the active subproblem. We frequently select the resolution of the nonlinear algebraic solution by choosing a fixed number of iterations, which may be interpreted as a predictor–multi-corrector scheme based on Newton's method [94].

For the computations in this paper, the matrix A_f is inverted approximately using parallel linear solvers from the Portable, Extensible Toolkit for Scientific Computation (PETSc) [101–103]. In some computations, we find that the desired level of accuracy can be obtained at lower computational cost by reusing the fluid subproblem tangent A_f assembled from the predictor instead of reassembling it each block iteration. Additional details on solver configurations are stated, when relevant, for computations described in the sequel. The matrix A_s is inverted approximately using a serial implementation of the conjugate gradient method [104]. Some minor approximations to A_s

ensure the requisite symmetry. The possibility of using different solvers for the fluid and structure subproblems highlights the flexibility of block iteration.

The fact that this procedure is stable when applied to the problem of heart valve FSI, in which the fluid is much more massive than the structure, is perhaps surprising to researchers familiar with Dirichlet-to-Neumann fluid–structure coupling, where the structure velocity is applied as a Dirichlet boundary condition on the fluid and the fluid traction is applied as a Neumann boundary condition on the structure. With that style of coupling, block iteration may be unstable for any time step size, no matter how small, if the fluid is incompressible and heavy (relative to the structure) [100]. Section 4 analyzes the stability and convergence of the block iteration algorithm in the context of penalty coupling between two linear elliptic problems, confirming that it is unconditionally stable, but perhaps slow to converge for excessively-large penalty parameters or time steps.

2.5.4. Discussion

Some reinterpretation of the algorithm stated in Section 2.5.2 helps to build an intuitive understanding of its properties and lays the groundwork for the more precise analysis given in Section 3. When $r = 0$, the multiplier becomes an accumulation of penalty tractions from previous time steps. This is equivalent to replacing the multiplier and normal penalty terms

$$\int_{\Gamma_t} (\mathbf{w}_1 - \mathbf{w}_2) \cdot (\lambda \mathbf{n}_2)\, d\Gamma + \int_{\Gamma_t} ((\mathbf{w}_1 - \mathbf{w}_2) \cdot \mathbf{n}_2)\, \tau^B_{\mathrm{NOR}} \left((\mathbf{u}_1 - \mathbf{u}_2) \cdot \mathbf{n}_2\right)\, d\Gamma \tag{72}$$

by a penalization of (a backward Euler evaluation of) the time integral of normal velocity differences on the immersed surface Γ_t

$$\begin{aligned}\int_{\Gamma_t} \Bigg\{ &\frac{\tau^B_{\mathrm{NOR}}}{\Delta t} (\mathbf{w}_1(\mathbf{x},t) - \mathbf{w}_2(\mathbf{x},t)) \cdot \mathbf{n}_2(\mathbf{x},t) \\ &\times \int_0^t \Big(\mathbf{u}_1(\boldsymbol{\varphi}_\tau(\boldsymbol{\varphi}_t^{-1}(\mathbf{x})),\tau) - \mathbf{u}_2(\boldsymbol{\varphi}_\tau(\boldsymbol{\varphi}_t^{-1}(\mathbf{x})),\tau)\Big) \cdot \mathbf{n}_2(\boldsymbol{\varphi}_\tau(\boldsymbol{\varphi}_t^{-1}(\mathbf{x})),\tau)\, d\tau \Bigg\}\, d\Gamma\,,\end{aligned} \tag{73}$$

where $\boldsymbol{\varphi}_\tau(\mathbf{X})$ gives the spatial position at time τ of material point $\mathbf{X} \in \Gamma_0$ and the measure $d\Gamma$ corresponds to the integration variable $\mathbf{x} \in \Gamma_t$. That the time integral in (73) is evaluated using the backward Euler method is demonstrated as follows. First define (at fixed $\mathbf{X}$)

$$\lambda^{\mathrm{reg}}(t) = \frac{\tau^B_{\mathrm{NOR}}}{\Delta t} \int_0^t (\mathbf{u}_1(\tau) - \mathbf{u}_2(\tau)) \cdot \mathbf{n}_2(\tau)\, d\tau\,. \tag{74}$$

The time rate-of-change of the integral λ^{reg} is

$$(\dot{\lambda^{\text{reg}}}) = \left.\frac{\partial \lambda^{\text{reg}}}{\partial t}\right|_{\mathbf{X}} = \frac{\tau^B_{\text{NOR}}}{\Delta t} (\mathbf{u}_1 - \mathbf{u}_2) \cdot \mathbf{n}_2 \ . \tag{75}$$

The normal forcing on Γ in the implicit step of the semi-implicit time integrator is designated

$$(\lambda^{\text{reg}})^{n+1} = (\lambda^{\text{reg}})^n + \Delta t (\dot{\lambda^{\text{reg}}})^{n+1} \tag{76}$$

where $(\lambda^{\text{reg}})^n$ is a sum of all previous approximations of λ and $\Delta t (\dot{\lambda^{\text{reg}}})^{n+1}$ is the current time step's penalty forcing, i.e. $\tau^B_{\text{NOR}} \left(\mathbf{u}_1^{n+\alpha_f} - \mathbf{u}_2^{n+\alpha_f} \right) \cdot \mathbf{n}_2^{n+\alpha_f}$. Equation (76) is precisely the backward Euler algorithm for computing λ^{reg}. Thus the forcing (73) is accounted for in a fully implicit manner within the discrete solution process, using a manifestly stable time integrator.

In the case of $r > 0$, we can draw a similar analogy. If the α-level normal penalty force and λ^{n+1} are again designated as $(\lambda^{\text{reg}})^{n+1}$, it is straightforward to see that λ^{reg} advances through time by backward Euler evaluation of the differential equation

$$\frac{1}{(1+r)} \left.\frac{\partial \lambda^{\text{reg}}}{\partial t}\right|_{\mathbf{X}} = \frac{\tau^B_{\text{NOR}}}{\Delta t} (\mathbf{u}_1 - \mathbf{u}_2) \cdot \mathbf{n}_2 - \frac{r}{\Delta t (1+r)} \lambda^{\text{reg}} \ . \tag{77}$$

Intuitively, it is clear that the additional term causes an exponential decay of λ^{reg} in the absence of constraint violation, which highlights its stabilizing effect on the multiplier field. One can quickly check that this reduces to (75) in the case of $r = 0$.

As we first pointed out in [16, Section 4.3], the degeneration of Nitsche's method to a velocity penalty and the time-continuous interpretation of the semi-implicit algorithm with $r = 0$ may both be interpreted as special cases of an existing framework for enforcing Dirichlet boundary conditions on the unsteady Navier–Stokes equation. Goldstein et al. [105] proposed to apply concentrated surface forcing of the form

$$\mathbf{f}(\mathbf{x}_s, t) = \alpha \int_0^t \mathbf{u}_1(\mathbf{x}_s, \tau) \, d\tau + \beta \mathbf{u}_1(\mathbf{x}_s, t) \ , \tag{78}$$

for all $\mathbf{x}_s$ on a stationary solid boundary (i.e. $\mathbf{u}_2 = \mathbf{0}$) with (dimensional) parameters $\alpha \leq 0$ and $\beta \leq 0$. Goldstein et al. interpreted this method, which we will refer to as the feedback method, in the context of control theory, arguing heuristically that it provides negative feedback in the case of constraint violation. This method is frequently passed over as a historical curiosity in literature reviews of immersed boundary CFD and FSI, and dismissed with criticisms of its arbitrary penalty parameters and numerical stiffness, but the feedback boundary condition and related methods remain in use today by numerous research groups, for both direct numerical simulation (DNS) of flow physics phenomena and engineering analysis of difficult FSI problems.

The initial implementation of [105] used a spectral discretization of the fluid (based on the DNS method used in [106]) and applied $O(h)$ smoothing to filter the concentrated forces, reducing pollution effects due to the global nature of the spectral basis functions (cf. [107, Chapter I, Section 2]). Goldstein and collaborators continue to use this methodology for DNS of turbulent flows with nontrivial boundary geometries [108–111]. Saiki and Biringen [112, 113] extended the concept of feedback forcing to finite difference fluid discretizations, using bilinear interpolation within grid cells to evaluate velocity at quadrature points of the immersed boundary and also to distribute concentrated feedback forces to grid points. Reference [112] documents the first application of the approach to moving boundaries, in which (78) becomes

$$\mathbf{f}(\boldsymbol{\varphi}_t(\mathbf{X}_s), t) = \alpha \int_0^t (\mathbf{u}_1(\boldsymbol{\varphi}_\tau(\mathbf{X}_s), \tau) - \mathbf{U}_2(\mathbf{X}_s, \tau))\, d\tau + \beta\, (\mathbf{u}_1(\boldsymbol{\varphi}_\tau(\mathbf{X}_s), \tau) - \mathbf{U}_2(\mathbf{X}_s, \tau)) \ , \tag{79}$$

where $\boldsymbol{\varphi}_t(\mathbf{X}_s)$ represents the position at time t of a material point $\mathbf{X}_s$ on the moving boundary, which moves with velocity $\mathbf{U}_2(\mathbf{X}_s, t)$. This extension naturally suggests application to FSI, and a recent series of papers by Huang, Sung, and collaborators has demonstrated that feedback forcing is a robust and accurate approach for the simulation of light flexible structures immersed in incompressible flows [114–118]. A similar immersed boundary approach has been used in the commercial code LS-DYNA [119] for decades, to study automobile airbag inflation and other challenging FSI problems [120–123], including heart valve simulation [7, 13, 21, 124]. LS-DYNA documentation refers to this capability as the “constrained Lagrange in solid” formulation. We have seen no documentation explicitly relating this to Goldstein et al.’s feedback approach, and assume that it was arrived at independently. The repeated rediscovery of this formulation by engineers studying difficult CFD and FSI problems suggests an inherent robustness to the approach.

The above studies all relied on explicit or semi-implicit time integration schemes, which placed stability restrictions on α and β relative to Δt. Much attention has therefore been paid to the temporal stability of explicitly-integrated feedback forces. The most comprehensive study of the temporal stability of feedback forcing is [125]. To our knowledge, though, no previous attempt has been made by numerical analysts to prove the convergence of the feedback boundary condition method to the Dirichlet boundary value problem that it is intended to approximate. In Section 3.1.3, we study the convergence of feedback boundary conditions in the context of a linear parabolic model problem, as a stepping-stone to the analysis of our semi-implicit time integrator for the augmented Lagrangian system.

3. Convergence of the semi-implicit integration

A critical question to address is whether the proposed semi-implicit time integration of the augmented Lagrangian is a fundamentally sound approach for enforcing Dirichlet boundary conditions in parabolic problems. Despite the closely-related feedback boundary condition's decades-long history of successful application to CFD and FSI (as reviewed in Section 2.5.4), we could not find any *a priori* analysis of its convergence. To investigate the convergence of our approach, we first introduce a linear, scalar model problem and prove convergence in that setting. We then discuss some simple extensions to problems that are more representative of FSI. We include numerical experiments indicating that our *a priori* analysis is not sharp; convergence is, in practice, faster than predicted. Throughout this section, we follow the common practice of considering the symbol "C" to stand for a generic constant that is independent of refinement parameters, but may represent different numerical values in different places.

3.1. Scalar parabolic model problem

We begin by analyzing the behavior of our semi-implicit time integrator applied to a scalar parabolic problem with immersed boundaries. To summarize, the main steps of our analysis are:

- Relate the semi-implicit time-integration of the scalar parabolic problem to implicit time integration of a regularized feedback boundary condition problem with h- and Δt-dependent coefficients (Section 3.1.2).
- Show that solutions of the regularized problem converge to solutions of the original parabolic problem (Section 3.1.3).
- Analyze the spatial discretization error of the semi-discrete regularized problem (Section 3.1.5).
- Quantify the truncation error in time of implicit time integration of the semi-discrete regularized problem (Section 3.1.7).

3.1.1. Scalar parabolic problem statement

As in Section 2.1, we begin from a problem stated in weak form to more naturally accommodate the singular distributional forcing associated with immersed boundaries. A scalar field u, which we refer to as temperature, evolves through time according to a second-order parabolic PDE resembling the heat equation on a domain $\Omega \subset \mathbb{R}^d$, while satisfying homogeneous Dirichlet boundary conditions on $\partial\Omega$ and being constrained to have its trace on the immersed surface Γ equal to the function g, defined on Γ. An example of such a configuration is shown in Figure 1. In weak form, using a Lagrange multiplier to enforce the constraint on Γ, the problem is: Find

$u \in L^2(0,T;H_0^1(\Omega))$ with $\partial_t u \in L^2(0,T;H^{-1}(\Omega))$ and $\lambda \in L^2(0,T;H^{-1/2}(\Gamma))$ such that for every $v \in H_0^1(\Omega)$ and $\delta\lambda \in H^{-1/2}(\Gamma)$ at a.e. $t \in [0,T]$,

$$\begin{aligned} \rho_{H^{-1}(\Omega)}\langle \partial_t u(t), v\rangle_{H^1(\Omega)} + a(u(t),v) + {}_{H^{-1/2}(\Gamma)}\langle \lambda(t), \gamma v\rangle_{H^{1/2}(\Gamma)} - {}_{H^{-1/2}(\Gamma)}\langle \delta\lambda, \gamma u(t)\rangle_{H^{1/2}(\Gamma)} \\ = {}_{H^{-1/2}(\Gamma)}\langle \delta\lambda, -g(t)\rangle_{H^{1/2}(\Gamma)} + (f(t),v)_{L^2(\Omega)} \end{aligned} \tag{80}$$

and

$$u(0) = u_0 \in L^2(\Omega)\,, \tag{81}$$

where $\rho > 0$ is a scalar coefficient, γ is the trace operator mapping from $H^1(\Omega)$ to $H^{1/2}(\Gamma)$, ${}_{A^*}\langle\cdot,\cdot\rangle_A$ is a duality pairing between a space A and its dual, a is a bilinear form that is coercive and bounded over $H_0^1(\Omega)$, u_0 is an initial condition for u at time $t = 0$, $g(t)$ is the Dirichlet boundary data on Γ at time t, and $f(t)$ is a prescribed source term driving the temperature. For background on the time-dependent spaces used in defining this problem, and an appropriate weak definition of the time derivative ∂_t, see [126, Section 5.9.2]. In particular, the meaningfulness of assigning an $L^2(\Omega)$ initial condition to u at the point $t = 0$ is assured by [126, Section 5.9.2, Theorem 3(i)]. If Γ divides Ω into two subdomains, as in Figure 1, the existence, uniqueness, and regularity theory for second-order parabolic problems with Dirichlet boundary conditions can be applied in each subdomain. We make the important assumption that the Lagrange multiplier λ is in $L^2(\Gamma) \subset H^{-1/2}(\Gamma)$. This greatly simplifies comparisons between (80) and the regularized problem (85) introduced below, in which the surface force field corresponding to a regularized multiplier is in $L^2(\Gamma)$. We introduce further regularity assumptions on u and λ, as needed to complete the arguments below. Implicit in these assumptions are regularity constraints on Ω, Γ, f, and g, but, for brevity, we simply state their effects directly. A discussion of the effects of problem data on regularity of solutions to second-order parabolic problems may be found in [126, Section 7.1.3].

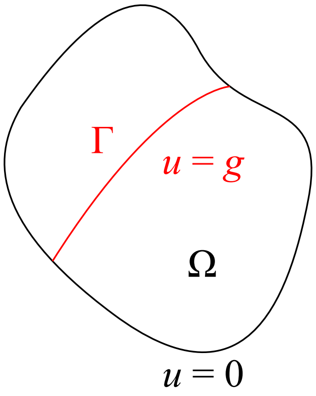

Figure 1: The domain Ω and the immersed boundary Γ.

3.1.2. Semi-implicit time integration

We now define a semi-implicit algorithm for this scalar model problem that is analogous to the scheme proposed for nonlinear FSI in Section 2.5. At each time step,

1. Given u^n and λ^n, find u^{n+1} such that for all $v \in H^1_0(\Omega)$,

$$\begin{aligned}\rho(u_t^{n+1}, v)_{L^2(\Omega)} + a(u^{n+1}, v) + (\lambda^n, \gamma v)_{L^2(\Gamma)} + \beta(\gamma u^{n+1} - g(t^{n+1}), \gamma v)_{L^2(\Gamma)} \\ = (f(t^{n+1}), v)_{L^2(\Omega)} \,,\end{aligned} \tag{82}$$

   where

$$u_t^{n+1} = \frac{u^{n+1} - u^n}{\Delta t} \,. \tag{83}$$

2. Update the multiplier such that, for all $\delta\lambda \in L^2(\Gamma)$,

$$(\lambda^{n+1}, \delta\lambda)_{L^2(\Gamma)} = \frac{1}{1+r}\left(\lambda^n + \beta(\gamma u^{n+1} - g(t^{n+1})), \delta\lambda\right)_{L^2(\Gamma)} \,. \tag{84}$$

As we explained in Section 2.5.4, in the context of FSI, this is a backward Euler time integration of a regularized problem: Find $u^{\text{reg}} \in L^2(0, T; H^1_0(\Omega))$ with $\partial_t u^{\text{reg}} \in L^2(0, T; H^{-1}(\Omega))$ and $\lambda^{\text{reg}} \in L^2(0, T; L^2(\Gamma))$ with $\partial_t \lambda^{\text{reg}} \in L^2(0, T; L^2(\Gamma))$ such that for all $v \in H^1_0(\Omega)$ and $\delta\lambda \in L^2(\Gamma)$ at a.e. $t \in [0, T]$,

$$\begin{aligned}&\rho_{H^{-1}(\Omega)}\langle \partial_t u^{\text{reg}}, v\rangle_{H^1(\Omega)} + a(u^{\text{reg}}, v) + (\lambda^{\text{reg}}, \gamma v)_{L^2(\Gamma)} \\ &\quad + \left(\frac{\Delta t}{(1+r)\beta}\partial_t \lambda^{\text{reg}} - (\gamma u^{\text{reg}} - g) + \frac{r}{(1+r)\beta}\lambda^{\text{reg}}, \delta\lambda\right)_{L^2(\Gamma)} \\ &\quad = (f, v)_{L^2(\Omega)} \,,\end{aligned} \tag{85}$$

$$u^{\text{reg}}(0) = u_0 \in L^2(\Omega) \,, \tag{86}$$

and

$$\lambda^{\text{reg}}(0) = \lambda_0 \in L^2(\Gamma) \,. \tag{87}$$

The meaningfulness of assigning an $L^2(\Gamma)$ initial condition to λ^{reg} at the point $t = 0$ is assured by [126, Section 5.9.2, Theorem 2(i)], with $X = L^2(\Gamma)$. Note that, as in Section 2.5.4, $\lambda^{\text{reg}}(t^n)$ corresponds to $(1 + r)\lambda^n$ in the semi-implicit algorithm.

The existence and uniqueness of solutions to the problem (85) for constant values of β and Δt follows from the usual Faedo–Galerkin argument for parabolic problems, which is executed in detail for the heat equation in [126, Section 7.1.2]. Briefly, existence theory for ordinary differential equations is applied to a sequence of Galerkin approximations and uniform energy bounds on the sequence of solutions are used to obtain a unique weak limit satisfying the weak PDE. In adapting the proof from [126, Section 7.1.2], a suitable basis for approximating λ^{reg} would be the eigenfunctions of the Laplace–Beltrami operator on Γ. This does *not* imply any sort of uniformity of energy estimates with respect to the limits $\beta \to \infty$ and/or $\Delta t \to 0$. Robustness in those limits will be derived separately in the sequel.

3.1.3. Convergence of the regularized problem

Our first step toward showing that the output of the semi-implicit algorithm converges to a solution of the parabolic problem (80) will be to show that the solution of the regularized problem (85) converges to the solution of (80). This portion of our analysis may be of interest beyond the narrow context of studying our semi-implicit algorithm, as the convergence of (85) to (80) is applicable to other discretizations of feedback boundary conditions. (Nearly all of the examples cited in Section 2.5.4 used explicit time integration.) We denote the error between the solutions to (80) and (85) by

$$(e_u, e_\lambda) = (u^{\mathrm{reg}} - u, \lambda^{\mathrm{reg}} - \lambda)\ . \tag{88}$$

We will derive a bound on the $L^2(\Omega)$ error in temperature at time T by bounding the energy norm

$$|||e_u(T), e_\lambda(T)|||^2 = \frac{1}{2}\rho\, \|e_u(T)\|^2_{L^2(\Omega)} + \frac{\Delta t}{2(1+r)\beta}\, \|e_\lambda(T)\|^2_{L^2(\Gamma)}\ . \tag{89}$$

Taking the difference between (85) and (80) (restricting $\delta\lambda$ in (80) to $L^2(\Gamma) \subset H^{-1/2}(\Gamma)$ and recalling the assumptions that $\lambda(t)$ and $\partial_t\lambda(t)$ are in $L^2(\Gamma)$ for a.e. $t \in [0, T]$),

$$\rho_{H^{-1}(\Omega)}\langle \partial_t e_u, v\rangle_{H^1(\Omega)} + a(e_u, v) + (e_\lambda, \gamma v)_{L^2(\Gamma)} + \left(\frac{\Delta t}{(1+r)\beta}\partial_t\lambda^{\mathrm{reg}} - \gamma e_u + \frac{r}{(1+r)\beta}\lambda^{\mathrm{reg}}, \delta\lambda\right)_{L^2(\Gamma)} = 0\ . \tag{90}$$

Add and subtract

$$\left(\frac{\Delta t}{(1+r)\beta}\partial_t\lambda + \frac{r}{(1+r)\beta}\lambda, \delta\lambda\right)_{L^2(\Gamma)} \tag{91}$$

from the left-hand side of (90) to obtain

$$\begin{aligned} &\rho_{H^{-1}(\Omega)}\langle \partial_t e_u, v\rangle_{H^1(\Omega)} + a(e_u, v) + (e_\lambda, v)_{L^2(\Gamma)} + \left(\frac{\Delta t}{(1+r)\beta}\partial_t e_\lambda - e_u + \frac{r}{(1+r)\beta}e_\lambda, \delta\lambda\right)_{L^2(\Gamma)} \\ &\quad + \left(\frac{\Delta t}{(1+r)\beta}\partial_t\lambda + \frac{r}{(1+r)\beta}\lambda, \delta\lambda\right)_{L^2(\Gamma)} = 0\ . \end{aligned} \tag{92}$$

Setting $v = e_u$ and $\delta\lambda = e_\lambda$, then applying [126, Section 5.9.2, Theorem 3(ii)] to simplify the $H^1(\Omega)$ duality pairing,

$$\partial_t \vert\!\vert\!\vert e_u, e_\lambda \vert\!\vert\!\vert^2 = -a(e_u, e_u) - \frac{r}{(1+r)\beta}\|e_\lambda\|^2_{L^2(\Gamma)} - \frac{\Delta t}{(1+r)\beta}(\partial_t\lambda, e_\lambda)_{L^2(\Gamma)} - \frac{r}{(1+r)\beta}(\lambda, e_\lambda)_{L^2(\Gamma)} \,. \tag{93}$$

Applying Young's inequality to the last two terms above,

$$\begin{aligned}\partial_t \vert\!\vert\!\vert e_u, e_\lambda \vert\!\vert\!\vert^2 \leq& - a(e_u, e_u) - \frac{r}{2(1+r)\beta}\|e_\lambda\|^2_{L^2(\Gamma)} + \frac{\Delta t}{2(1+r)\beta}\left(T\|\partial_t\lambda\|^2_{L^2(\Gamma)} + \frac{1}{T}\|e_\lambda\|^2_{L^2(\Gamma)}\right)\\ &+ \frac{r}{2(1+r)\beta}\|\lambda\|^2_{L^2(\Gamma)} \,.\end{aligned} \tag{94}$$

Adding the non-negative term

$$+\frac{\rho}{2T}\|e_u\|^2_{L^2(\Omega)} + a(e_u, e_u) + \frac{r}{2(1+r)\beta}\|e_\lambda\|^2_{L^2(\Gamma)} \tag{95}$$

to the right-hand side,

$$\partial_t \vert\!\vert\!\vert e_u, e_\lambda \vert\!\vert\!\vert^2 \leq \frac{1}{T}\vert\!\vert\!\vert e_u, e_\lambda \vert\!\vert\!\vert^2 + \frac{T\Delta t}{2(1+r)\beta}\|\partial_t\lambda\|^2_{L^2(\Gamma)} + \frac{r}{2(1+r)\beta}\|\lambda\|^2_{L^2(\Gamma)} \,. \tag{96}$$

Then Grönwall's lemma bounds the error at time T:

$$\vert\!\vert\!\vert e_u(T), e_\lambda(T) \vert\!\vert\!\vert^2 \leq C\int_0^T \left(\frac{T\Delta t}{2(1+r)\beta}\|\partial_t\lambda\|^2_{L^2(\Gamma)} + \frac{r}{2(1+r)\beta}\|\lambda\|^2_{L^2(\Gamma)}\right) dt \,, \tag{97}$$

assuming $e_u(0) = e_\lambda(0) = 0$. Thus

$$\frac{\rho}{2}\|e_u\|^2_{L^2(\Omega)} \leq \vert\!\vert\!\vert e_u, e_\lambda \vert\!\vert\!\vert^2 \to 0 \tag{98}$$

as $\beta \to \infty$. In the case of $r = 0$, we have this convergence when $\Delta t \to 0$ at fixed β. A formally similar argument produces an analogous estimate for $(\rho/2)\|\partial_t^N e_u\|^2_{L^2(\Omega)}$ with $N \geq 1$, so long as the solution to (80) has sufficiently many time derivatives in $L^2(\Gamma)$:

$$\left\vert\!\left\vert\!\left\vert \partial_t^N e_u(T), \partial_t^N e_\lambda(T) \right\vert\!\right\vert\!\right\vert^2 \leq C\int_0^T \left(\frac{T\Delta t}{2(1+r)\beta}\|\partial_t^{N+1}\lambda\|^2_{L^2(\Gamma)} + \frac{r}{2(1+r)\beta}\|\partial_t^N\lambda\|^2_{L^2(\Gamma)}\right) dt \,. \tag{99}$$

Ensuring that $\partial_t^N e_u(0) = \partial_t^N e_\lambda(0) = 0$ (as assumed for the $N = 0$ case above, to arrive at (97)) requires the assumption that the multiplier solution $\lambda(t)$ of (80) evolves sufficiently smoothly from an initial value of zero. This is a somewhat restrictive assumption, but still admits many nontrivial solutions. For example, it can easily be satisfied by starting up the forcing functions $f(t)$ and $g(t)$

smoothly, to disturb a homogeneous initial temperature field. We ignore this condition altogether in numerical experiments, with no apparent effect on the convergence of the method.

Remark 6. Similar assumptions on problem data derivatives at $t = 0$ are made in [127, Section 4.3], while analyzing the convergence of an artificial compressibility scheme. The cited work acknowledges that these restrictions are not especially realistic and [127, Remark 4.2] suggests that they might be weakened by using time-weighted norms, referring to [128, Lemma 3.2] as an example. The numerical examples of [127, Section 6] ignore the assumptions about data at $t = 0$ while still exhibiting the desired convergence rates.

Remark 7. It is clear from the numerical experiments in the sequel that the rates of convergence with respect to β and Δt are not sharp. We have sketched proofs of some sharper estimates, based on adapting the duality arguments in [129, Section 2.3], which we hope to complete and publish in the near future.

Remark 8. One might also try to optimize the choices of r and β, to minimize e_u and e_λ, but such optimizations can come into conflict with competing demands on these parameters, from the spatial discretization. For instance, faster convergence of e_u with respect to Δt can be obtained by selecting $r = C\Delta t/T$ above, but this hurts convergence of the bound (125) on spatial discretization error below.

3.1.4. Uniform bound in $H^{3/2-\epsilon}(\Omega)$

To obtain useful interpolation errors in finite element spaces, we will need to bound $u^{\text{reg}}(T)$ in a stronger norm than $H^1(\Omega)$. A uniform bound on u^{reg} in the $H^{3/2-\epsilon}(\Omega)$ norm may be found using elliptic regularity given a uniform $L^2(\Gamma)$ bound on λ^{reg}. In the case of $r = O(\Delta t)$, such a uniform bound follows immediately from (97). If r goes to zero more slowly than $C\Delta t$, we must prove the uniform bound on $\|\lambda^{\text{reg}}\|_{L^2(\Gamma)}$ separately. This is the case of interest, since we anticipate using $r = C$.

Assume that $\beta > 0$, $\Delta t = C/\beta$, and $r = C$, and consider norms of (time derivatives of) the solution to the original problem (80) to be constant (since this solution is independent of β and Δt). Then, for β sufficiently large, (99) can be re-written as

$$|\!|\!|\partial_t e_u(T), \partial_t e_\lambda(T)|\!|\!|^2 \le \frac{C}{\beta}\,. \tag{100}$$

This implies

$$\frac{\rho}{2}\|\partial_t e_u(T)\|^2_{L^2(\Omega)} \le \frac{C}{\beta} \tag{101}$$

$$\Rightarrow \|\partial_t e_u(T)\|_{L^2(\Omega)} \le \frac{C}{\sqrt{\beta}} \tag{102}$$

and

$$
\begin{aligned}
&\frac{\Delta t}{2(1+r)\beta}\,\|\partial_t e_\lambda(T)\|^2_{L^2(\Gamma)} \le \frac{C}{\beta} && (103)\\
&\Rightarrow \|\partial_t e_\lambda(T)\|^2_{L^2(\Gamma)} \le C\beta && (104)\\
&\Rightarrow \left\|\frac{\Delta t}{(1+r)\beta}\partial_t e_\lambda(T)\right\|_{L^2(\Gamma)} \le \frac{C}{\beta^{3/2}}\ . && (105)
\end{aligned}
$$

The above-bounded terms may be cast as part of the prescribed forcing in an elliptic problem for the error at time T. Consider re-arranging (92) at time T into the problem: Find $e_u(T)$ and $e_\lambda(T)$ such that for all v and $\delta\lambda$

$$
\begin{aligned}
&a(e_u(T),v) + (e_\lambda(T),v)_{L^2(\Gamma)} - (e_u(T),\delta\lambda)_{L^2(\Gamma)} + \frac{r}{(1+r)\beta}\,(e_\lambda(T),\delta\lambda)_{L^2(\Gamma)}\\
&= -\rho(\partial_t e_u(T),v)_{L^2(\Omega)} - \left(\frac{\Delta t}{(1+r)\beta}\partial_t e_\lambda(T),\delta\lambda\right)_{L^2(\Gamma)} - \left(\frac{\Delta t}{(1+r)\beta}\partial_t\lambda(T) + \frac{r}{(1+r)\beta}\lambda(T),\delta\lambda\right)_{L^2(\Gamma)}\ ,
\end{aligned}
\tag{106}
$$

where $\partial_t e_u(T)$ and $\partial_t e_\lambda(T)$ on the right-hand side of the equation are *not* considered to be unknown. In (106), these functions are fixed data, subject to the bounds (102) and (105). The left-hand side bilinear form of (106),

$$
B_{\text{steady}}((u,\lambda),(v,\delta\lambda)) = a(u,v) + (\lambda,v)_{L^2(\Gamma)} - (u,\delta\lambda)_{L^2(\Gamma)} + \frac{r}{(1+r)\beta}\,(\lambda,\delta\lambda)_{L^2(\Gamma)}\ , \tag{107}
$$

is coercive and bounded in the norm

$$
\|u,\lambda\|^2_{\text{steady}} = \beta\|u\|^2_{H^1(\Omega)} + \|\lambda\|^2_{L^2(\Gamma)}\ . \tag{108}
$$

The coercivity constant is clearly seen to be C/β:

$$
\begin{aligned}
B_{\text{steady}}((u,\lambda),(u,\lambda)) &= a(u,u) + (\lambda,v)_{L^2(\Gamma)} - (\lambda,v)_{L^2(\Gamma)} + \frac{r}{(1+r)\beta}\|\lambda\|^2_{L^2(\Gamma)} && (109)\\
&\ge C\left(\|u\|^2_{H^1(\Omega)} + \frac{1}{\beta}\|\lambda\|^2_{L^2(\Gamma)}\right) && (110)\\
&\ge \frac{C}{\beta}\|u,\lambda\|^2_{\text{steady}}\ . && (111)
\end{aligned}
$$

The dual norm (induced by (108)) of the right-hand side functional,

$$
F_{\text{steady}}((v,\delta\lambda)) = -\rho(\partial_t e_u(T),v)_{L^2(\Omega)} - \left(\frac{\Delta t}{(1+r)\beta}\partial_t e_\lambda(T),\delta\lambda\right)_{L^2(\Gamma)}
$$

$$-\left(\frac{\Delta t}{(1+r)\beta}\partial_t\lambda(T)+\frac{r}{(1+r)\beta}\lambda(T),\delta\lambda\right)_{L^2(\Gamma)}\ , \tag{112}$$

is also C/β, for β sufficiently large. Using the Lax–Milgram theorem to bound the solution of (106) in terms of the coercivity constant and the right-hand side functional norm,

$$\|e_u(T),e_\lambda(T)\|_{\text{steady}}\leq\frac{1}{C/\beta}\left\|F_{\text{steady}}(\cdot)\right\|_{\text{steady}}\leq C\ . \tag{113}$$

Based on the definition of $\|\cdot\|_{\text{steady}}$, (113) provides a β-independent bound on $\|e_\lambda(T)\|_{L^2(\Gamma)}$. Using the uniform bound on $\|\lambda^{\text{reg}}\|_{L^2(\Gamma)}$ which immediately follows,

$$(\lambda^{\text{reg}},\gamma(\cdot))_{L^2(\Gamma)} \tag{114}$$

is bounded independently of β over the set of functions on Ω with traces in $L^2(\Gamma)$. This set of functions is $H^{1/2+\epsilon}(\Omega)$. Thus the functional (114) is in the dual space $H^{-(1/2+\epsilon)}(\Omega)$, and its induced norm is bounded uniformly with respect to β. Using the uniform bound on the $L^2(\Omega)$ norm of $\partial_t e_u$, we may conclude, through elliptic regularity theory, that u^{reg} is bounded in $H^{3/2-\epsilon}(\Omega)$, independently of β.

3.1.5. Spatial discretization of the modified equation

We now consider a semi-discrete counterpart of problem (85), posed over finite element spaces for $u^{\text{reg}}(t)$. We will formally consider $\lambda^{\text{reg}}(t)$ and $\delta\lambda$ to be in the infinite-dimensional space $L^2(\Gamma)$, yet, due to the structure of the problem, λ^{reg} will clearly stay within the finite-dimensional trace space of the discrete temperature so long as its initial condition and the data g are also in this space. This can be verified in the semi-discrete setting by deriving a solution of $\lambda^{\text{reg}}(t)$ in terms of $u^{\text{reg}}(t)$ at a fixed point on Γ (cf. [23, (3.35)–(3.38)]). In the fully-discrete setting, the finite dimensionality of λ^n is clear from its explicit update formula and the closure of the discrete trace space under linear combination. The semi-discrete numerical method is to find $u^h\in V_u^h\subset H_0^1(\Omega)$ and $\lambda^h\in L^2(\Gamma)$ such that, for every $v^h\in V_u^h$ and $\delta\lambda\in L^2(\Gamma)$,

$$\begin{aligned}&\rho(\partial_t u^h,v^h)_{L^2(\Omega)}+a(u^h,v^h)+(\lambda^h,v^h)_{L^2(\Gamma)}\\&\quad+\left(\frac{\Delta t}{(1+r)\beta}\partial_t\lambda^h-\left(u^h-g\right)+\frac{r}{(1+r)\beta}\lambda^h,\delta\lambda\right)_{L^2(\Gamma)}=\left(f,v^h\right)_{L^2(\Omega)}\ .\end{aligned} \tag{115}$$

The $L^2(\Omega)$ inner product used above to represent $\partial_t u^h\in H^{-1}(\Omega)$ is appropriate in the finite dimensional setting. The semi-discrete errors in the velocity and multiplier fields are

$$e_u^{\text{reg}}=u^h-u^{\text{reg}}=(u^h-\bar{u}^h)+(\bar{u}^h-u^{\text{reg}})=\xi_u^h+\eta_u \tag{116}$$

and

$$e_\lambda^{\mathrm{reg}} = \lambda^h - \lambda^{\mathrm{reg}} \;, \tag{117}$$

The function $\bar{u}^h \in V_u^h$ is an arbitrary interpolant, used to split the velocity error into discrete and interpolation components. Because, as discussed above, the multiplier test space is considered to be all of $L^2(\Gamma)$, there is no reason to perform a splitting of the multiplier error, since the "interpolation" component will be zero. The velocity interpolation error is defined as an elliptic projection of u^{reg} into the discrete space V_u^h. Specifically,

$$a(\bar{u}^h, v^h) = a(u^{\mathrm{reg}}, v^h) \qquad \forall v^h \in V_u^h \;. \tag{118}$$

As argued earlier, u^{reg} is uniformly bounded in $H^{3/2-\epsilon}(\Omega)$, so it is reasonable to assume

$$\|\eta_u\|^2_{H^1(\Omega)} \leq Ch^{1-2\epsilon} \;. \tag{119}$$

An Aubin–Nitsche-type duality argument can produce

$$\|\eta_u\|^2_{L^2(\Omega)} \leq Ch^{3-2\epsilon} \;, \tag{120}$$

from which one can obtain

$$\|\eta_u\|^2_{L^2(\Gamma)} \leq Ch^{2-2\epsilon} \tag{121}$$

by assuming a trace estimate on Γ. Using Galerkin orthogonality (i.e. consistency of (115) with (85)) and setting $v^h = \xi_u^h$ and $\delta\lambda = e_\lambda^{\mathrm{reg}}$,

$$\rho(\partial_t e_u^{\mathrm{reg}}, \xi_u^h)_{L^2(\Omega)} + a(e_u^{\mathrm{reg}}, \xi_u^h) + (e_\lambda^{\mathrm{reg}}, \xi_u^h)_{L^2(\Gamma)} + \left(\frac{\Delta t}{(1+r)\beta}\partial_t e_\lambda^{\mathrm{reg}} - e_u^{\mathrm{reg}} + \frac{r}{(1+r)\beta} e_\lambda^{\mathrm{reg}}, e_\lambda^{\mathrm{reg}}\right)_{L^2(\Gamma)} = 0 \;. \tag{122}$$

Invoking the velocity error splitting (116), this becomes

$$\rho(\partial_t \eta_u, \xi_u^h)_{L^2(\Omega)} + \rho(\partial_t \xi_u^h, \xi_u^h)_{L^2(\Omega)} + a(\xi_u^h, \xi_u^h) + \left(\frac{\Delta t}{(1+r)\beta}\partial_t e_\lambda^{\mathrm{reg}} - \eta_u + \frac{r}{(1+r)\beta} e_\lambda^{\mathrm{reg}}, e_\lambda^{\mathrm{reg}}\right)_{L^2(\Gamma)} = 0 \;. \tag{123}$$

Re-arranging terms,

$$\begin{aligned}\partial_t\left(\frac{\rho}{2}\|\xi_u^h\|^2_{L^2(\Omega)} + \frac{\Delta t}{2(1+r)\beta}\|e_\lambda^{\mathrm{reg}}\|^2_{L^2(\Gamma)}\right) = &- \rho(\partial_t \eta_u, \xi_u^h)_{L^2(\Omega)} - a(\xi_u^h, \xi_u^h) + (\eta_u, e_\lambda^{\mathrm{reg}})_{L^2(\Gamma)} \\ &- \frac{r}{(1+r)\beta}\|e_\lambda^{\mathrm{reg}}\|^2_{L^2(\Gamma)} \;.\end{aligned} \tag{124}$$

Applying Young's inequality on the right and adding strictly positive terms to the upper bound,

$$\partial_t \left\| \xi_u^h, e_\lambda^{\text{reg}} \right\|^2 \leq \frac{1}{T} \left\| \xi_u^h, e_\lambda^{\text{reg}} \right\|^2 + \frac{T\rho}{2} \|\partial_t \eta_u\|^2_{L^2(\Omega)} + \frac{2(1+r)\beta}{r} \|\eta_u\|^2_{L^2(\Gamma)} \,. \tag{125}$$

Grönwall's lemma then gives a bound on $\left\| \xi_u^h(T), e_\lambda^{\text{reg}}(T) \right\|$ (and, by triangulation, $\left\| e_u^{\text{reg}}(T), e_\lambda^{\text{reg}}(T) \right\|$) in terms of the interpolation error η_u. The only hazard is that $\|\eta_u\|^2_{L^2(\Gamma)}$ must converge faster than β/r diverges. If $\beta = C/h$, $r = C$, and the interpolation error is bounded like (121), the temperature should converge at a rate $\geq 1/2$ in $L^2(\Omega)$. A similar argument can bound time derivatives of the semi-discrete error, if the problem data is sufficiently nice at $t = 0$ to ensure that $\partial_t^N e_u^{\text{reg}}(0) = \partial_t^N e_\lambda^{\text{reg}}(0) = 0$.

3.1.6. Semi-discrete convergence for $r = 0$

The error bound that follows from (125) clearly fails in the limit of $r \to 0$. Computations with $r = 0$, on the other hand, seem to proceed without major issues and enjoy better conservation properties in the steady limit. Let us first attempt to backtrack in the argument of the previous section. Let us try an alternate approach, starting over from (124). In the case of $r = 0$, (124) becomes

$$\partial_t \left(\frac{\rho}{2} \|\xi_u^h\|^2_{L^2(\Omega)} + \frac{1}{2k} \|e_\lambda^{\text{reg}}\|^2_{L^2(\Gamma)} \right) = -\rho(\partial_t \eta_u, \xi_u^h)_{L^2(\Omega)} - a(\xi_u^h, \xi_u^h) + (\eta_u, e_\lambda^{\text{reg}})_{L^2(\Gamma)} \,, \tag{126}$$

where we have defined $k = \beta/\Delta t$, to simplify notation. Applying Young's inequality to terms in the right-hand side of (126) and adding strictly non-negative terms to the upper bound, we get

$$\partial_t \left\| \xi_u^h, e_\lambda^{\text{reg}} \right\|^2 \leq \frac{1}{T} \left\| \xi_u^h, e_\lambda^{\text{reg}} \right\|^2 + \frac{T\rho}{2} \|\partial_t \eta_u\|^2_{L^2(\Omega)} + \frac{Tk}{2} \|\eta_u\|^2_{L^2(\Gamma)} \,. \tag{127}$$

Using the interpolation estimate (121) and Grönwall's lemma, we obtain (for k sufficiently large)

$$\left\| \xi_u^h(T), e_\lambda^{\text{reg}}(T) \right\|^2 \leq Ckh^{2-\epsilon} \,. \tag{128}$$

Applying $\partial_t^N(\cdot)$ to the trial functions and forcing throughout the entire semi-discrete problem and carrying out a similar analysis,

$$\left\| \partial_t^N \xi_u^h(T), \partial_t^N e_\lambda^{\text{reg}}(T) \right\|^2 \leq Ckh^{2-\epsilon} \,, \tag{129}$$

given sufficient time-regularity of the original problem (80). As with (99), the use of Grönwall's lemma with zero initial time derivatives of the error relies on the assumption that source terms in (80) evolve smoothly from zero, although, as evidenced by the numerical examples, this assumption is likely not strictly necessary for convergence of the numerical method. Based on the scalings

$\beta \sim 1/h$ and $\Delta t \sim h$ assumed above ($\Rightarrow k \sim 1/h^2$), these error estimates are not very appealing; we essentially have that the semi-discrete solution is bounded, but not convergent. We can try to improve on this situation using a duality argument.

To execute the duality argument, we first need to establish $H^1(\Omega)$ stability of the semi-discrete temperature error e_u^{reg}, i.e. $\|e_u^{\text{reg}}(s)\|_{H^1(\Omega)} \leq C$ for all $s \in (0, T)$. In keeping with the goals of the present section, we consider only the case $r = 0$. Recalling the error splitting (116) and the definition of the interpolant $\overline{u}^h$, it is clear that the semi-discrete error satisfies

$$\rho\left(\partial_t e_u^{\text{reg}}, v^h\right)_{L^2(\Omega)} + a\left(\xi_u^h, v^h\right) + \left(e_\lambda^{\text{reg}}, v^h\right)_{L^2(\Gamma)} + \left(\frac{1}{k}\partial_t e_\lambda^{\text{reg}} - e_u^{\text{reg}}, \delta\lambda\right)_{L^2(\Gamma)} = 0 \qquad \forall\left(v^h, \delta\lambda\right) . \tag{130}$$

Setting $\left\{v^h, \delta\lambda\right\} = \left\{\partial_t \xi_u^h, 0\right\}$ and using the symmetry of a,

$$\rho\left(\partial_t e_u^{\text{reg}}, \partial_t \xi_u^h\right)_{L^2(\Omega)} + \frac{1}{2}\partial_t a\left(\xi_u^h, \xi_u^h\right) + \left(e_\lambda^{\text{reg}}, \partial_t \xi_u^h\right)_{L^2(\Gamma)} = 0 . \tag{131}$$

For all $\delta\lambda \in L^2(\Gamma)$, $\left(\xi_u^h + \eta_u, \delta\lambda\right)_{L^2(\Gamma)} = \left(\frac{1}{k}\partial_t e_\lambda^{\text{reg}}, \delta\lambda\right)_{L^2(\Gamma)}$, so (131) implies that

$$\rho\left(\partial_t e_u^{\text{reg}}, \partial_t \xi_u^h\right)_{L^2(\Omega)} + \frac{1}{2}\partial_t a\left(\xi_u^h, \xi_u^h\right) + \left(e_\lambda^{\text{reg}}, \frac{1}{k}\partial_t^2 e_\lambda^{\text{reg}} - \partial_t \eta_u\right)_{L^2(\Gamma)} = 0 . \tag{132}$$

Integrating (132) in time and applying the Cauchy–Schwarz and Young inequalities,

$$\begin{aligned}
& a\left(\xi_u^h(s), \xi_u^h(s)\right) \\
& \quad \leq 2\int_0^s \left(\rho\left\|\partial_t e_u^{\text{reg}}(t)\right\|_{L^2(\Omega)}\left\|\partial_t \xi_u^h(t)\right\|_{L^2(\Omega)}\right. \\
& \qquad \left. + \frac{1}{2k}\left(\left(\frac{1}{T^2} + \frac{1}{T}\right)\left\|e_\lambda^{\text{reg}}(t)\right\|_{L^2(\Gamma)}^2 + T^2\left\|\partial_t^2 e_\lambda^{\text{reg}}(t)\right\|_{L^2(\Gamma)}^2 + Tk^2\left\|\partial_t \eta_u\right\|_{L^2(\Gamma)}^2\right)\right) dt \\
& \qquad + a\left(\xi_u^h(0), \xi_u^h(0)\right) && (133) \\
& \quad \leq 2\int_0^T \left(\rho\left\|\partial_t e_u^{\text{reg}}(t)\right\|_{L^2(\Omega)}\left\|\partial_t \xi_u^h(t)\right\|_{L^2(\Omega)}\right. \\
& \qquad \left. + \frac{1}{2k}\left(\left(\frac{1}{T^2} + \frac{1}{T}\right)\left\|e_\lambda^{\text{reg}}(t)\right\|_{L^2(\Gamma)}^2 + T^2\left\|\partial_t^2 e_\lambda^{\text{reg}}(t)\right\|_{L^2(\Gamma)}^2 + Tk^2\left\|\partial_t \eta_u\right\|_{L^2(\Gamma)}^2\right)\right) dt \\
& \qquad + a\left(\xi_u^h(0), \xi_u^h(0)\right) . && (134)
\end{aligned}$$

Recalling (129) and interpolation estimates bounding η_u, then using the $H^1(\Omega)$ coercivity of a, we have (to within a factor of $h^{-\epsilon}$) the desired $H^1(\Omega)$ stability of e_u^{reg}:

$$\|e_u^{\text{reg}}(s)\|_{H^1(\Omega)} \leq Ch^{-\epsilon} . \tag{135}$$

We now proceed with our duality argument, to sharpen (128) into a convergent error estimate. Consider the dual problem: Find $w \in L^2(0,T;H^1_0(\Omega))$ and $\omega \in L^2(0,T;H^{-1/2}(\Gamma))$ such that for all $\delta w \in H^1_0(\Omega)$ and $\delta\omega \in H^{-1/2}(\Gamma)$

$$\begin{aligned}\rho\,{}_{H^{-1}(\Omega)}\langle \partial_t w(t), \delta w\rangle_{H^1(\Omega)} - a\left(w(t), \delta w\right) + {}_{H^{-1/2}(\Gamma)}\langle \omega(t), \gamma\delta w\rangle_{H^{1/2}(\Gamma)} - {}_{H^{-1/2}(\Gamma)}\langle \delta\omega, \gamma w(t)\rangle_{H^{1/2}(\Gamma)} \\ = \left(e_u^{\mathrm{reg}}(t), \delta w\right)_{L^2(\Omega)} ,\end{aligned} \tag{136}$$

subject to the *final* condition that $w(T) = 0$. This problem should be viewed as evolving backwards through time; by examining the signs of the first two terms, it is clear that (136) is unstable in the forward time direction. Note that the trace of w is constrained to be zero on Γ, by the Lagrange multiplier ω. In view of the regularity of the source term, consider $\partial_t w(t) \in L^2(\Omega)$, so that the duality pairing can be re-written as an $L^2(\Omega)$ inner product. Inserting the test functions $\delta w = e_u^{\mathrm{reg}}(t)$ and $\delta\omega = e_\lambda^{\mathrm{reg}}(t)$, we get

$$\|e_u^{\mathrm{reg}}\|^2_{L^2(\Omega)} = \rho\left(\partial_t w, e_u^{\mathrm{reg}}\right)_{L^2(\Omega)} - a\left(w, e_u^{\mathrm{reg}}\right) + {}_{H^{-1/2}(\Gamma)}\left\langle \omega, \gamma e_u^{\mathrm{reg}}\right\rangle_{H^{1/2}(\Gamma)} - {}_{H^{-1/2}(\Gamma)}\left\langle e_\lambda^{\mathrm{reg}}, \gamma w\right\rangle_{H^{1/2}(\Gamma)} . \tag{137}$$

Adding and subtracting $\rho\left(w, \partial_t e_u^{\mathrm{reg}}\right)_{L^2(\Omega)}$ on the right and using the symmetry of a and the fact that $\gamma w = 0$ (in an appropriate weak sense),

$$\|e_u^{\mathrm{reg}}\|^2_{L^2(\Omega)} = \rho\partial_t\left(w, e_u^{\mathrm{reg}}\right)_{L^2(\Omega)} - \left(\rho\left(\partial_t e_u^{\mathrm{reg}}, w\right)_{L^2(\Omega)} + a\left(e_u^{\mathrm{reg}}, w\right)\right) + {}_{H^{-1/2}(\Gamma)}\left\langle \omega, \gamma e_u^{\mathrm{reg}}\right\rangle_{H^{1/2}(\Gamma)} . \tag{138}$$

Let w^h be a function in the discrete temperature space that satisfies the condition $\gamma w^h = 0$. A nontrivial finite element function in the discrete space satisfying this condition could be constructed, for instance, by assigning all nodes of elements intersecting Γ to zero, while allowing effective interpolation away from Γ. Due to the consistency of the semi-discrete problem with the regularized problem (85) we have

$$\|e_u^{\mathrm{reg}}\|^2_{L^2(\Omega)} = \rho\partial_t\left(w, e_u^{\mathrm{reg}}\right)_{L^2(\Omega)} - \left(\rho\left(\partial_t e_u^{\mathrm{reg}}, w - w^h\right)_{L^2(\Omega)} + a\left(e_u^{\mathrm{reg}}, w - w^h\right)\right) + {}_{H^{-1/2}(\Gamma)}\left\langle \omega, \gamma e_u^{\mathrm{reg}}\right\rangle_{H^{1/2}(\Gamma)} . \tag{139}$$

Suppose that Γ divides Ω into two portions, Ω_1 and Ω_2, and is sufficiently smooth that $w|_{\Omega_i} \in H^2(\Omega_i)$, $i = 1, 2$. Then we have

$$\left\| w|_{\Omega_i} \right\|_{L^2(0,T;H^2(\Omega_i))} \leq C\|e_u^{\mathrm{reg}}\|_{L^2(0,T;L^2(\Omega))} \tag{140}$$

and

$$\|\omega\|_{L^2(0,T;L^2(\Gamma))} \leq C\|e_u^{\mathrm{reg}}\|_{L^2(0,T;L^2(\Omega))} , \tag{141}$$

where we have abused notation slightly, in using the same symbol "ω" to denote both $\omega \in H^{-1/2}(\Gamma)$ and $\omega \in L^2(\Gamma)$ such that $(\omega, v)_{L^2(\Gamma)} = {}_{H^{-1/2}(\Gamma)} \langle \omega, v \rangle_{H^{1/2}(\Gamma)}$ for all $v \in H^{1/2}(\Gamma)$. The bounds (140) and (141) follow from regularity theory for the equivalent parabolic Dirichlet boundary value problem [126, Section 7.1.3] and boundedness of the normal derivative of $w|_{\Omega_i}$ [80, Theorem 7.53] (where the multiplier ω is the jump in normal derivative of w across Γ). Now assume that we can find an interpolant w^h of w, with $\gamma w^h = 0$, such that

$$\|w - w^h\|_{L^2(\Omega_i)} \leq Ch\|w\|_{H^2(\Omega_i)} \tag{142}$$

and

$$\|w - w^h\|_{H^1(\Omega_i)} \leq Ch^{1/2}\|w\|_{H^2(\Omega_i)} \ . \tag{143}$$

This can be shown for Q_1 finite elements by applying the results of [130] on either side of Γ. It basically forces w^h to be zero on the $O(h)$-thickness band of elements containing Γ, which introduces a first-order stair-step approximation of the boundary to each of Ω_1 and Ω_2. We speculate that the interpolation estimates (142) and (143) hold for many other finite element spaces as well. Because $\delta\lambda$ is quantified over all of $L^2(\Gamma)$, we have that

$${}_{H^{-1/2}(\Gamma)} \left\langle \omega, \gamma e_u^{\text{reg}} \right\rangle_{H^{1/2}(\Gamma)} = \left(\omega, \gamma e_u^{\text{reg}}\right)_{L^2(\Gamma)} = \left(\omega, \frac{1}{k}\partial_t e_\lambda^{\text{reg}}\right)_{L^2(\Gamma)} \ . \tag{144}$$

Applying Cauchy–Schwarz to (144),

$$\left|\left(\omega, \gamma e_u^{\text{reg}}\right)_{L^2(\Gamma)}\right| \leq \frac{\|\omega\|_{L^2(\Gamma)}}{\sqrt{k}} \sqrt{\frac{1}{k} \left\|\partial_t e_\lambda^{\text{reg}}\right\|_{L^2(\Gamma)}^2} \leq \frac{C\sqrt{kh^{2-\epsilon}}}{\sqrt{k}}\|\omega\|_{L^2(\Gamma)} \leq Ch^{1-\epsilon}\|\omega\|_{L^2(\Gamma)} \ , \tag{145}$$

where the value of ϵ has been allowed to absorb a positive constant. Cauchy–Schwarz, (129), and (142) give us

$$\rho\left|\left(\partial_t e_u^{\text{reg}}, w - w^h\right)_{L^2(\Omega)}\right| \leq Ch\sqrt{kh^{2-\epsilon}}\|w\|_{H^2(\Omega\setminus\Gamma)} \leq C\sqrt{k}h^{2-\epsilon}\|w\|_{H^2(\Omega\setminus\Gamma)} \ , \tag{146}$$

where the value of ϵ has again been allowed to shift by a constant factor and $H^2(\Omega \setminus \Gamma)$ indicates that the space is broken across Γ. $H^1(\Omega)$ boundedness of a, $H^1(\Omega)$ stability (135) of e_u^{reg}, and the interpolation estimate (143) provide

$$\left|a\left(e_u^{\text{reg}}, w - w^h\right)\right| \leq Ch^{1/2-\epsilon}\|w\|_{H^2(\Omega\setminus\Gamma)} \ . \tag{147}$$

Thus, using the preceding bounds in (139),

$$\|e_u^{\text{reg}}\|^2_{L^2(\Omega)} \leq \rho\partial_t \left(w, e_u^{\text{reg}}\right)_{L^2(\Omega)} + \left(C_1 \sqrt{k}h^{2-\epsilon} + C_2 h^{1/2-\epsilon}\right)\|w\|_{H^2(\Omega\setminus\Gamma)} + C_3 h^{1-\epsilon}\|\omega\|_{L^2(\Gamma)} \ , \tag{148}$$

where C_1, C_2, and C_3 are independent of h and k, but may carry different units in a physical problem. The preasymptotic convergence regimes associated with these constants are therefore connected to the physics of the system being modeled. The practical implications of these preasymptotic regimes for specific problem classes are, however, beyond the scope of the present analysis. Integrating in time, assuming $e_u^{\text{reg}}(0) = 0$, using the final condition on $w(T)$, and recalling the bounds on the solution to the dual problem,

$$\|e_u^{\text{reg}}\|^2_{L^2(0,T;L^2(\Omega))} \leq C\left(C_1 \sqrt{k}h^{2-\epsilon} + C_2 h^{1/2-\epsilon} + C_3 h^{1-\epsilon}\right)\|e_u^{\text{reg}}\|_{L^2(0,T;L^2(\Omega))} \ . \tag{149}$$

For $k \sim 1/h^2$, (149) implies, for h sufficiently small, that

$$\|e_u^{\text{reg}}\|_{L^2(0,T;L^2(\Omega))} \leq C h^{1/2-\epsilon} \ . \tag{150}$$

3.1.7. Discretization in time

Consider the following problem template: Find x such that, for all y in an appropriate test space,

$$(\dot{x}(t), y) = -B(x(t), y) + F(y) \ , \tag{151}$$

where $(\cdot,\cdot)$ is an inner product, B is a bilinear form and F is a bounded linear functional. In the case of the semi-discrete regularized problem (115), $x(t)$ and y are in the Cartesian product space of temperatures and multipliers:

$$x = \left\{u^h, \lambda^h\right\} \tag{152}$$

and

$$y = \left\{v^h, \delta\lambda\right\} \ , \tag{153}$$

and the inner product, bilinear, and linear forms are defined by

$$(\dot{x}, y) = \frac{\rho}{2}\left(\partial_t u^h, v^h\right)_{L^2(\Omega)} + \frac{\Delta t}{2(1+r)\beta}\left(\partial_t \lambda^h, \delta\lambda\right)_{L^2(\Gamma)} \ , \tag{154}$$

$$2B(x,y) = a\left(u^h, v^h\right) + \left(\lambda^h, v^h\right)_{L^2(\Gamma)} - \left(\delta\lambda, u^h\right)_{L^2(\Gamma)} + \frac{r}{(1+r)\beta}\left(\lambda^h, \delta\lambda\right)_{L^2(\Gamma)} \ , \tag{155}$$

and

$$2F(y) = (f(t), v^h)_{L^2(\Omega)} - (g(t), \delta\lambda)_{L^2(\Gamma)} \ . \tag{156}$$

Note that $B(y, y) \geq 0$ for all y in the test/trial space. Note also that the norm induced by the inner product $(\cdot, \cdot)$ is exactly $|||\cdot|||$ (defined earlier by (89)). We now test the local truncation error (LTE) that results from inserting the semi-discrete solution into the backward Euler time discretization:

$$((\mathrm{LTE})_{n+1}, y) = \left(\frac{x(t^{n+1}) - x(t^n)}{\Delta t}, y\right) + B(x(t^{n+1}), y) - F(y) \tag{157}$$

$$= \left(\frac{x(t^{n+1}) - \left(x(t^{n+1}) - \Delta t \dot{x}(t^{n+1}) - R_1(t^n)\right)}{\Delta t}, y\right) + B(x(t^{n+1}), y) - F(y) \tag{158}$$

$$= \left(\frac{R_1(t^n)}{\Delta t}, y\right) , \tag{159}$$

where $R_1(t^n)$ in the above is the remainder of a Taylor series expansion of x about t^{n+1}, evaluated at t^n. Thus the LTE is bounded like

$$|||(\mathrm{LTE})_{n+1}||| = \frac{|||R_1(t^n)|||}{\Delta t} \tag{160}$$

$$\leq \sup_{\xi \in (t^n, t^{n+1})} \frac{\frac{1}{2}|||\ddot{x}(\xi)|||\Delta t^2}{\Delta t} \tag{161}$$

$$\leq \sup_{\xi \in (0, T)} \frac{\frac{1}{2}|||\ddot{x}(\xi)|||\Delta t^2}{\Delta t} \tag{162}$$

$$\leq C \Delta t \, , \tag{163}$$

where C is independent of n, Δt and β. The last inequality follows from the uniform stability of (time derivatives of) the semi-discrete regularized problem in the $|||\cdot|||$ norm. (Recall that the uniformity of the $|||\cdot|||$-norm stability relies, in the preceding analysis, on assumptions that sufficiently many derivatives of the problem data are zero at $t = 0$. Numerical results in the sequel suggest, however, that these assumptions are unnecessary; a route toward weakening the conditions on data at $t = 0$ is suggested in Remark 6.) Testing the error e^{n+1} between the backward Euler solution x^{n+1} and the semi-discrete solution $x(t^{n+1})$,

$$\left(e^{n+1}, y\right) = \left(x^{n+1} - x(t^{n+1}), y\right) \tag{164}$$

$$= (e^n, y) - \Delta t \left(B(e^{n+1}, y) + ((\mathrm{LTE})_{n+1}, y)\right) \, . \tag{165}$$

Inserting test function $y = e^{n+1}$, using the Cauchy–Schwarz inequality (with the norm induced by the inner product $(\cdot, \cdot)$), and using the coercivity of B,

$$\left|\left|\left|e^{n+1}\right|\right|\right|^2 = \left(e^n, e^{n+1}\right) - \Delta t \left(B(e^{n+1}, e^{n+1}) + \left((\mathrm{LTE})_{n+1}, e^{n+1}\right)\right) \tag{166}$$

$$\leq \left|\left|\left|e^{n+1}\right|\right|\right| \cdot |||e^n||| + \Delta t |||(\mathrm{LTE})_{n+1}||| \cdot \left|\left|\left|e^{n+1}\right|\right|\right| \tag{167}$$

$$\Rightarrow \left|\!\left|\!\left| e^{n+1} \right|\!\right|\!\right| \leq |\!|\!| e^n |\!|\!| + \Delta t |\!|\!| (\mathrm{LTE})_{n+1} |\!|\!| \ . \tag{168}$$

Using the bound (163) on LTE, (168) becomes

$$\left|\!\left|\!\left| e^{n+1} \right|\!\right|\!\right| \leq |\!|\!| e^n |\!|\!| + C\Delta t^2 \ , \tag{169}$$

where C is independent of Δt and β. Assuming for simplicity that $e^0 = 0$,

$$\left|\!\left|\!\left| e^{1} \right|\!\right|\!\right| \leq C'\Delta t^2 \tag{170}$$
$$\left|\!\left|\!\left| e^{2} \right|\!\right|\!\right| \leq \left(\left|\!\left|\!\left| e^{1} \right|\!\right|\!\right| + C'\Delta t^2 \right) \leq 2C'\Delta t^2 \tag{171}$$
$$\left|\!\left|\!\left| e^{3} \right|\!\right|\!\right| \leq \left(\left|\!\left|\!\left| e^{2} \right|\!\right|\!\right| + C'\Delta t^2 \right) \leq 3C'\Delta t^2 \tag{172}$$
$$\dots$$
$$\left|\!\left|\!\left| e^{N} \right|\!\right|\!\right| \leq \left(\left|\!\left|\!\left| e^{N-1} \right|\!\right|\!\right| + C'\Delta t^2 \right) \leq NC'\Delta t^2 \ , \tag{173}$$

where $N = T/\Delta t$ and the prime on C' is merely to prevent it from absorbing numerical constants as is typically allowed with the symbol "C". Taking T to be constant, then

$$\left|\!\left|\!\left| e^{N} \right|\!\right|\!\right| \leq \frac{T}{\Delta t} C'\Delta t^2 \leq C\Delta t \ , \tag{174}$$

where C does not depend on Δt or β. This implies first-order temporal convergence in the norm $|\!|\!| \cdot |\!|\!|$, which controls the temperature in $L^2(\Omega)$.

3.1.8. Numerical experiment: scalar parabolic problem

In this section, we construct an instance of the parabolic model problem and test the convergence of the discretization. In this problem instance, the space dimension, d, is two, $a(u, v) = (\nabla u, \nabla v)_{L^2(\Omega)}$, and $\rho = 1$. The prescribed functions f and g are zero. Ω is the square $(-W/2, W/2)^2 \subset \mathbb{R}^2$, with $W = 2.5$ and Γ is the unit circle $\{\mathbf{x} \in \mathbb{R}^2 \ : \ \|\mathbf{x}\|_{\ell^2} = 1\}$. The time interval terminates at time $t = T = 0.1$ and the initial temperature at $t = 0$ is

$$u_0(r, \theta) = \begin{cases} J_0(Rr) & r < 1 \\ 0 & \text{otherwise} \end{cases} \ , \tag{175}$$

where r and θ are standard 2D polar coordinates and R is the first root of the Bessel function J_0. This implies that the exact solution is

$$u(r, \theta, t) = J_0(Rr)e^{-R^2 t} \ . \tag{176}$$

For discretization, we use a linear uniform B-spline space with $2^N \times 2^N$ elements, for $N \in \{3, \ldots, 10\}$, to represent trial and test functions. We define the penalty by $\beta = C_{\text{pen}}/h$, where $h = W/2^N$ is element width of the uniform B-spline space and $C_{\text{pen}} = 1$. The discrete initial condition is set by nodal interpolaton of u_0. The time step is proportional to h, viz. $\Delta t = T/2^N$. An illustrative snapshot of a numerical solution is shown in Figure 2.

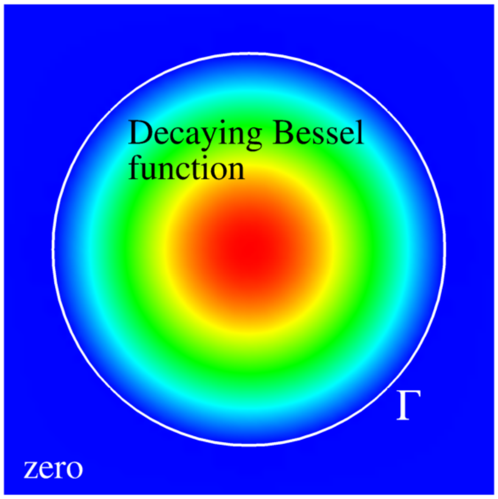

Figure 2: Annotated snapshot of a solution to the scalar parbolic test problem.

To test the robustness of the formulation for small perturbation parameters $r \ll 1$, we first compute with $r = 0.1$ and then compare with results for $r = 0$. Figure 3 shows the convergence of $L^2(\Omega)$ and $H^1(\Omega)$ norms of the error $u - u^h$ at time T for $r = 0.1$ and $r = 0$, suggesting convergence rates of 1/2 in $H^1(\Omega)$ and 1 in $L^2(\Omega)$ for both cases.

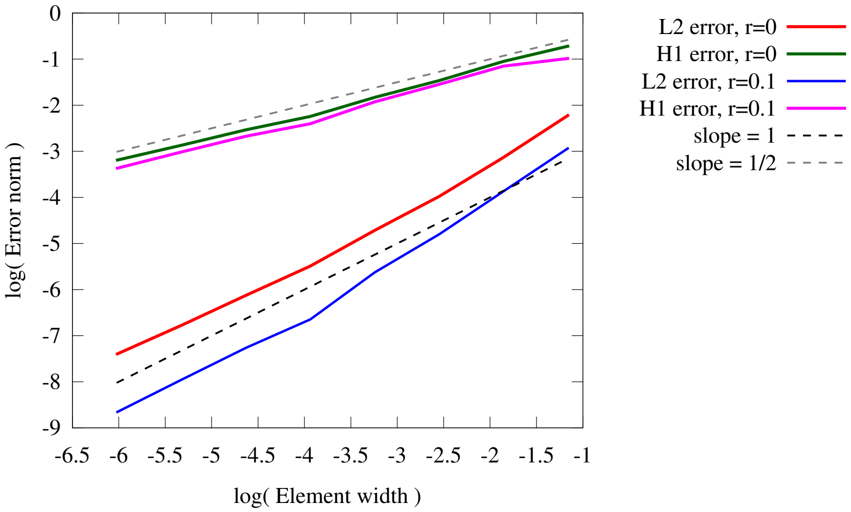

Figure 3: Convergence of L^2 and H^1 errors for different values of r.

Integrals over Γ are evaluated using 32×2^N quadrature points, spaced evenly along the arc length of Γ, where 2^N is the number of elements across the width of the domain. A scalar sample of λ is stored and updated at each of these points. This high density of points rules out the possibility of accidental inf-sup stability following from reduced quadrature of the boundary constraint. Consistent with the absence of any proven convergence for λ^h, the computed multiplier field is highly oscillatory and bears no resemblance whatsoever to the spatially-uniform exact solution. Figure 4 shows a representative plot of the multiplier as a function of polar angle around Γ. In light of such inaccurate results for the multiplier field, we would recommend to consider the Lagrange multiplier a by-product of constraint enforcement rather than a meaningful component of the solution. This is consistent with the results obtained by Kallemov et al. [131, Figure 8] who solved implicitly for Lagrange multipliers at boundary points immersed in Stokes flow. The cited study found that, for high spatial densities of markers, the multiplier "traction" is highly oscillatory. (While rarely reported or visualized, such boundary force oscillations are presumably present in many immersed boundary computations, since, as pointed out by [131], high densities of markers are frequently recommended to prevent leakage.) Also in agreement with [131], we observe that low-order moments of the Lagrange multiplier field (e.g. net drag or torque on immersed objects) remain accurate in spite of egregious spatial oscillations.

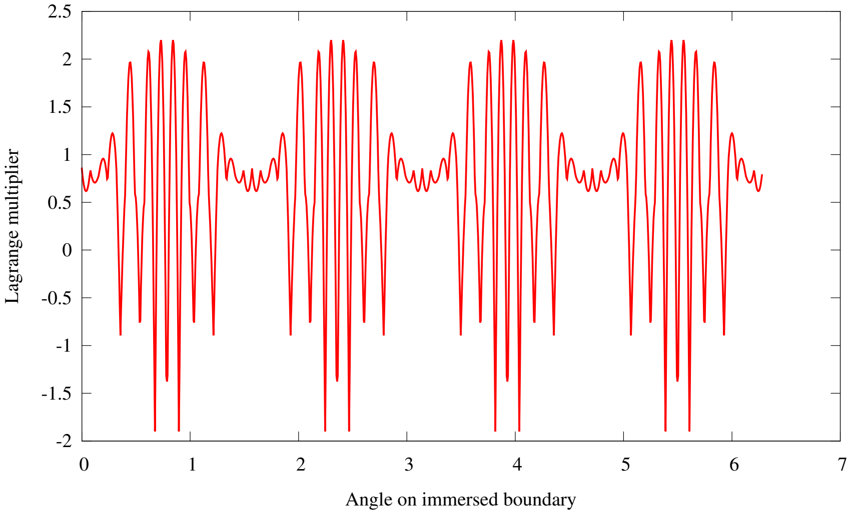

Figure 4: The value of λ^h as a function of the angle around Γ. (Linear interpolation is used between surface quadrature point samples of λ^h.)

Remark 9. The error norms used to assess convergence are integrated over Ω with the same 2×2 quadrature rule used to assemble the equation systems in the analysis. Due to the low regularity of the exact solution, this incurs a significant integration error, but this extra error is not asymptotically worse than what one would expect from approximation and temporal truncation considerations.

3.2. *Extension to related linear problems*

The analysis of the scalar second-order parabolic equation suggests some extensions to other linear model problems that more closely resemble FSI. This section will address some of those extensions, albeit with a lesser degree of rigor and completeness than the analysis of the scalar parabolic problem.

3.2.1. *Unsteady Stokes flow*

The analysis of the heat equation can be formally extrapolated to divergence-conforming discretizations of unsteady Stokes flow, by posing the problem over the solenoidal subspace of $V_0(\Omega) \subset \left(H^1(\Omega)\right)^d$ and seeking discrete solutions in a finite dimensional subspace (cf. [132, Section 10]). This is in contrast to non-div-conforming discretizations, in which the subspace of discrete velocities that weakly satisfy incompressibility with respect to a finite dimensional pressure test space are not pointwise divergence-free and do not form a proper subset of solenoidal H^1 functions. To simplify discussion, we will eliminate the tangential portion of the multiplier on Γ from the outset, with the understanding that this approaches consistency with the true no-slip-on-Γ Stokes problem as the penalty coefficient $\tau_{\text{TAN}} \to \infty$.

More precisely, consider the problem: Find velocity $\mathbf{u} \in L^2(0,T;V_0(\Omega))$ with $\partial_t\mathbf{u} \in L^2(0,T;V_0^*(\Omega))$ and normal traction jump $\lambda \in L^2(0,T;H^{-1/2}(\Gamma))$ such that for every $\mathbf{v} \in V_0(\Omega)$ and $\delta\lambda \in H^{-1/2}(\Gamma)$ at a.e. $t \in [0,T]$,

$$\begin{aligned} &\rho_{V_0^*(\Omega)}\langle \partial_t\mathbf{u}(t),\mathbf{v}\rangle_{V_0(\Omega)} + a(\mathbf{u}(t),\mathbf{v}) + {}_{H^{-1/2}(\Gamma)}\langle \lambda(t), \mathbf{v}\cdot\mathbf{n}\rangle_{H^{1/2}(\Gamma)} - {}_{H^{-1/2}(\Gamma)}\langle \delta\lambda, \mathbf{u}(t)\cdot\mathbf{n}\rangle_{H^{1/2}(\Gamma)} \\ &\qquad + \tau_{\text{TAN}}\left(\mathbf{u}(t) - (\mathbf{u}(t)\cdot\mathbf{n})\mathbf{n}, \mathbf{v}\right)_{L^2(\Gamma)} \\ &\quad = {}_{H^{-1/2}(\Gamma)}\langle \delta\lambda, \mathbf{g}(t)\cdot\mathbf{n}\rangle_{H^{1/2}(\Gamma)} + \tau_{\text{TAN}}\left(\mathbf{g}(t) - (\mathbf{g}(t)\cdot\mathbf{n})\mathbf{n}, \mathbf{v}\right)_{L^2(\Gamma)} + {}_{V_0^*(\Omega)}\langle \mathbf{f}(t),\mathbf{v}\rangle_{V_0(\Omega)} \end{aligned} \tag{177}$$

and

$$\mathbf{u}(0) = \mathbf{u}_0 \in L^2(\Omega)\ , \tag{178}$$

where $\mathbf{n}$ is a normal vector to the surface Γ, $\mathbf{g}(t)$ is the prescribed velocity on Γ at time t, $\mathbf{f}(t)$ is some functional in the dual of $V_0(\Omega)$, ρ takes on the physical interpretation of mass density, and the bilinear form a is now defined

$$a(\mathbf{u},\mathbf{v}) = 2\mu\left(\boldsymbol{\varepsilon}(\mathbf{u}),\boldsymbol{\varepsilon}(\mathbf{v})\right)_{L^2(\Omega)}\ , \tag{179}$$

where μ is the dynamic viscosity and $\boldsymbol{\varepsilon}$ is the symmetric gradient operator. This problem statement is subtly incomplete in that, depending on the geometry of Γ, there may be some compatibility condition on the data $\mathbf{g}$ to ensure consistency with mass conservation (e.g., if Γ encloses a region of Ω, the integral of the normal component of $\mathbf{g}$ must be zero to have a solenoidal $\mathbf{u} \in V_0$ satisfying the immersed boundary condition). The steps of the semi-implicit time integration scheme become

1. Given $\mathbf{u}^n$ and λ^n, find $\mathbf{u}^{n+1}$ such that for all $\mathbf{v}$,

$$\begin{aligned}\rho\left(\mathbf{u}_t^{n+1},\mathbf{v}\right)_{L^2(\Omega)} &+ a(\mathbf{u}^{n+1},\mathbf{v}) + (\lambda^n,\mathbf{v}\cdot\mathbf{n})_{L^2(\Gamma)}\\ &+ \tau_{\mathrm{NOR}}\left(\mathbf{u}^{n+1}\cdot\mathbf{n},\mathbf{v}\cdot\mathbf{n}\right)_{L^2(\Gamma)} + \tau_{\mathrm{TAN}}\left(\mathbf{u}^{n+1}-(\mathbf{u}^{n+1}\cdot\mathbf{n})\mathbf{n},\mathbf{v}\right)_{L^2(\Gamma)}\\ &= \tau_{\mathrm{NOR}}\left(\mathbf{g}(t^{n+1})\cdot\mathbf{n},\mathbf{v}\cdot\mathbf{n}\right)_{L^2(\Gamma)} + \tau_{\mathrm{TAN}}\left(\mathbf{g}(t^{n+1})-(\mathbf{g}(t^{n+1})\cdot\mathbf{n})\mathbf{n},\mathbf{v}\right)_{L^2(\Gamma)}\\ &+ {}_{V_0^*(\Omega)}\langle\mathbf{f}(t^{n+1}),\mathbf{v}\rangle_{V_0(\Omega)}\ ,\end{aligned}\tag{180}$$

   where

$$\mathbf{u}_t^{n+1} = \frac{\mathbf{u}^{n+1}-\mathbf{u}^n}{\Delta t}\ .\tag{181}$$

2. Update the multiplier such that, for all $\delta\lambda\in L^2(\Gamma)$,

$$(\lambda^{n+1},\delta\lambda)_{L^2(\Gamma)} = \frac{1}{1+r}\left(\lambda^n+\tau_{\mathrm{NOR}}(\mathbf{u}^{n+1}-\mathbf{g}(t^{n+1}))\cdot\mathbf{n},\delta\lambda\right)_{L^2(\Gamma)}\ .$$

The corresponding implicitly-integrated regularized problem is: Find the regularized velocity $\mathbf{u}^{\mathrm{reg}}\in L^2(0,T;V_0(\Omega))$ with $\partial_t\mathbf{u}^{\mathrm{reg}}\in L^2(0,T;V_0^*(\Omega))$ and normal traction jump $\lambda^{\mathrm{reg}}\in L^2(0,T;L^2(\Gamma))$ with $\partial_t\lambda^{\mathrm{reg}}\in L^2(0,T;L^2(\Gamma))$ such that for every $\mathbf{v}\in V_0(\Omega)$ and $\delta\lambda\in L^2(\Gamma)$ at a.e. $t\in[0,T]$,

$$\begin{aligned}\rho\,{}_{V_0^*(\Omega)}\langle\partial_t\mathbf{u}^{\mathrm{reg}}(t),\mathbf{v}\rangle_{V_0(\Omega)} &+ a(\mathbf{u}^{\mathrm{reg}}(t),\mathbf{v}) + (\lambda^{\mathrm{reg}}(t),\mathbf{v}\cdot\mathbf{n})_{L^2(\Gamma)}\\ &+\left(\frac{\Delta t}{(1+r)\tau_{\mathrm{NOR}}}\partial_t\lambda^{\mathrm{reg}}(t)-\mathbf{u}^{\mathrm{reg}}(t)\cdot\mathbf{n}+\frac{r}{(1+r)\tau_{\mathrm{NOR}}}\lambda^{\mathrm{reg}}(t),\delta\lambda\right)_{L^2(\Gamma)}\\ &+\tau_{\mathrm{TAN}}\left(\mathbf{u}^{\mathrm{reg}}(t)-(\mathbf{u}^{\mathrm{reg}}(t)\cdot\mathbf{n})\mathbf{n},\mathbf{v}\right)_{L^2(\Gamma)}\\ &= (\mathbf{g}(t)\cdot\mathbf{n},\delta\lambda)_{L^2(\Gamma)} + \tau_{\mathrm{TAN}}\left(\mathbf{g}(t)-(\mathbf{g}(t)\cdot\mathbf{n})\mathbf{n},\mathbf{v}\right)_{L^2(\Gamma)} + {}_{V_0^*(\Omega)}\langle\mathbf{f}(t),\mathbf{v}\rangle_{V_0(\Omega)}\end{aligned}\tag{182}$$

and

$$\mathbf{u}^{\mathrm{reg}}(0)=\mathbf{u}_0\in L^2(\Omega)\ ,\quad \lambda^{\mathrm{reg}}(0)=\lambda_0\in L^2(\Gamma)\ .\tag{183}$$

Notice that the compatibility condition on $\mathbf{g}$ is no longer strictly required in the regularized problem, although we would anticipate bad results if it is violated. Recognizing the coercivity of the tangential penalty term and the formal similarity of this problem to the scalar parabolic problem of Section 3.1, we do not expect to encounter major difficulties adapting the program of Section 3.1 to this setting, to bound errors at time T in the norm

$$|||\mathbf{u},\lambda|||^2 = \frac{1}{2}\rho\,\|\mathbf{u}\|^2_{L^2(\Omega)} + \frac{\Delta t}{2(1+r)\tau_{\mathrm{NOR}}}\,\|\lambda\|^2_{L^2(\Gamma)}\ .\tag{184}$$

The first term now carries the physical interpretation of the kinetic energy of the fluid. In the case of $r = 0$, the multiplier represents a normal displacement of fluid through Γ, and the second term of the energy norm becomes a spring-like potential energy (foreshadowing the inclusion of a structural potential energy in linearized FSI problems).

3.2.2. Numerical experiment: linearized Taylor–Green vortex

The following velocity field is a solution to the 2D Navier–Stokes equations posed on the domain $\Omega = [-\pi, \pi]^2$ with periodic boundary conditions and no external forcing:

$$\mathbf{u}_{\mathrm{TG}}(\mathbf{x}, t) = (\sin(x_1)\cos(x_2)\mathbf{e}_1 - \cos(x_1)\sin(x_2)\mathbf{e}_2)\, e^{-2\mu t/\rho} \, . \tag{185}$$

This is known as the Taylor–Green vortex. The velocity field is also an exact solution to the Stokes equations, with the body force field $\mathbf{f}_{\mathrm{TG}} = -\rho \mathbf{u}_{\mathrm{TG}} \cdot \nabla \mathbf{u}_{\mathrm{TG}}$. We may construct an interesting test problem by prescribing $\mathbf{u} = \mathbf{u}_{\mathrm{TG}}$ as an initial condition at $t = 0$ and also as a time-dependent Dirichlet boundary condition on a closed immersed boundary Γ, then adding a spatially-uniform body force $\mathbf{f}_x = \mathbf{e}_1$ in the x_1-direction, so that the total body force is $\mathbf{f} = \mathbf{f}_{\mathrm{TG}} + \mathbf{f}_x$. This body force induces a pressure gradient in the region enclosed by Γ without perturbing the velocity solution in that region. The velocity outside of the region enclosed by Γ is no longer equal to $\mathbf{u}_{\mathrm{TG}}$ for $t > 0$. There are jumps in the pressure and velocity derivatives along Γ. The regularity of the velocity solution is therefore representative of typical usage of an immersed boundary method.

We have not attempted to derive an exact solution on the entire domain, but we can easily measure the error in the subset Ω^{err}, enclosed by Γ. Let Γ be a circle centered at $(x, y) = (0, 0)$, with radius 2 and let $\Omega^{\mathrm{err}} = \{\mathbf{x} \in \mathbb{R}^2 \mid |\mathbf{x}|_{\ell^2} < 2\}$. We integrate errors on Ω^{err} approximately, using points from a 3×3 Gaussian quadrature rule on each element that fall inside of Ω^{err}. This is only a first order approximation, but we do not expect higher than first order convergence of errors in any norm. The setup is illustrated, along with a representative numerical solution, in Figure 5.

We discretize this problem using $2^N \times 2^N$ div-conforming B-spline elements of degree $k' = 1$, for $N \in \{4, \dots, 9\}$. Due to the low regularity of the exact solution, we would not expect to obtain improved convergence rates with higher k'. The problem is posed over the interval $(0, T)$ with $T = 0.2$, using time steps of size $\Delta t = T/(2^{N-2})$. The initial condition is set using H^1 projection. Penalty values are $\tau_{\mathrm{NOR}} = \tau_{\mathrm{TAN}} = 100\mu/h$, where $h = 2\pi/(2^N)$ is the mesh element size. The convergence of $L^2(\Omega^{\mathrm{err}})$ and $H^1(\Omega^{\mathrm{err}})$ errors at time T is shown in Figure 6. As with the heat equation, the convergence for $r > 0$ is first order in $L^2(\Omega^{\mathrm{err}})$ and one-half order in $H^1(\Omega^{\mathrm{err}})$, with robustness in the limit of $r \to 0$.

3.2.3. Coupled second-order problems

To look at coupling between d-dimensional and $(d-1)$-dimensional subproblems without immediately facing the complexities of fluid–structure interaction, we outline a model problem

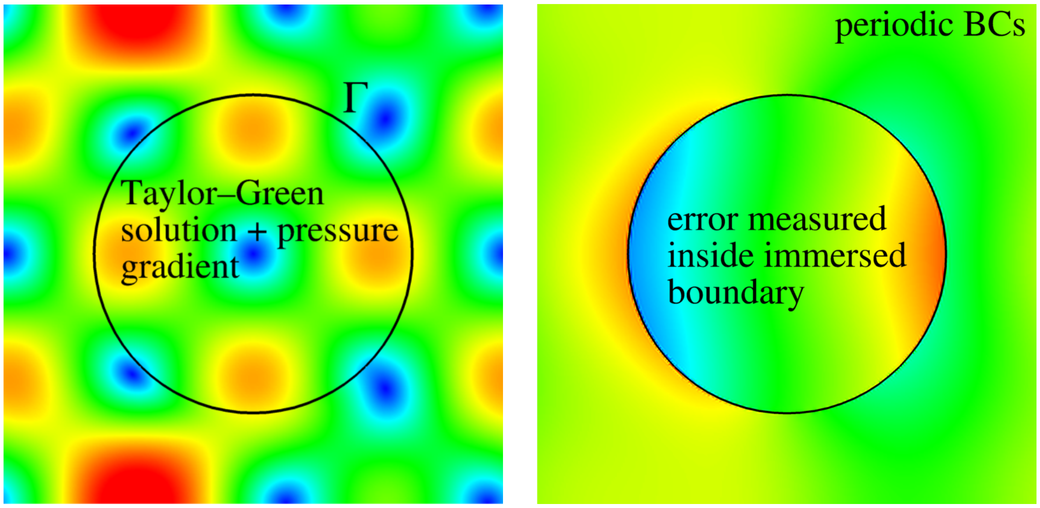

Figure 5: Simultaneous velocity magnitude (left) and pressure (right) snapshots of the Stokes Taylor–Green problem, with annotations describing the problem setup.

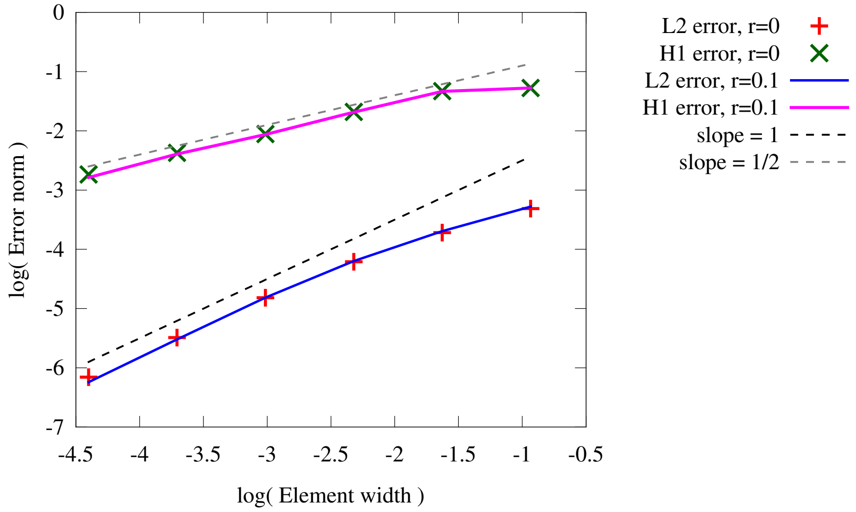

Figure 6: Convergence of $L^2(\Omega^{\text{err}})$ and $H^1(\Omega^{\text{err}})$ errors at time T for different values of r.

in which two second-order parabolic subproblems are coupled: Find $u \in L^2(0,T;H_0^1(\Omega))$ with $\partial_t u \in L^2(0,T;H^{-1}(\Omega))$, $y \in L^2(0,T;H_0^1(\Gamma))$ with $\partial_t y \in L^2(0,T;H^{-1}(\Gamma))$ and $\lambda \in L^2(0,T;H^{-1/2}(\Gamma))$ such that for every $v \in H_0^1(\Omega)$, $z \in H_0^1(\Gamma)$ and $\delta\lambda \in H^{-1/2}(\Gamma)$ at a.e. $t \in [0,T]$,

$$\begin{aligned}\rho_1 \; {}_{H^{-1}(\Omega)}\langle \partial_t u(t), v\rangle_{H^1(\Omega)} + a_1(u(t),v) + \rho_2 \; {}_{H^{-1}(\Gamma)}\langle \partial_t y(t), z\rangle_{H^1(\Gamma)} + a_2(y(t),z)\\ + \; {}_{H^{-1/2}(\Gamma)}\langle \lambda(t), \gamma w - z\rangle_{H^{1/2}(\Gamma)} - \; {}_{H^{-1/2}(\Gamma)}\langle \delta\lambda, \gamma u(t) - y(t)\rangle_{H^{1/2}(\Gamma)} = F(v,z)\end{aligned} \tag{186}$$

and

$$u(0) = u_0 \in L^2(\Omega)\,, \quad y(0) = y_0 \in L^2(\Gamma)\,. \tag{187}$$

a_1 is coercive over $H^1_0(\Omega)$ and a_2 is coercive over $H^1_0(\Gamma)$. Following the pattern set by the scalar parabolic problem of Section 3.1 and the unsteady Stokes problem of Section 3.2.1, it should be clear what the semi-implicit algorithm and equivalent implicitly-integrated problem are for the coupled problem. Much of the program of Section 3.1 can then be repeated nearly unchanged to obtain analogous error estimates in the norm

$$|||u, y, \lambda|||^2 = \frac{1}{2}\rho_1 \, \|u\|^2_{L^2(\Omega)} + \frac{1}{2}\rho_2 \|y\|^2_{L^2(\Gamma)} + \frac{\Delta t}{2(1+r)\beta} \, \|\lambda\|^2_{L^2(\Gamma)} \; . \tag{188}$$

We use this model coupled problem to demonstrate the efficacy of block iteration in Section 4.

3.3. *Extrapolation to Navier–Stokes flow*

A priori error analysis for Navier–Stokes flow with immersed boundaries is beyond the scope of this paper, but, to demonstrate the robustness of the estimates derived for linear model problems, we study convergence for Navier–Stokes flow empirically, using numerical experiments.

3.3.1. *Taylor–Green vortex*

This section considers a variant of the numerical experiment from Section 3.2.2, but with the full Navier–Stokes equations. Recall that Section 3.2.2 solved the Stokes equations, with the advection term of the Taylor–Green vortex solution (185) prescribed as a body force. We now treat the advection term nonlinearly. As in Section 3.2.2, div-conforming B-splines of degree $k' = 1$ are used to discretize the velocity and pressure spaces and backward Euler integration is applied in time. In this section, we consider the case of low Reynolds number flow, and choose $\mu = 0.01$. (A high Reynolds-number stress test is carried out in Section 3.3.3.)

An interesting phenomenon that we have noticed in nonlinear computations is that prescribing an immersed boundary velocity that differs from the actual movement of Γ_t leads to severely degraded performance and, at high Reynolds numbers and/or over long time intervals, an apparent lack of convergence. For this reason, we use the boundary of the square $[-\pi, \pi]$ for Γ_t. No fluid flows across this boundary in (185). To avoid any special behavior associated mesh-aligned immersed boundaries, we distort the background mesh in a periodic manner, shown in Figure 7. In the notation of Section 2.2.2, this corresponds to a deformation of

$$\boldsymbol{\phi}(\mathbf{X}) = \left(X_1 + A \sin\left(\frac{\pi X_1}{W/2}\right) \sin\left(\frac{\pi X_2}{W/2}\right), X_2 + A \sin\left(\frac{\pi X_1}{W/2}\right) \sin\left(\frac{\pi X_2}{W/2}\right)\right) \tag{189}$$

applied to the parametric domain $\widehat{\Omega} = (-W/2, W/2)^2 \subset \mathbb{R}^2$, with $A = 1$ and $W = 4\pi$. To test convergence, we divide the parametric domain $\widehat{\Omega}$ evenly into $2^N \times 2^N$ elements, for $N \in \{4, 5, 6, 7, 8\}$. The time interval $(0, T = 0.7)$ is divided into steps of size $\Delta t = T/2^{N-3}$. Penalty parameters are defined by (52) and (53), with h defined to be $W/2^N$ (regardless of mesh distortion), $C^{\text{inert}}_{\text{NOR}} = C^{\text{inert}}_{\text{NOR}} = 1000$,

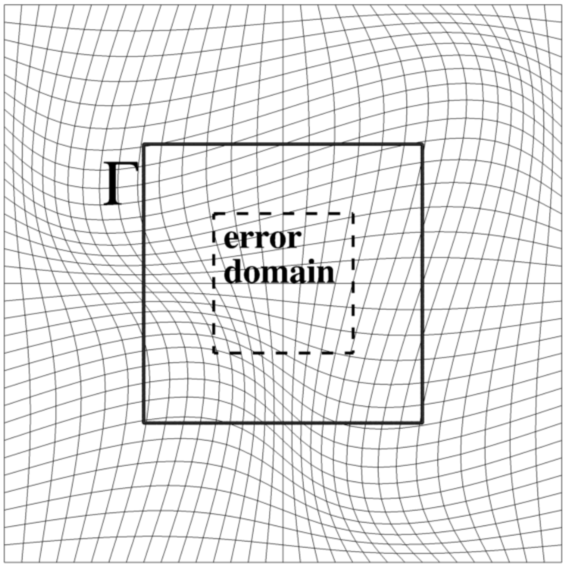

Figure 7: The non-rectilinear mesh of Ω avoids grid alignment with Γ.

and $C_{\text{TAN}} = 100$. The initial condition is set by $H^1(\Omega)$ projection onto the divergence-free discrete subspace. As in Section 3.2.2, we measure error on a subset Ω^{err} of the domain. For Navier–Stokes flow, we are interested in looking at the advection-dominated limit, in which the H^1 norm of the exact velocity solution diverges near the boundary (due to a discontinuous velocity field, which is $\notin H^1(\Omega)$), so we define the error domain to have an $O(1)$ separation from Γ_t, as shown in Figure 7. We choose $\Omega^{\text{err}} = [-W/8, W/8]$. Due to the mesh distortion, Ω^{err} is no longer a union of elements. We integrate errors on Ω^{err} inexactly, by using whatever analysis quadrature points happen to fall in Ω^{err}. While this is a crude, first-order quadrature scheme, we do not expect it to influence asymptotic convergence rates, based on our *a priori* analysis and experience with the simpler linear problems, for which at most first-order convergence is found, regardless of norm.

An annotated snapshot of a solution illustrates the problem setup in Figure 8. The convergence of errors on Ω^{err} is shown in Figure 9. The nearly first-order convergence rates obtained suggest that the analysis of linear parabolic problems extrapolates reasonably well to Navier–Stokes flow.

3.3.2. Translating Taylor–Green vortex

The addition of a uniform velocity to an initial condition in a periodic domain yields a Galilean transformation of the original solution. In this section, we superpose velocity $\mathbf{v} = -0.87\mathbf{e}_1 - 0.5\mathbf{e}_2$ on top of the initial condition of the problem from Section 3.3.1 and translate the boundary Γ_t at the same velocity. A snapshot of the solution at time T is shown in Figure 10. Figure 11 illustrates how the near-first-order convergence on Ω^{err} remains intact.

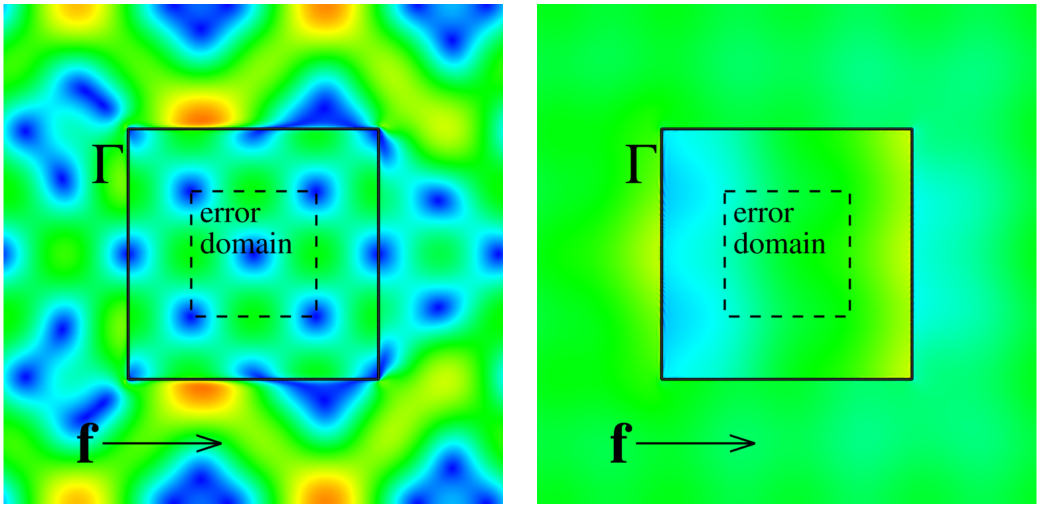

Figure 8: Simultaneous velocity magnitude (left) and pressure (right) snapshots of the Navier–Stokes Taylor–Green problem, with annotations describing the problem setup.

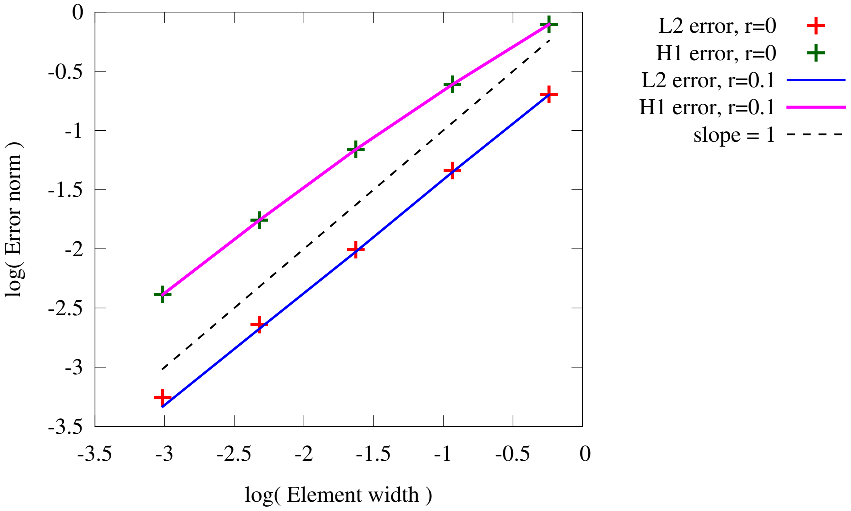

Figure 9: Convergence of the $L^2(\Omega^{\mathrm{err}})$ and $H^1(\Omega^{\mathrm{err}})$ errors for $r = 0$ and $r = 0.1$ for Navier–Stokes flow with a stationary boundary and positive viscosity.

3.3.3. Infinite Reynolds number

To demonstrate the robustness of the proposed methodology at realistic Reynolds numbers, we repeat the test of Section 3.3.2 with $\mu = 0$. The exact solution becomes tangentially discontinuous at Γ_t. This behavior is captured reasonably well, as shown in Figure 12, in spite of the application of (52) and (53), which provides no enforcement of tangential boundary conditions when $\mu = 0$. The nearly-linear convergence rates in local $L^2(\Omega^{\mathrm{err}})$ and $H^1(\Omega^{\mathrm{err}})$ seminorms are maintained as well, as shown in Figure 13, despite the fact that the global $H^1(\Omega)$ norm of the discontinuous exact solution is not well-defined. For $\mu = 0$ and the Δt–h relationship used here, (53) is $O(1)$ as $h \to 0$. Using $r > 0$ therefore introduces an $O(1)$ perturbation into the no-penetration constraint on Γ_t, so we would not expect asymptotic convergence. In this example, we therefore use $r = 0$. (Even for

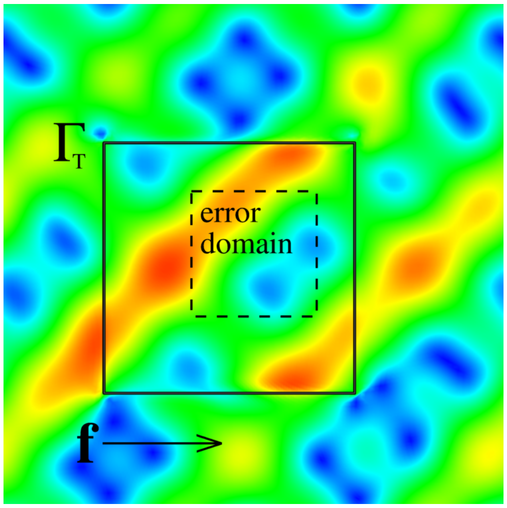

Figure 10: Annotated snapshot of velocity magnitude at time T for Navier–Stokes flow with moving boundaries and positive viscosity. (Note the translation of Γ relative to its initial position, shown in Figure 8.)

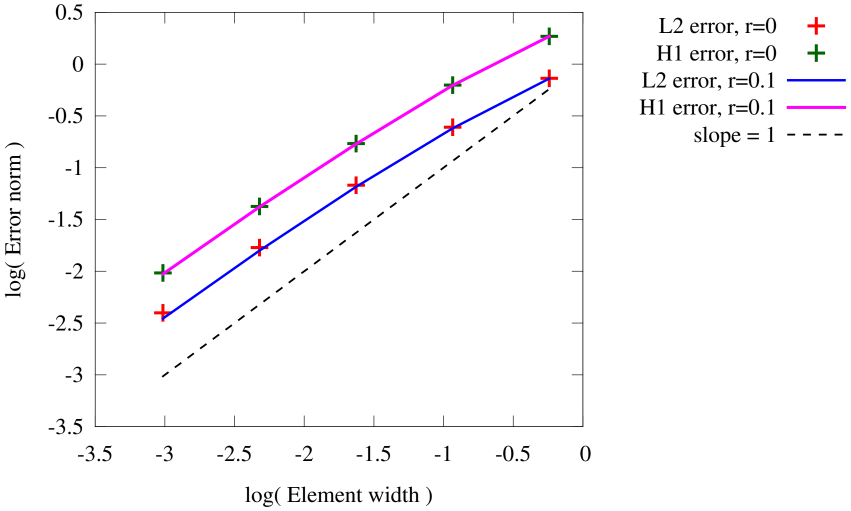

Figure 11: Convergence of the $L^2(\Omega^{\text{err}})$ and $H^1(\Omega^{\text{err}})$ errors for $r = 0$ and $r = 0.1$ for Navier–Stokes flow with moving boundaries and positive viscosity.

significant values of $r > 0$, though, we cannot practically refine the mesh enough for the resulting perturbation to dominate errors in this problem.)

Remark 10. Recall that the discrete formulation includes h-dependent artificial streamline diffusion (of the form (41)) to stabilize advection. In the absence of this diffusion, the solution becomes highly oscillatory.

4. Block iterative convergence

This section uses a linearized model problem to study the convergence of the block iterative procedure introduced in Section 2.5.3 to resolve a penalty-coupled FSI system.

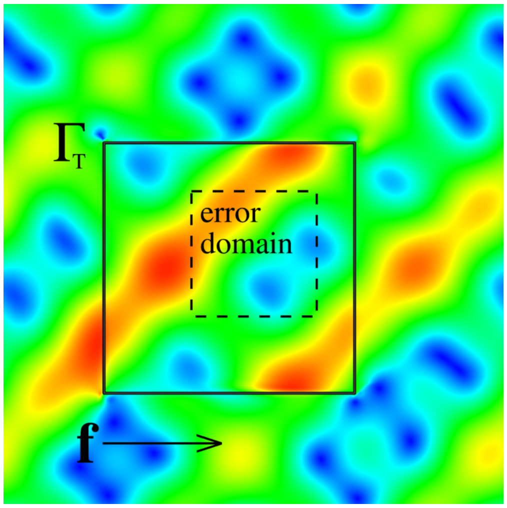

Figure 12: Annotated snapshot of velocity magnitude at time T for Navier–Stokes flow with moving boundaries and zero viscosity.

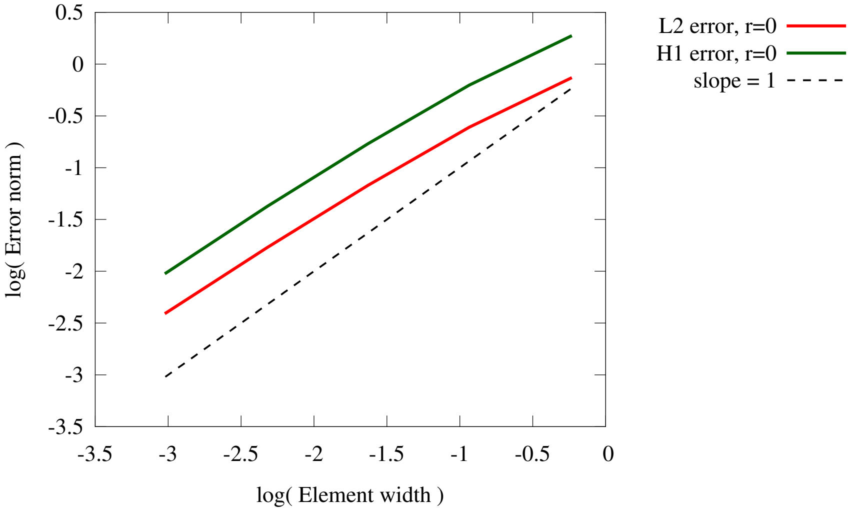

Figure 13: Convergence of the $L^2(\Omega^{\text{err}})$ and $H^1(\Omega^{\text{err}})$ errors for $r = 0$ for Navier–Stokes flow with moving boundaries and zero viscosity.

4.1. A generic model problem

The Lagrange multipliers are held fixed in the block iteration, so only the penalty coupling is of concern when investigating the stability of block iteration. We therefore introduce the following linear model problem, in which two linear elliptic subproblems, indexed 1 and 2, are coupled along an interface by penalty forces: Find $u_1 \in \mathcal{V}_1$ and $u_2 \in \mathcal{V}_2$ such that, for all test functions $w_1 \in \mathcal{V}_1$ and $w_2 \in \mathcal{V}_2$,

$$B_1(u_1, w_1) + k(u_1 - u_2, w_1)_\Gamma = F_1(w_1) \tag{190}$$

$$B_2(u_2, w_2) + k(u_2 - u_1, w_2)_\Gamma = F_2(w_2)\ . \tag{191}$$

In this problem, B_1 and B_2 are coercive and bounded bilinear forms, F_1 and F_2 are bounded linear functionals, $k > 0$ is the penalty constant coupling the two subproblems, and $(\cdot,\cdot)_\Gamma$ is an inner product of bounded traces of functions from $\mathcal{V}_1$ and $\mathcal{V}_2$. The block iterative algorithm for this problem is to start with $i = 0$ and an initial guess for u_2^0, then repeat

1. Holding u_2^i constant, find $u_1^{i+1} \in \mathcal{V}_1$ such that, for all $w_1 \in \mathcal{V}_1$,
$$B_1(u_1^{i+1}, w_1) + k(u_1^{i+1}, w_1)_\Gamma = k(u_2^i, w_1)_\Gamma + F_1(w_1) \; . \tag{192}$$
2. Holding u_1^{i+1} constant (at the value computed in the previous step) find $u_2^{i+1} \in \mathcal{V}_2$ such that, for all $w_2 \in \mathcal{V}_2$,
$$B_2(u_2^{i+1}, w_2) + k(u_2^{i+1}, w_2)_\Gamma = k(u_1^{i+1}, w_2) + F_2(w_2) \; . \tag{193}$$
3. $i \leftarrow i + 1$.

Remark 11. Note that, when the subproblems are linear, no initial guess is required for u_1^0. u_1^1 is completely determined by u_2^0.

We would like to know whether this procedure will converge to a fixed point. Let us define the norms
$$|||u|||_i^2 = ||u||_i^2 + k||u||_\Gamma^2 \; , \tag{194}$$
for $i \in \{1, 2\}$, where $||\cdot||_i$ is some norm in which B_i is coercive with unit constant (such as energy for B_i symmetric) and $||\cdot||_\Gamma$ is the norm induced by $(\cdot,\cdot)_\Gamma$. Then the bilinear form
$$\mathcal{B}_i(u, v) = B_i(u, v) + k(u, v)_\Gamma \tag{195}$$
will be coercive in the norm $|||\cdot|||_i$ with unit constant. We have Green's operators $\{\mathcal{G}_i\}_{i=1}^2$ such that if u_i satisfies
$$\mathcal{B}(u_i, w_i) = F(w_i) \qquad \forall w_i \in \mathcal{V}_i \; , \tag{196}$$
then
$$u_i = \mathcal{G}_i(F) \; , \tag{197}$$
i.e., $\mathcal{G}_i$ is a map from right-hand-side functionals to solutions, for subproblem i. Because the subproblems are linear, so are their solution operators. Using the Lax–Milgram theorem, with unit coercivity constant,
$$|||\mathcal{G}_i(F)|||_i \le |||F|||_i \; , \tag{198}$$
where the norm on the right-hand side is understood as the induced norm on the dual space $\mathcal{V}_i^*$. Expressing the solution u_1^{i+1} of Step 1 of the block iteration algorithm in terms of $\mathcal{G}_1$, we can

re-write Step 2 as

$$\mathcal{B}_2(u_2^{i+1}, w_2) = k\left(\mathcal{G}_1\left(k(u_2^i, \cdot)_\Gamma + F_1\right), w_2\right)_\Gamma + F_2(w_2)\ . \tag{199}$$

Expressing the solution of Step 2 in terms of its Green's operator, we then have a mapping from u_2^i to u_2^{i+1}:

$$u_2^{i+1} = \mathcal{G}_2\left(k\left(\mathcal{G}_1\left(k(u_2^i, \cdot)_\Gamma + F_1\right), \cdot\right)_\Gamma + F_2\right) = \mathcal{H}(u_2^i)\ . \tag{200}$$

For the block iteration to be stable, it is sufficient that $\mathcal{H}$ be a contraction mapping. Continuity of $(\cdot, w_1)_\Gamma$ and coercivity of $\mathcal{B}_1$ are sufficient to show that the convergence of subproblem 2 implies the convergence of subproblem 1. Using the linearity of $\mathcal{G}_1$ and $\mathcal{G}_2$ and bilinearity of the inner product $(\cdot, \cdot)_\Gamma$, it is easy to see that

$$\mathcal{H}(u) - \mathcal{H}(v) = \mathcal{G}_2\left(k\left(\mathcal{G}_1\left(k(u - v, \cdot)_\Gamma\right), \cdot\right)_\Gamma\right)\ . \tag{201}$$

Recalling (198), we can see that

$$\|\!|\mathcal{H}(u) - \mathcal{H}(v)|\!\|_2 \le C_1 C_2 \|\!|u - v|\!\|_2\ , \tag{202}$$

where C_1 and C_2 are defined such that

$$\|\!|k(u, \cdot)_\Gamma|\!\|_2 \le C_1 \|\!|u|\!\|_1 \qquad \forall u \in \mathcal{V}_1 \tag{203}$$

and

$$\|\!|k(u, \cdot)_\Gamma|\!\|_1 \le C_2 \|\!|u|\!\|_2 \qquad \forall u \in \mathcal{V}_2\ . \tag{204}$$

To show stability of block iteration, it is therefore sufficient to show that $C_1 \le 1$ and $C_2 \le 1$. Let us first proceed in a general way. For $(i, j) \in \{(1, 2), (2, 1)\}$,

$$\begin{aligned}
\|\!|k(u, \cdot)_\Gamma|\!\|_i &= \sup_{v \neq 0} \frac{k(u, v)_\Gamma}{\sqrt{\|v\|_i^2 + k\|v\|_\Gamma^2}} && (205)\\
&\le \sup_{v \neq 0} \frac{\sqrt{k}(u, v)_\Gamma}{\|v\|_\Gamma} && (206)\\
&\le \sqrt{k}\|u\|_\Gamma && (207)\\
&\le \|\!|u|\!\|_j\ . && (208)
\end{aligned}$$

This demonstrates that $C_1 \le 1$ and $C_2 \le 1$, and therefore that block iteration is at worst non-divergent.

4.2. *Application to FSI*

We would like to have greater insight into the rate of convergence of the iteration, and its dependence on the nature of the subproblems and the penalty parameter k. Specifically, we shall use further assumptions on the structures of B_1 and B_2 and trace and trace-inverse inequalities to sharpen the estimate in the step from (207) to (208). Consider the problem of dynamic linearized FSI, with subproblem 1 an incompressible Stokesian fluid occupying $\Omega_1 \subset \mathbb{R}^3$ and subproblem 2 a thin immersed structure modeled geometrically as the surface Γ, of co-dimension one to Ω_1. The inner product $(\cdot,\cdot)_\Gamma$ is the $L^2(\Gamma)$ inner product, with appropriate traces taken of its arguments when necessary. Further, we discretize implicitly in time, with the backward Euler method, using time step Δt. The time-discrete fluid physics are given by

$$B_1(u,v) = \frac{\rho_1}{\Delta t}(u,v)_{L^2(\Omega_1)} + a_1(u,v)\ , \tag{209}$$

where ρ_1 is the fluid mass density and a_1 is an $H^1(\Omega_1)$-coercive bilinear form. Rather than introducing a pressure to enforce incompressibility, simply consider $\mathcal{V}_1$ to be the space of discretely divergence-free velocities, to remain in the simpler setting of coercive problems. (Alternatively, in the case of pressure-stabilizing methods, the method is coercive over the whole pressure–velocity product space.) The structure physics are given by

$$B_2(u,v) = \frac{\rho_2 \ell_{\text{th}}}{\Delta t}(u,v)_\Gamma + \Delta t a_2(u,v)\ , \tag{210}$$

where ρ_2 is the structural mass density, ℓ_{th} is the structure's thickness, and a_2 is an $H^2(\Gamma)$-coercive bilinear form. For Stokes flow, a_1 is symmetric, so we can define the norms $\{\|\cdot\|_i\}_{i=1}^2$ by

$$\|u\|_i^2 = B_i(u,u)\ . \tag{211}$$

Suppose the coercivity constants for a_1 and a_2 are given by

$$|a_1(u,u)| \geq A_1 \|u\|^2_{H^1(\Omega_1)} \tag{212}$$

and

$$|a_2(u,u)| \geq A_2 \|u\|^2_{H^2(\Gamma)}\ . \tag{213}$$

Suppose further that we have the trace inequality

$$\|u\|^2_{H^1(\Omega_1)} \geq T \|u\|^2_\Gamma\ , \tag{214}$$

and the trace-inverse inequality

$$\|u\|^2_{L^2(\Omega_1)} \geq Ih\|u\|^2_\Gamma \, , \tag{215}$$

where h is a mesh parameter.Then it is clear that

$$\left(\frac{\rho_1 Ih}{\Delta t} + A_1 T + k\right)\|u\|^2_\Gamma \leq |\!|\!|u|\!|\!|^2_1 \tag{216}$$

and

$$\left(\frac{\rho_2 \ell_{\mathrm{th}}}{\Delta t} + \Delta t A_2 + k\right)\|u\|^2_\Gamma \leq |\!|\!|u|\!|\!|^2_2 \, . \tag{217}$$

Using these estimates in lieu of the duller bound (207)–(208), we can find that

$$C_1^2 = \frac{k}{\frac{\rho_1 Ih}{\Delta t} + A_1 T + k} \tag{218}$$

and

$$C_2^2 = \frac{k}{\frac{\rho_2 \ell_{\mathrm{th}}}{\Delta t} + \Delta t A_2 + k} \, . \tag{219}$$

Obviously we have $C_i < 1$, but if $|C_1 C_2 - 1| \ll 1$, then convergence of block iteration will be quite slow. Suppose the penalty parameter is given by

$$k = K/h \tag{220}$$

and the time step is given by

$$\Delta t = \tau h \, , \tag{221}$$

where K and τ are independent of the mesh parameter h. Then

$$C_1^2 \to 1 \quad \text{as} \quad h \to 0 \tag{222}$$

and

$$C_2^2 \to \frac{K}{\frac{\rho_2 \ell_{\mathrm{th}}}{\tau} + K} \quad \text{as} \quad h \to 0 \, . \tag{223}$$

The convergence therefore approaches a fixed rate under refinement. That rate can be improved by shrinking the time step–mesh size proportionality constant τ and/or decreasing the mesh-independent penalty parameter K. This is consistent with the trends noted in [16, Remark 14] and demonstrated in Section 5 of the sequel.

4.3. Relation to Newton iteration

Kamensky et al. [16, Section 4.6] introduced block iteration as a modification of Newton iteration with an approximate tangent. This section examines precisely how block iteration and inexact Newton iteration are related and indicates why block iteration is preferable. In the abstract model problem of Section 4.1, Newton iteration would have the tangent system

$$\begin{pmatrix} B_1(\cdot, w_1) + k(\cdot, w_1)_\Gamma & -k(\cdot, w_1)_\Gamma \\ -k(\cdot, w_2)_\Gamma & B_2(\cdot, w_2) + k(\cdot, w_2)_\Gamma \end{pmatrix} \begin{pmatrix} \Delta u_1 \\ \Delta u_2 \end{pmatrix}$$
$$= -\begin{pmatrix} B_1(u_1^i, w_1) + k(u_1^i - u_2^i, w_1)_\Gamma - F_1(w_1) \\ B_2(u_2^i, w_2) + k(u_1^i - u_2^i, w_2)_\Gamma - F_2(w_2) \end{pmatrix} , \tag{224}$$

which would, for a linear problem, arrive at the exact solution in a single iteration, from any initial guess. Eliminating off-diagonal blocks, we obtain two independent equations to update u_1 and u_2:

$$B_1(\Delta u_1, w_1) + k(\Delta u_1, w_1)_\Gamma = -B_1(u_1^i, w_1) - k(u_1^i - u_2^i, w_1)_\Gamma + F_1(w_1) \tag{225}$$

and

$$B_2(\Delta u_2, w_2) + k(\Delta u_2, w_2)_\Gamma = -B_2(u_2^i, w_2) - k(u_2^i - u_1^i, w_2)_\Gamma + F_2(w_2) \, . \tag{226}$$

Using $u_j^{i+1} = u_j^i + \Delta u_j$ for $j \in \{1, 2\}$, and the linearity of $B_j(\cdot, w_j)$ and $(\cdot, w_j)_\Gamma$, these two update equations are clearly equivalent to

$$B_1(u_1^{i+1}, w_1) + k(u_1^{i+1}, w_1) = k(u_2^i, w_1)_\Gamma + F_1(w_1) \tag{227}$$

and

$$B_2(u_2^{i+1}, w_2) + k(u_2^{i+1}, w_2)_\Gamma = k(u_1^i, w_2) + F_2(w_2) \, . \tag{228}$$

Unlike the problem of Section 4.1, inexact Newton iteration will require an initial guess for u_1^0, to compute u_2^1. For u_2^i, $i > 1$, we can follow analogous steps to those spelled out in Section 4.1 to derive a counterpart to (200):

$$u_2^{i+1} = \mathcal{H}(u_2^{i-1}) \, , \tag{229}$$

where $\mathcal{H}$ is the same as that defined in (200). Block iteration is therefore an acceleration of the inexact Newton approach that converges twice as quickly when the subproblems are linear.

Remark 12. Notice that the inexact Newton iteration, when applied to the problem of Section 4.2, would be equivalent to the following: putting the coupling force in explicitly and adding extra mass along the interface Γ in the tangent matrix for each subproblem. This is suggested heuristically by Tezduyar et al. in [133, Section 5.1], as a way to improve the robustness of classical Dirichlet-to-Neumann block iteration. In block iteration for penalty-coupled problems, there is a precise way to determine the amount of extra mass needed to guarantee stability. This interpretation suggests, however, that under-converging the block iteration may cause the structure to behave as if it has extra mass.

4.4. Numerical test

We now test the convergence of block iteration for the model coupled problem suggested in Section 3.2.3. In particular, we choose $\Omega = (-W/2, W/2)^2 \subset \mathbb{R}^2$ with $W = 2.5$ and select Γ to be the intersection of the line $x_2 = 3x_1 + W/4$ with Ω. We set

$$a_1(u, v) = (\nabla u, \nabla v)_{L^2(\Omega)} \ , \tag{230}$$

$$a_2(y, z) = (\nabla y, \nabla z)_{L^2(\Gamma)} \ , \tag{231}$$

$\rho_1 = \rho_2 = 1$, and select the functional F so as to strongly enforce $u = 1$ on the left edge of the domain. (We have both abused notation and stretched the problem definition in this example, by first conflating $u \in H^1_0(\Omega)$ with $u + g$, where g satisfies the inhomogeneous boundary condition, then selecting $g \notin H^1(\Omega)$. In computations, the discontinuous boundary data is implemented analogously to the "leaky lid" discretization of the lid-driven cavity benchmark, as depicted in [79, Figure 1].) A representative solution snapshot is shown in Figure 14. Notice that the Lagrange multiplier values, plotted as coloration along the physical image of Γ, are highly oscillatory, while the temperatures u and y remain qualitatively smooth.

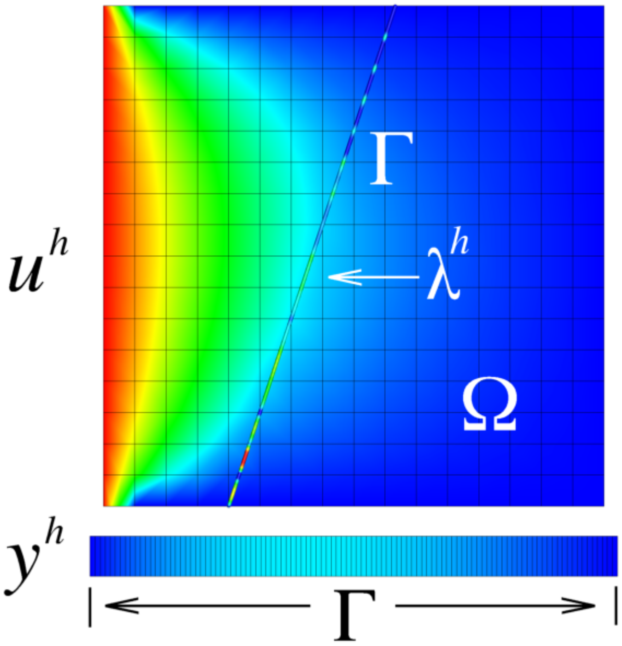

Figure 14: Annotated snapshot of a solution to the coupled model problem. The solution to the Γ subproblem, y^h, is plotted below Ω and the colors on Γ cutting through Ω represent point values of λ^h.

To investigate the effect of time step on block iterative convergence, we set $T = 10$ and take $\Delta t = T/N$ for $N \in \{1, 10, 100\}$, holding $\beta > 0$ fixed and $r = 0$. The (log of the) ℓ^2 norm of the discrete residual for the Γ subproblem during the first time step is shown as a function of the number of block iterations in Figure 15. (This differs from the choice of norm used in the convergence analysis, but, for a fixed number of degrees of freedom in the spatial discretization, all norms of the finite-dimensional solution space are equivalent.) The linear convergence rate and improvement with temporal refinement predicted in the preceding analysis are confirmed.

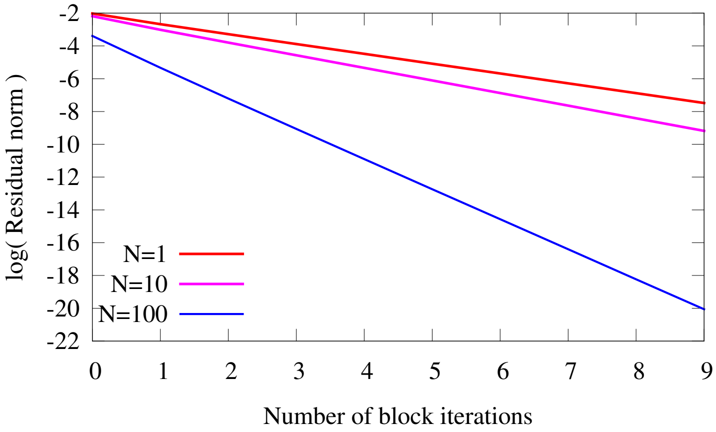

Figure 15: The norm of the discrete residual for the Γ subproblem converges linearly with a rate that improves as the time step $\Delta t = T/N$ decreases.

To investigate the effect of penalty parameter, we use $\Delta t = T/100$ and choose $\beta = C/h$, for $C \in \{1, 10, 100\}$ and h the mesh element size shown in Figure 14. The block iterative convergence is shown in Figure 16. This illustrates that block iterative convergence slows down with increasing penalty value. This highlights the value of including a semi-implicitly-integrated Lagrange multiplier rather than simply using a naive penalty method, in spite of these approaches having the same asymptotic convergence rates. The inclusion of the Lagrange multiplier allows for satisfactory constraint enforcement with lower (and therefore more computationally tractable) penalty values.

5. An FSI benchmark problem

To verify that the methodology extrapolates to the setting of large-displacement fluid–thin structure interaction, we study the performance of our div-conforming immersogeometric approach using a variant of the 2D non-coapting valve from [134] that has subsequently been used as a benchmark test by [16, 135–137]. As in our earlier study [16, Section 4.7] we look at the displacement history of a material point on the structure and compare immersogeometric and boundary-fitted results. We refer the reader to [16, Section 4.7] for the details of the boundary-fitted reference solution that we compare our immersogeometric computations against.

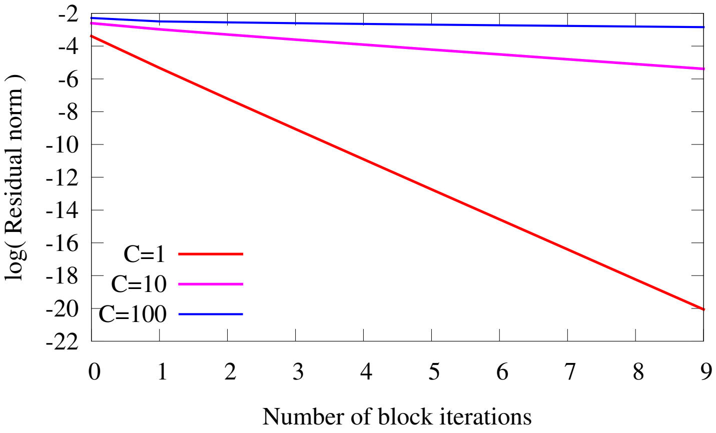

Figure 16: The norm of the discrete residual for the Γ subproblem converges linearly with a rate that slows down as the penalty C/h increases.

5.1. Problem definition

The problem is posed in two spatial dimensions and involves a pair of cantilevered beams immersed in incompressible Newtonian fluid, as shown in Figure 17. The fluid and structure have densities $\rho_1 = \rho_2 = 100$. The viscosity of the fluid is $\mu = 10$. The beams are modeled using the 2D degeneration of the shell formulation described in Section 2.1.3. The material model is isotropic St. Venant–Kirchhoff with Young's modulus $E = 5.6 \times 10^7$ and Poisson's ratio $\nu = 0.4$. The top and bottom of the channel have no-slip and no-penetration boundary conditions, the left end has a prescribed, time-dependent velocity profile, and the right end is traction free. The inflow velocity prescribed on the left end of the channel is

$$\mathbf{u}_1\left(x_2\mathbf{e}_2, t\right) = \begin{cases} 5(\sin(2\pi t) + 1.1)x_2(1.61 - x_2)\mathbf{e}_1 & , \quad t > 0 \\ \mathbf{0} & , \quad \text{otherwise} \end{cases} , \tag{232}$$

where the origin of the spatial coordinate system is at the bottom left corner of the domain. The fluid and structure are at rest at times $t < 0$. Considering the channel width to be a characteristic length scale and the peak inflow speed to be a characteristic flow speed, the Reynolds number is approximately 110. This low-Reynolds-number flow does not suffer from instabilities at the outflow face on the right end of the domain, and the traction boundary stabilization parameter γ is set to zero.

5.2. Immersogeometric discretizations with div-conforming B-splines

To demonstrate the convergence of div-conforming immersogeometric discretizations toward the boundary-fitted reference solution, we present results from a sequence of three immersogeometric discretizations. Although the problem domain is rectangular and we could simply employ the B-spline parameter space as physical space, we opt to demonstrate convergence with distorted

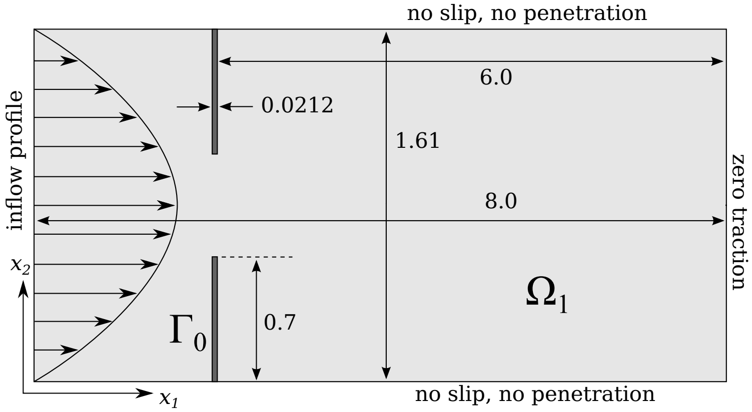

Figure 17: Geometry and boundary conditions for the 2D non-coapting valve benchmark. (This diagram is not to-scale.) The time-dependent inflow profile is (232).

fluid meshes by deforming the interior of the parametric domain while mapping it to the physical domain. For all of the immersogeometric discretizations, the fluid domain is discretized using a B-spline patch with the knot space $\widehat{\Omega}_1 = [0,1]\times[0,1]$. A point $\mathbf{X}$ in this knot space is (in the notation of Section 2.2.2) mapped to the physical domain Ω_1 with the mapping

$$\phi_1 = LX_1 \ , \tag{233}$$

$$\phi_2 = W\left(X_2 + \frac{s}{4}\left(1 - \cos\left(2\pi N X_1\right)\right)\left(X_2^2 - X_2\right)\right) \ , \tag{234}$$

where $L = 8$, $W = 1.61$, $N = 5$, and $s = 1.5$. For the coarsest mesh, M1, the B-spline knot space is subdivided into 32×128 Bézier elements and div-conforming B-spline velocity and pressure spaces of degree $k' = 1$ are defined on this mesh. The meshes, M2 and M3, use 64×256 and 128×512 elements respectively. The knot lines for M1 are drawn on the depiction of Ω_1 in Figure 18 to indicate the mesh distortion. Because resolution in the structure problem is far from being a limiting factor in accuracy, we use the same structure mesh in both problems, dividing each beam into 128 quadratic B-spline elements.

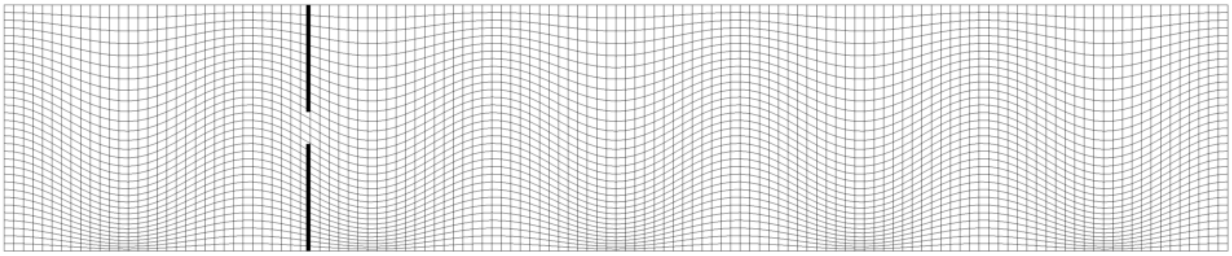

Figure 18: The physical image of the B-spline parameter space, showing the mesh of unique knots (thin lines) for M1 in relation to the beams (thick lines).

Normal-direction Dirichlet boundary conditions are enforced strongly, while tangential boundary conditions are enforced using the penalty method. The x_2 component of velocity at the inflow can easily be set to a nodal interpolant of the x_2 component of (232) when $k' = 1$, because the mapping $\boldsymbol{\phi}$ and the corresponding velocity push-forward involve only scaling by a constant factor at the inflow face of the domain. For computations on mesh $\mathrm{M}(N + 1)$, the penalty parameters are $\tau^B_{\mathrm{NOR}} = \tau^B_{\mathrm{TAN}} = C_{\text{no slip}} = 1000 \times 2^N$. The temporal discretization uses the backward Euler method with $\Delta t = 1.0 \times 10^{-2} \times 2^{-N}$. Six block iterations are used to couple the fluid and structure implicitly, reusing the fluid tangent from the first iteration. For this simple 2D problem, we solve for fluid increments in the block iteration using a direct solver, namely the MUltifrontal Massively Parallel sparse direct Solver (MUMPS) [138], accessed via PETSc.

5.3. Comparison of results

Figures 19 and 20 compare the x- and y-direction displacement histories of the tip of the upper beam in the three immersogeometric computations and the body-fitted reference (from [16, Section 4.7]). Refinement of the immersogeometric discretizations clearly brings this quantity of interest closer to the boundary-fitted reference curve. As in [16, Section 4.7], the pressure space still struggles to approximate the discontinuous exact solution, with the discrete solution exhibiting over- and under-shoot phenomena to either side of the immersed structure, as shown on M2 in Figure 21. However, in the context of immersed fluid–thin structure interaction, using div-conforming B-splines and the fluid–structure coupling method described above, the quality of the pressure solution is not especially important. The pressure is not involved in the computation of fluid–structure coupling forces and discrete fluid velocities computed using div-conforming methods are immune to pressure interpolation errors [67, (6.32)]. This is perhaps a counter-intuitive statement, because it stands in stark contrast to experience with most other numerical methods for incompressible flow, in which pressure interpolation error enters into *a priori* bounds on the velocity error. We go into more detail on exactly how this effect emerges in the stabilized finite element methods in Appendix A. The robustness of div-conforming B-spline discretizations to pressure jumps is illustrated in practical setting in Section 6. As expected from the theory, poor pressure approximation does not appear to have any ill effect on the velocity field, which remains smooth in Figure 21. It is also noteworthy that there is no visible asymmetry induced in the velocity solution by the asymmetric mesh distortion. One might expect "problems" on account of the lack of momentum conservation of the div-conforming discretization on mapped domains. This can be seen easily by observing that $\mathbf{w}_1 \equiv \mathbf{e}_i$ is not in the pushed-forward velocity test space. (Recall that the push-forward applied to velocity test and trial space basis functions rotates them, so they point along the mesh lines rather than the x_1 and x_2 axes.) However, we have not noticed any artifacts attributable to spurious momentum generation on deformed meshes.

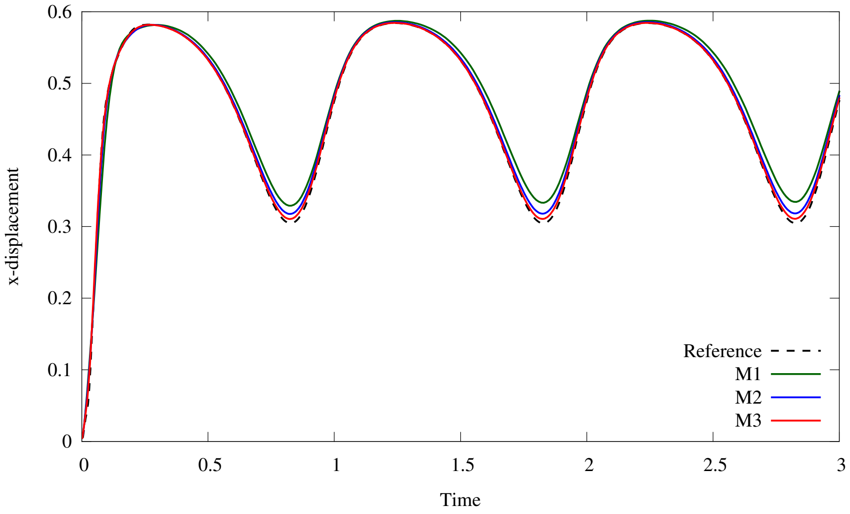

Figure 19: The x-direction displacement of the tip of the upper beam.

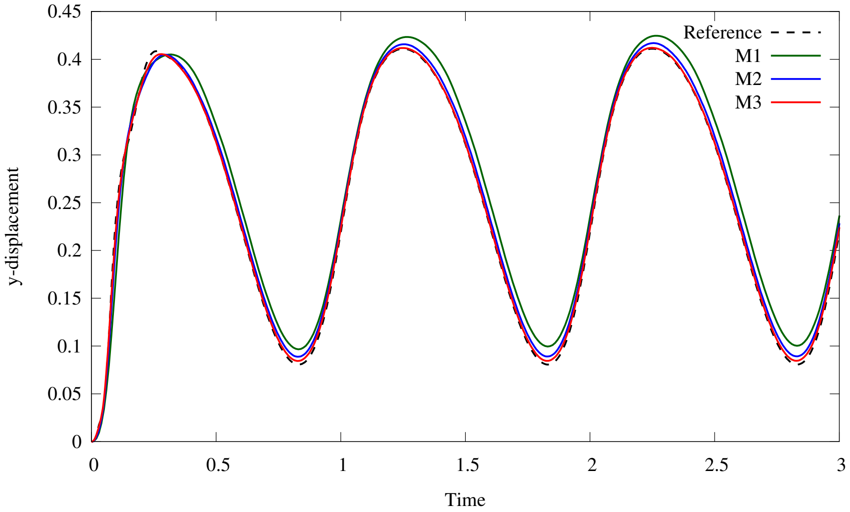

Figure 20: The y-direction displacement of the tip of the upper beam.

5.4. Block iterative convergence

We also use this problem to observe the behavior of block iteration "in the wild", on a nonlinear FSI problem. We restart the computation on M1 from the 50th time step and look at the ℓ^2 norm of the fluid subproblem residual vector (R_{f}, in the notation of Section 2.5.3) as a function of the number of block iterations. To illustrate the effects of the fluid–structure coupling penalties τ^B_{NOR} and τ^B_{TAN} and the time step, we restart with smaller and larger values of these parameters. The results are shown in Figure 22. The case with 10× larger time step requires the tangent matrix A_{f} to be recomputed every iteration. For the other cases, A_{f} is assembled on the first iteration only, then reused in subsequent iterations. Comparing Figure 22 with the analysis of Section 4 and Figures 15 and 16, we see that the overall conclusions from the linear model for block iteration carry over to

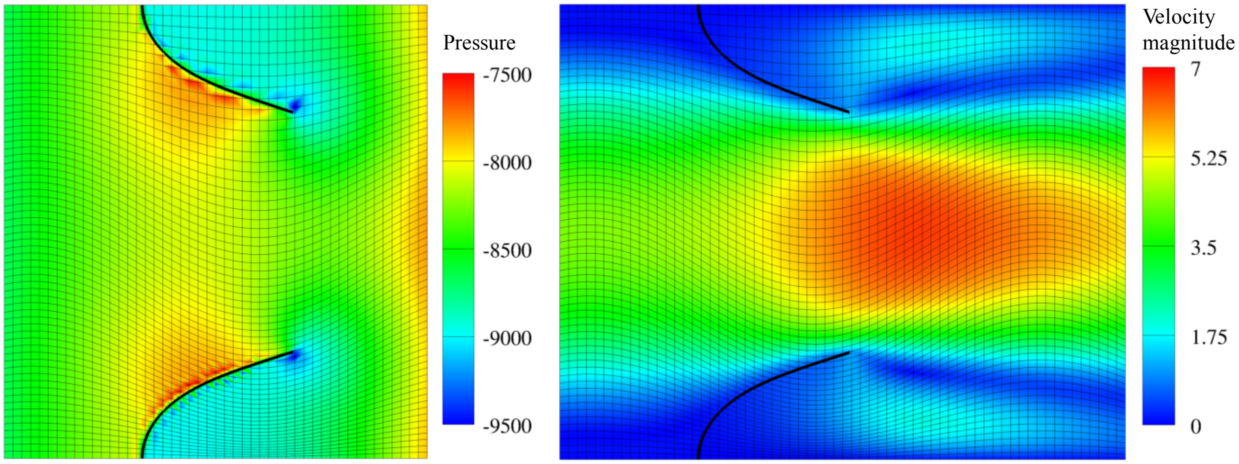

Figure 21: The pressure field (left) and the the velocity magnitude (right) at time $t = 0.5$ on M2.

the nonlinear case: increasing the penalty parameters and/or time step causes convergence to slow down while decreasing the penalty parameters and/or time step causes convergence to speed up.

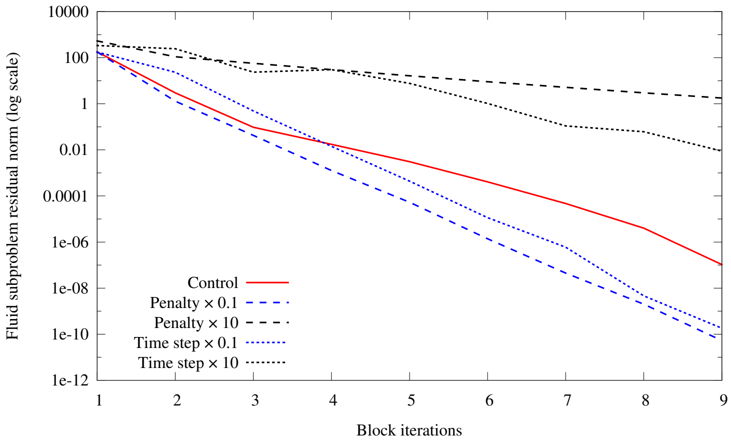

Figure 22: Convergence of block iteration in the 51^{st} time step, subject to different perturbations of the parameters used in the computation on M1 (the "control" case).

6. Heart valve closing under physiological pressure

A capability that is not verified by the testing of Section 5 is the effective simulation of closing heart valves. Recall from Section 1 that our motivation for using div-conforming B-splines for the fluid discretization is to avoid the *ad hoc* scaling of stabilization parameters that was needed to improve mass conservation in [16]. In principle, div-conforming B-splines should prevent mass loss altogether, but, in practice, for 3D problems, one generally does not solve the discrete algebraic problem exactly, as would be required for (24)–(27) to remain valid. This section demonstrates the feasibility of using div-conforming B-splines as a fluid discretization for heart valve FSI with inexact iterative solution of the discrete problem.

6.1. Test problem definition

The test problem that we use to illustrate the div-conforming discretization's potential for practical valve simulation is as follows. A variant of the valve geometry constructed in [16, Section Section 5.1] is immersed in a cylindrical fluid domain of radius 1.25 cm and height 3 cm. This geometry is derived from a finite element model of a bioprosthetic heart valve (BHV). BHVs are man-made replacements for diseased heart valves, with leaflets made from chemically-treated soft tissues that deliberately mimic the mechanics of naturally-occurring valves. The rigid extensions are added to the leaflets, as in [16], to block flow passing around the attached boundaries of the leaflets. The fluid subproblem posed on the cylindrical domain has traction boundary conditions on the ends and no-slip and no-penetration boundary conditions on the sides. The bottom face of the cylinder is subject to a time-dependent traction $\mathbf{h}_1 = P(t)\mathbf{e}_3$, where $P(t)$ is given by

$$P(t) = \begin{cases} P_1 & t < T_1 \\ at + b & T_1 \leq t \leq T_2 \\ P_2 & t > T_2 \end{cases} . \tag{235}$$

$P_1 = 2 \times 10^4$ dyn/cm^2 is the opening pressure applied before $T_1 = 0.05$ s, $P_2 = -10^5$ dyn/cm^2 is the closing pressure applied after $T_2 = 0.1$ s, and $a = (P_2 - P_1)/(T_2 - T_1)$ and $b = P_1 - aT_1$ are selected to continuously interpolate between the two states. The top face is subject to the traction boundary condition $\mathbf{h}_1 = \mathbf{0}$. The traction boundary stabilization scaling factor is set to $\gamma = 1$ on both sides. The properties of the fluid are $\rho_1 = 1$ g/cm^3 and $\mu = 4$ cP. The valve is modeled as an incompressible neo-Hookean material with shear modulus $\mu_s = 600$ kPa and density $\rho_2 = 1$ g/cm^3. The shell thickness is $h_{\text{th}} = 0.04$ cm. The attached edges of the valve leaflets are subject to a clamped boundary condition. The fluid and structure are initially at rest at time $t = 0$. This problem is not intended to be a physiologically realistic FSI model of a BHV in an artery. It is constructed to exhibit the same challenging flow conditions, for the purpose of demonstrating that div-conforming B-splines can easily circumvent difficulties encountered by methods that produce only weakly divergence-free velocity solutions.

6.2. Discretization

The cylindrical fluid domain is discretized using a B-spline knot space $\widehat{\Omega}_1 = [-1,1]\times[-1,1]\times[-1,2]$. A point $\mathbf{X}$ in this knot space is (in the notation of Section 2.2.2) mapped to the physical domain Ω_1 with the mapping

$$\phi_1 = RX_1 \sqrt{1 - \frac{1}{2}X_2^2} \tag{236}$$

$$\phi_2 = RX_2 \sqrt{1 - \frac{1}{2}X_1^2} \tag{237}$$

$$\phi_3 = LX_3 \tag{238}$$

with $R = 1.25$ cm and $L = 1$ cm. This mapping, illustrated in Figure 23, becomes singular at the corners of the parametric domain. A robust inverse of $\boldsymbol{\phi}(\mathbf{X})$ (as required for the immersed surface integration described in Section 2.4) is implemented by using Newton iteration with an exception to short-circuit the iteration and map $\boldsymbol{\phi}^{-1}(\mathbf{x})$ to a sentinel value outside of the knot space if $\mathbf{x}$ falls outside of the physical cylinder of radius R. (Otherwise, the singular nature of the mapping can prevent convergence.) The knot space is evenly subdivided into $40 \times 40 \times 40$ knot spans and div-conforming B-spline velocity and pressure spaces of degree $k' = 1$ are defined on this mesh. The no-penetration constraint on the sides of the cylinder is enforced strongly and the no-slip condition is enforced weakly by velocity penalization with penalty parameter $C_{\text{no slip}} = 10$ dyn/cm^2/(cm/s). The FSI coupling parameters are, using the notation of Section 2.5.1, $\tau^B_{\text{NOR}} = 1000$ dyn/cm^2/(cm/s), $\tau^B_{\text{TAN}} = 10$ dyn/cm^2/(cm/s), and $r = 0$. The contact parameters in the discrete structure subproblem are $k = 10^7$ dyn/cm^2/cm, $h_c = 0.005$ cm, and $c = 0.1$ cm. The temporal discretization uses the backward Euler method with $\Delta t = 5.0 \times 10^{-4}$ s. Six block iterations are used in each time step. The formulation is under-integrated, using a reduced quadrature rule with $(k' + 1)^d$ points in each

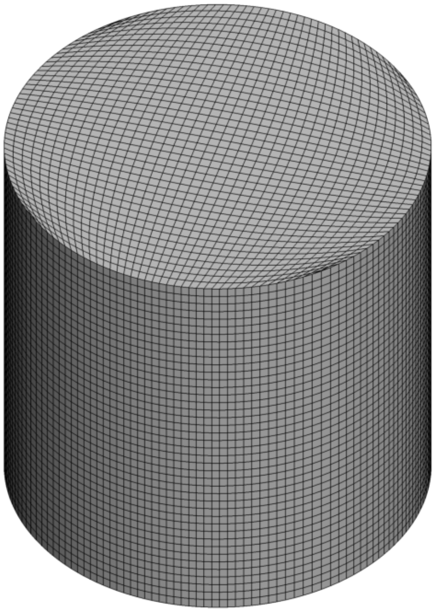

Figure 23: The physical image of the B-spline parameter space, showing the mesh of unique knots (black lines).

Bézier element. Typically $(k' + 2)^d$ points per element are needed to obtain optimal convergence rates with smooth solutions,[7] but, in the presence of immersed boundaries, convergence rates are limited by regularity of the exact solution.

6.3. Results

The opening of the valve is illustrated by several snapshots in Figure 24. The closed state at time $t = 0.197$ s is shown in Figure 25. The history of volumetric flow rate through the bottom of the cylinder is given in Figure 26, which indicates that the valve is able to block flow without the spurious apparent leakage that spoils solutions computed with unmodified stabilized formulations (cf. [16, Section 4.4.1]). These results illustrate the basic soundness of using div-conforming B-splines as a fluid discretization for heart valve FSI simulations. We now take a closer look at the mass conservation in the computed solutions. Because we use an iterative solver to approximate the fluid increments in the block iteration (Section 2.5.3), we do not expect $\nabla \cdot \mathbf{u}_1^h$ to be exactly zero. For the results presented above, we solve for fluid increments with the default Krylov method of PETSc (namely, GMRES(30) with a simple preconditioner)[8] to a relative tolerance of 10^{-2} for convergence of the preconditioned residual. Even with this loose tolerance, we avoid disastrous mass loss. We now recompute step 391 (at time $t = 0.1955$ s, when the valve is closed, under a large pressure jump) with a range of relative tolerances. For this experiment, we use the *un*preconditioned residual to measure convergence, so that results generalize more readily to other iterative solvers. The residual is assembled in centimeter–gram–second (CGS) units, without any scaling to compensate

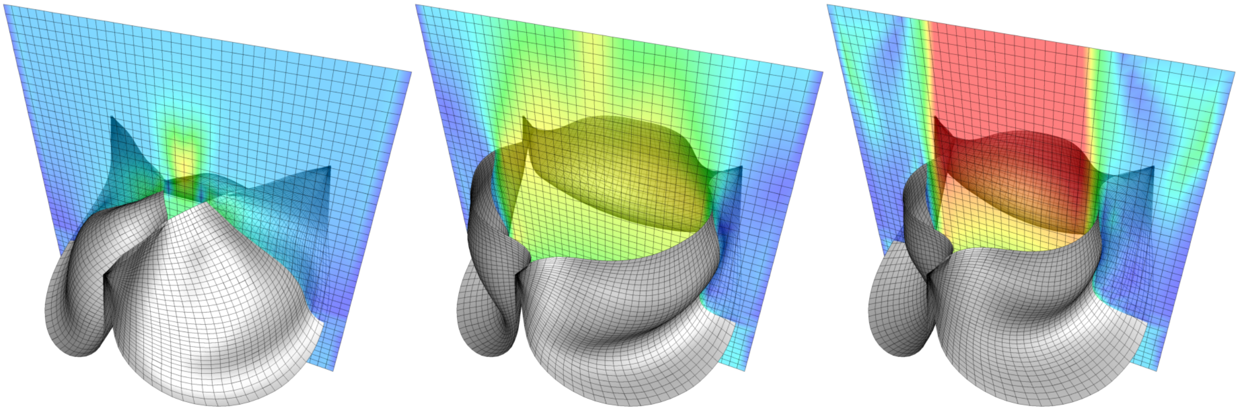

Figure 24: Snapshots of the opening process. Velocity magnitude is plotted on a slice, using a color scale ranging from 0 (blue) to ≥ 200 cm/s (red).

---

[7] That is, if one ignores the possibility of more efficient quadrature rules for IGA spline spaces, e.g. [139].

[8] This naive solver does not scale well with spatial refinement, which is entirely expected when solving saddle point problems, but the development of optimal linear solution strategies is beyond the scope of the present paper.

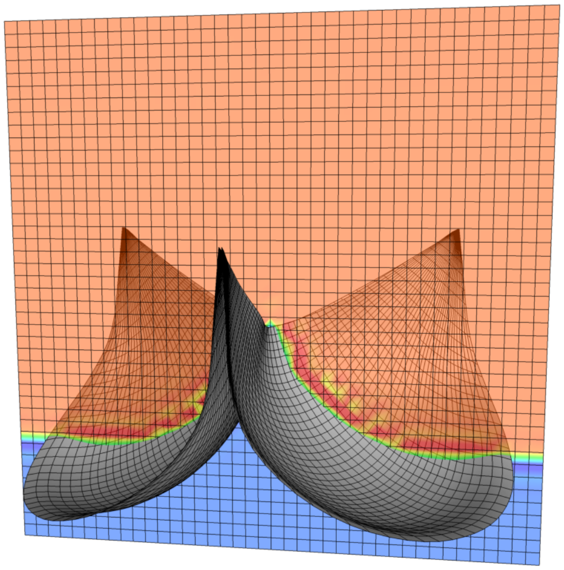

Figure 25: The closed valve at time $t = 0.16$ s. Pressure is plotted on a slice, using a color scale ranging from $\leq -1.1 \times 10^5$ dyn/cm^2 (blue) to $\geq 10^4$ dyn/cm^2 (red). Some over- and under-shoot is evident near the immersed structure.

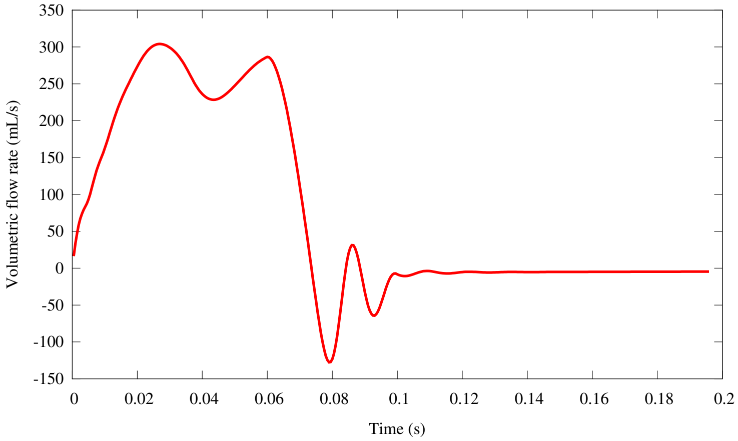

Figure 26: The volumetric flow rate through the cylinder.

for the difference in units between entries of the momentum and continuity equation residuals. The velocity divergence L^2 norms of the solutions to this time step are collected in Table 1. As expected, the velocity divergence approaches zero as the algebraic solution accuracy improves.

7. Simulating an *in vitro* experiment

The previous sections have endeavored to verify that the FSI analysis techniques described in this paper can accurately approximate solutions to the mathematical model stated in Section 2.1. However, this model is not guaranteed *a priori* to describe the dynamics of a heart valve immersed in fluid. The present section serves both to further illustrate the application of div-conforming

Table 1: The effect of relative tolerance in the approximate inversion of A_{f} (Section 2.5.3) on mass conservation.

Solver tolerance	$\|\nabla \cdot \mathbf{u}_1\|_{L^2(\Omega_1)}$ (CGS units)
10^{-1}	3.9×10^{-5}
10^{-2}	1.2×10^{-5}
10^{-3}	3.0×10^{-7}
10^{-4}	2.0×10^{-8}
10^{-5}	1.2×10^{-9}
10^{-6}	2.4×10^{-10}
10^{-7}	4.3×10^{-11}

B-splines to realistic problems and to argue that the modeling assumptions from Section 2.1 can represent the dynamics of an artificial heart valve immersed in fluid.

This section provides preliminary experimental validation of the model from Section 2.1 by qualitatively comparing FSI simulation outputs with the results of *in vitro* experiments using a latex valve in a device called a flow loop. A flow loop is an artificial hydraulic system comprising a series of fluid-carrying tubes connecting several components in a closed loop. Typically one component, the pump, drives fluid through the loop. This might be accomplished in a continuous manner by, e.g., a centrifugal pump, but, to construct *in vitro* models of cardiovascular systems, the pump is usually fashioned to mimic the action of a cardiac ventricle: a time-varying pressure is applied to a fluid-filled chamber, with valves upstream and downstream to ensure that this pressure induces a unidirectional flow through the loop. Additional components in the loop can tune the response of the flow to this pumping action by providing viscous drag, hydrostatic pressure differences (from changes in elevation), or pressure in proportion to stored fluid, known as hydraulic compliance. The measurements that we collect from the flow loop experiment are photographic images of the deforming valve and volumetric flow rate through it. The flow rate is used as data for the model we construct, while valve deformation is the feature of the physical system that the model is used to predict. We assess the validity of the model in the context of predicting valve deformation by qualitatively comparing the computed and photographed deformations.

Remark 13. The purpose of this section is emphatically *not* to experimentally validate the *numerical methods* described in this paper. Numerical methods approximate mathematical problems. The verification of numerical methods and their implementations (i.e. “solving the equations right”) is a separate concern from validation of mathematical models (i.e. “solving the right equations”) [140, Section 4, Rule 5]. Attempts to experimentally validate numerical methods or computer programs (rather than mathematical models) reflect confusion over the distinction between verification and validation.

7.1. Description of the experiment

The preliminary validation experiment consists of a latex valve in an acrylic tube. Volumetric flow rate through the tube is measured using an ultrasonic flow meter and images of the valve are collected using a borescope. Water is pumped through the tube using a flow loop system similar to the bioreactor detailed in [141]. The flow loop[9] is shown in Figure 27, with annotations indicating the locations of different components and the prevailing flow direction permitted by the valves. We are interested in FSI simulation of the segment between the pump and the flow meter, containing the artificial aortic valve, which is oriented to permit flow to leave the pump and prevent flow from entering the pump. The cyclical response of flow rate to pressure produced in the pump is highly sensitive to the precise configuration of the compliance chamber and resistor, along with the inertia of fluid in the loop, and additional resistance and compliance associated with other components. To avoid complications associated with experimentally controlling and mathematically modeling the interaction of the valve and adjacent fluid with the hydraulic components upstream and downstream of the valve location, we focus on the phase of the flow cycle during which the valve opens. In this

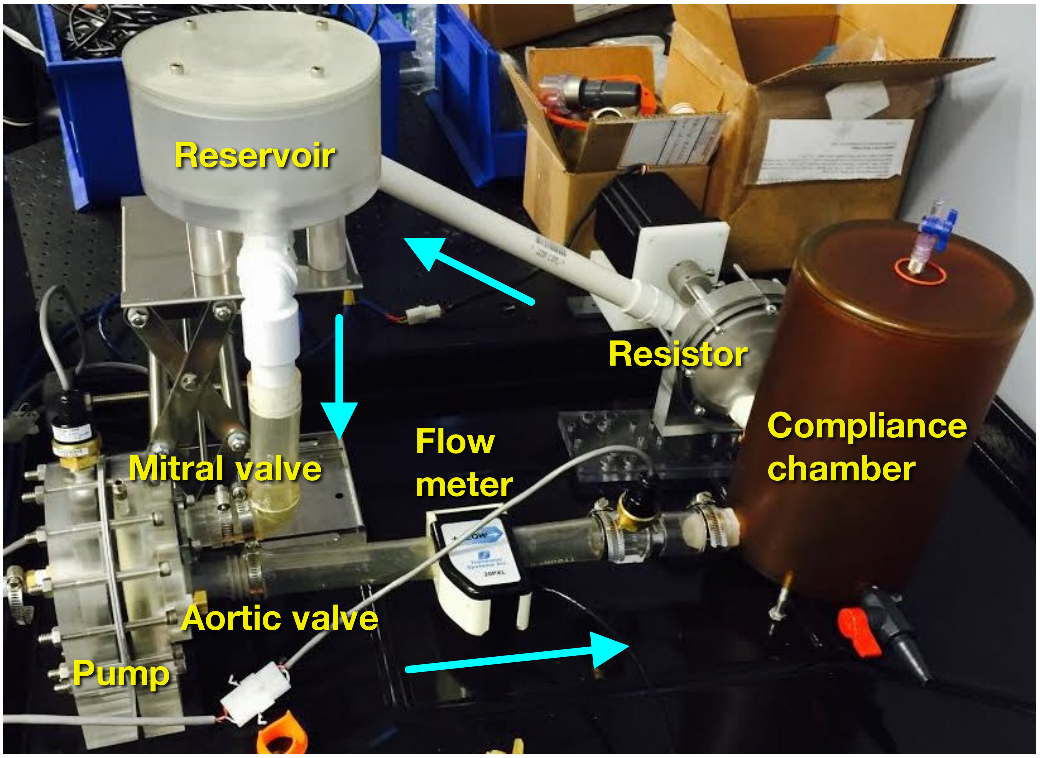

Figure 27: An annotated photograph of the flow loop. The blue arrows indicate the direction of flow permitted by the valves.

---

[9] The flow loop was designed and constructed with the assistance of an experimental team. Contributors to this effort are listed in the acknowledgments section of this paper.

limited context, the net effect of the components upstream and downstream of the valve can be seen as a black box determining the volumetric flow rate through the valve. Any configuration leading to the same flow rate would lead to essentially equivalent deformations of the valve. This is clearly *not* a reasonable assumption when studying valve closure, where the deformation of the valve is largely determined by the pressure difference across it, which can be altered without changing the (lack of) flow through the valve. In the case of a closing valve, the dynamics of the valve and adjacent fluid are inseparably coupled to the compliance, resistance, and fluid inertia upstream and downstream of the valve. Experimental reproducibility—which is an essential prerequisite to representing an experiment with a mathematical model [140, Section 4, Rule 8]—would depend on meticulous control over and documentation of the entire system, which is beyond the scope of the present validation effort.

Remark 14. The ability to accommodate valve closure under physiological pressure levels is one of the numerical method's distinguishing successes. However, the formulation of realistic boundary conditions to model specific animal circulatory systems or artificial fluidic devices (rather than merely obtaining Reynolds numbers and pressure differences of the right general magnitude) remains an open problem. The details of modeling a specific *in vitro* experiment will not likely carry over directly to the *in vivo* setting or even to other *in vitro* experiments. The scientific value of formulating, calibrating, and validating a sophisticated boundary condition to model the specific experiment described here is therefore questionable, as it would not clearly inform any future applications.

7.1.1. The acrylic tube

In this experiment, the valve is placed in a straight tube, illustrated in Figures 28 and 29. The inner diameter varies between 2 and 3 cm along the length of the tube, as shown in Figure 29, and is roughly the size of a typical human ascending aorta. To capture images of the valve, a hole is

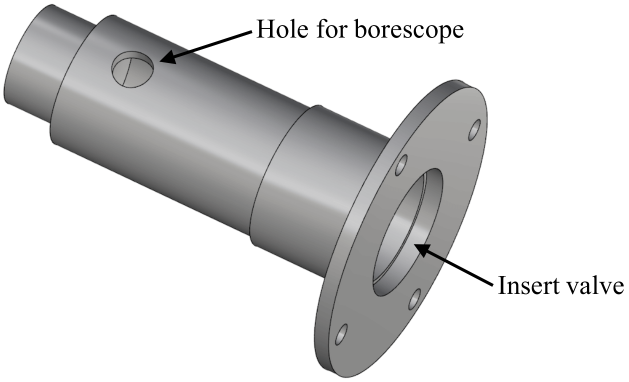

Figure 28: A 3D rendering of a CAD model of the acrylic tube.

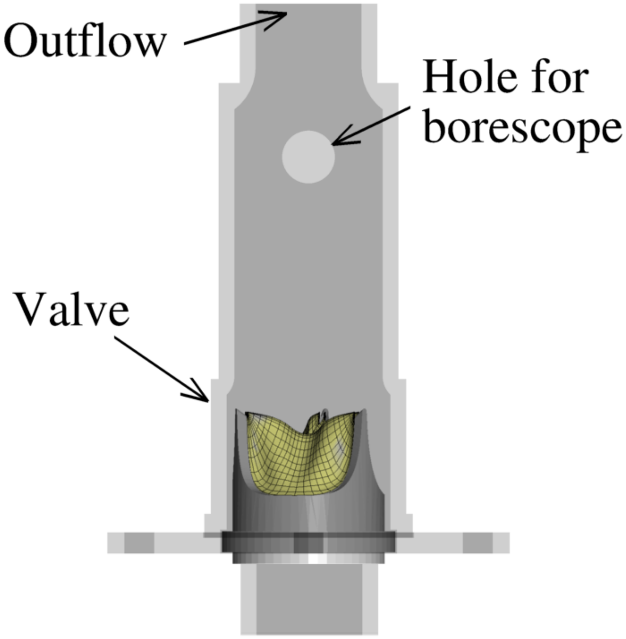

Figure 29: A 2D to-scale view of the tube, showing its relation to the valve and stent. The inflow and outflow have inner diameters of 2 cm.

included in the side of the tube, to permit insertion of a borescope. Using a mirror attachment to the end of the borescope's optical relay, this allows for a view of the valve from the aortic side as illustrated schematically in Figure 30.

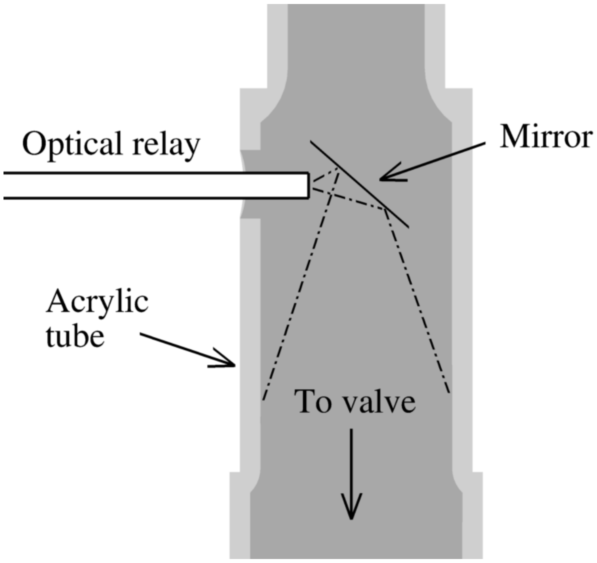

Figure 30: A schematic illustration of how images of the valve are captured.

7.1.2. *The valve*

We constructed the valve by attaching latex leaflets to an aluminum stent with superglue. The valve is shown in Figure 31. Each leaflet is cut from a flat sheet of latex with thickness 0.054 cm in such a way that the free edge is straight in the flattened configuration and the attached edge matches the geometry of the stent if the latex sheet is deformed into a cylinder without stretching. Cutting leaflets out from the latex sheet can be done to a high degree of precision (~ 0.05 cm), but the difficulty of gluing of leaflets onto the stent in a consistent manner is a major source of uncertainty in the experiment. In our estimation, this is the largest source of uncertainty affecting leaflet displacements during the opening phase of the flow cycle. The level of uncertainty in leaflet displacement introduced by inconsistencies in leaflet attachment can be roughly estimated by looking at the deviations from trefoil symmetry of the leaflets in their static equilibrium configuration shown in Figure 31.

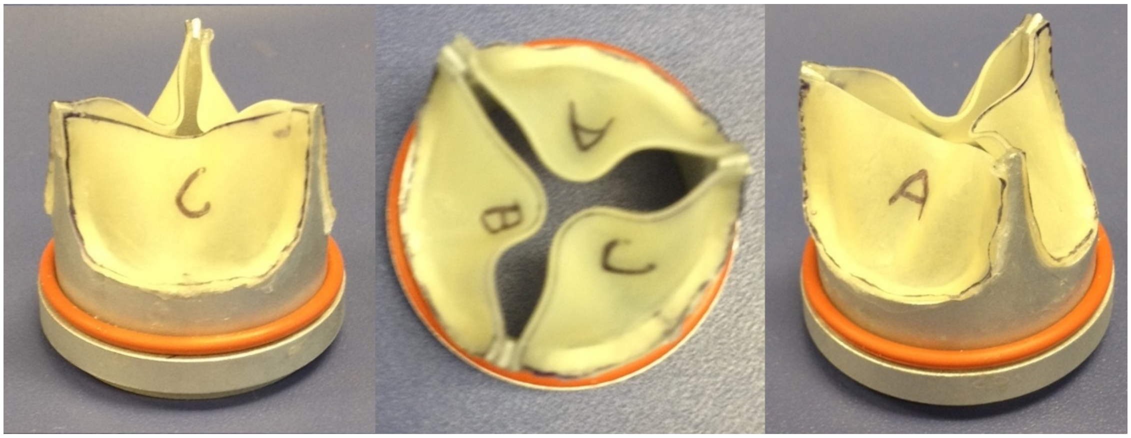

Figure 31: The physical valve used in the validation experiment.

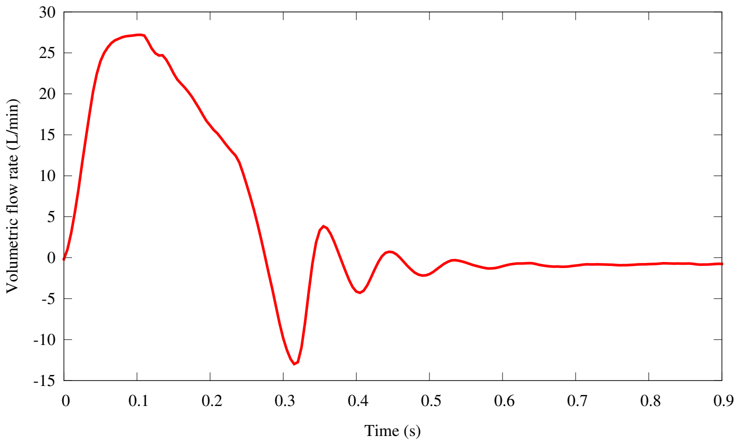

Figure 32: The measured volumetric flow rate used to set a Dirichlet boundary condition in the mathematical model.

7.2. *Mathematical model of the experiment*

This section specifies an instance of the mathematical problem stated in Section 2.1 that is designed to resemble the experiment described in Section 7.1.

7.2.1. *Fluid subproblem*

The mathematical model includes some deliberate simplifications of the geometry of the region occupied by fluid. Ω_1 consists of the image of a parametric space $\widehat{\Omega}_1 = (-1,1)\times(-1,1)\times(-1,4.5) \subset \mathbb{R}^3$ under the mapping $\boldsymbol{\phi}(\mathbf{X})$, which is defined by

$$\phi_1 = R(X_3)X_1\sqrt{1-\frac{1}{2}X_2^2}\ , \tag{239}$$

$$\phi_2 = R(X_3)X_2\sqrt{1-\frac{1}{2}X_1^2}\ , \tag{240}$$

$$\phi_3 = LX_3\ , \tag{241}$$

where $L = 1$ cm and $R(X_3)$ is defined by

$$R(X_3) = \begin{cases} R_{\text{in}} & X_3 < z_1 \\ R_{\text{out}} & X_3 > z_2 \\ (R_{\text{out}} - R_{\text{in}})\sin^2\left(\frac{\pi(X_3-z_1)}{2(z_2-z_1)}\right) + R_{\text{in}} & \text{otherwise} \end{cases}\ , \tag{242}$$

with $z_1 = -0.45$ cm, $z_2 = 0$, $R_{\text{in}} = 1$ cm, and $R_{\text{out}} = 1.4025$ cm. The shape of Ω_1 is shown in Figure 33. This is an admittedly crude approximation of the connection between the two tubes, but it is convenient from the standpoint of computing with a div-conforming B-spline space defined on a single patch.

The lateral sides of Ω_1 are subject to a no-slip and no-penetration condition. The inflow face of the domain is subject to a time-dependent plug flow boundary condition with the volumetric flow rate history shown in Figure 32. This flow rate was directly measured from the flow loop. The outflow face of the domain is subject to a traction-free boundary condition, including backflow stabilization with $\gamma = 1$. The fluid velocity initial condition is $\mathbf{u}_1^0 \equiv \mathbf{0}$. To model water, the viscosity of the fluid is set to $\mu = 1$ cP and the density is set to $\rho_1 = 1.0$ g/cm^3.

7.2.2. *Structure subproblem*

The latex is modeled as an incompressible neo-Hookean material with shear modulus $\mu_s = 8.7 \times 10^6$ dyn/cm^2 (based on uniaxial stretching experiments). Numerical experiments indicate that the leaflet opening kinematics are insensitive to this number, so long as it is the right order of magnitude, but the details of these numerical experiments have been omitted for brevity. We

Figure 33: The shape of the fluid subproblem domain, Ω_1, defined by applying the transformation (239)–(241) to a trivariate B-spline parameter space.

remark, however, that the strain distribution in closed leaflets (cf. [18, Figure 5]) or the opening kinematics in a *pressure*-driven flow would be more sensitive to leaflet material properties.

The geometry of the stress-free reference configuration Γ_0 is specified by manually selecting B-spline control points to generate the configuration shown in Figure 34. The leaflets are flat in Γ_0, based on the fact that the physical leaflets are cut out of a flat latex sheet. These leaflets are deformed into a static equilibrium configuration Γ_0', (a discrete approximation of) which is also shown in Figure 34. The boundary corresponding to the attached edge is subject to a strongly-enforced clamped boundary condition, in which displacement and derivatives of displacement are fixed to equal their values in Γ_0'. The stent is assumed to be rigid and its principle effect on the fluid is presumed to be merely preventing flow from passing between the wall of the tube and the attached leaflet edges. The stent is therefore modeled crudely in the FSI problem, as a rigid extension of the leaflets, closing the gap between the attached edge and the boundary of Ω_1. This extension is shown in relation to the leaflets in Figure 36. In a slight abuse of the notation introduced in Section 2.1, the leaflets are considered to be initially at rest in the deformed configuration Γ_0' (rather than the stress-free configuration Γ_0 which is used as a reference configuration in (8)). Figure 35 compares the model to the physical valve.

The "closed" equilibrium configuration shown in Figure 35 is not the unique static equilibrium configuration of the valve. Each leaflet can be snapped through to a stable open configuration. We found this necessary to ensure reproducible behavior in the experiment. (Otherwise, subtle, uncontrolled variations in the closed leaflet geometry lead to large differences in behavior between leaflets.) This also provides a simple analytical explanation for the insensitivity of opening kinematics to shear modulus. Analytical elimination of the pressure Lagrange multiplier from the 2nd Piola–Kirchhoff stress shows that the entire internal work term of (8) is proportional to μ_s, which

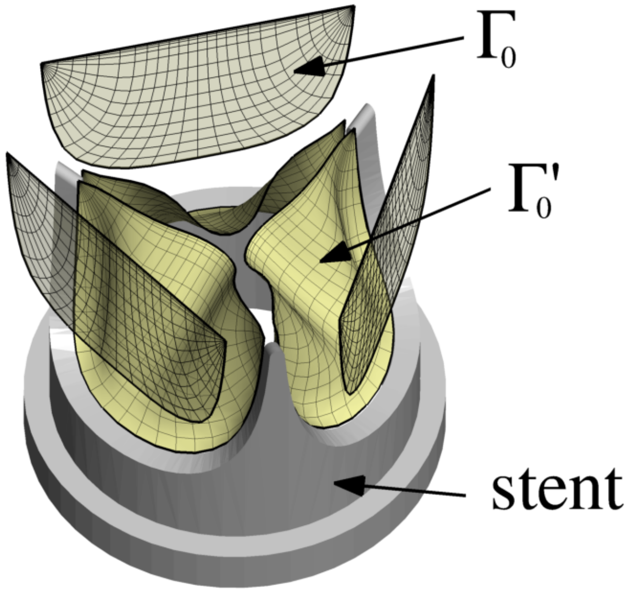

Figure 34: The reference (Γ_0) and initial (Γ_0') configurations of the valve model, shown in relation to a CAD model of the aluminum stent.

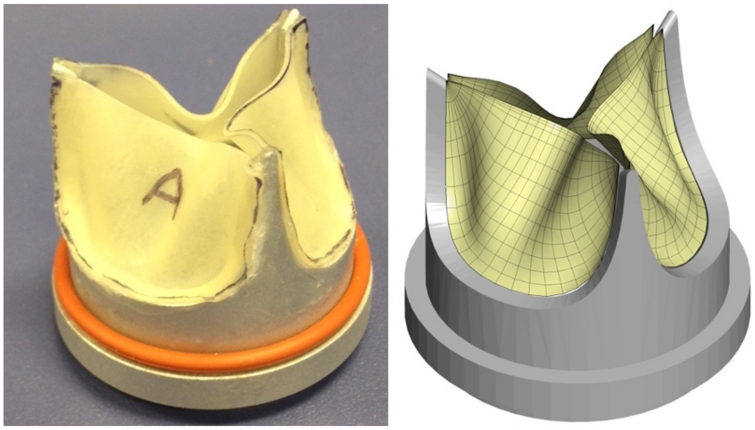

Figure 35: A visual comparison of the physical valve and its model, in the configuration Γ_0'.

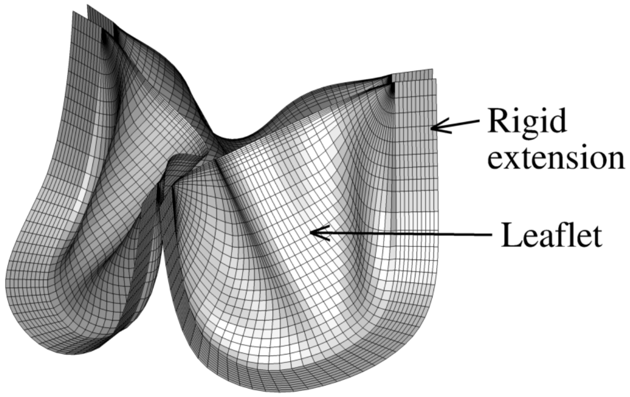

Figure 36: The rigid extensions closing the gap between the attached edges of the leaflets and the boundary of Ω_1.

means that a static equilibrium configuration with strongly enforced kinematic boundary conditions and no external loading is independent of μ_s. The (unloaded) closed and open configurations of the thin shell are therefore dictated by *geometry*, which perhaps partly explains the extreme improvements in performance that can be obtained from isogeometric discretizations of shell structures; see the comparison in [33] for a practical example in the context of heart valve structural analysis. Loosely speaking, fluid flow drives the opening valve over a material-dependent energy barrier separating these two material-independent equilibrium configurations. The prescription of a Dirichlet boundary condition at the inflow causes the force driving the fluid to adjust to the height of this energy barrier, lessening the apparent dependence of the system's dynamics on μ_s (relative to pressure-driven flow).

7.3. Discretization of the mathematical model

The fluid subproblem parametric domain $\widehat{\Omega}_1$ is split evenly into $64 \times 64 \times 99$ Bézier elements, used to define div-conforming B-spline spaces of degree $k' = 1$. The no-slip and inflow Dirichlet boundary conditions are enforced by velocity penalization, with penalty-constants of $C_{\text{no slip}} = 10$ dyn/cm^2/(cm/s) and $C_{\text{inflow}} = 1000$ dyn/cm^2/(cm/s) respectively, while the no-penetration condition on the lateral sides of the flow domain is enforced strongly. The renderings of the structure subproblem model in Figures 34 and 35 show the isogeometric discrete model, which consists of a 936-element quadratic B-spline mesh (with the element count excluding the rigid extensions shown in Figure 36). The equilibrium configuration Γ'_0 is approximated in the computational model by driving a structural dynamics simulation with mass damping from Γ_0 to a steady solution with the attached edges of the leaflets clamped into the configuration shown in Figure 34. The values of the contact penalty parameters are $k_c = 10^8$ (dyn/cm^2)/cm, $h_c = 0.04$ cm, and $c_c = 0.1$ cm. The FSI penalty parameters are $\tau^B_{\text{NOR}} = 1000$ dyn/cm^2/(cm/s) and $\tau^B_{\text{TAN}} = 10$ dyn/cm^2/(cm/s). The multiplier stabilization parameter r is set to zero. The backward Euler time integration method is used with $\Delta t = 2.5 \times 10^{-4}$ s. Seven block iterations, reusing A_f from the first, are used to converge the implicit phase of each time step. A_f is inverted approximately, using GMRES(300) (via PETSc, with the default preconditioning options) and a relative tolerance of 10^{-3} for the unpreconditioned residual.

7.4. Comparison of results

This section qualitatively compares the computational and experimental results. The experimental results consist of a flow rate history and a sequence of images taken through the borescope, as illustrated in Figure 30. The flow rate history is used as an input to the mathematical model, so it is vacuous to compare the flow rate measurements with the flow rates in the model. The measurements that remain for comparison are the sequence of images of the valve. Due to limitations of measurement equipment, we do not have information on when images were recorded in relation to the time axis of Figure 32. To associate images with values on the time axis of the flow rate plot in Figure 32, we first select an image of the valve in which it appears, subjectively, to be starting to open. Next, we assume that this corresponds to the time value at which the flow rate first becomes positive. Then we assign time values to subsequent images by assuming that they are captured at a constant frame rate. By counting the total number of frames and comparing with the number of times the valve opens, we estimate the frame rate to be 220 frames per second. We use this estimated rate, along with the subjectively-identified frame corresponding to $t = 0$, to assign time values to the experimental images. We estimate that this introduces several milliseconds of uncertainty into the temporal alignment of the images with the flow rate.

Figure 37 compares the computed valve deformations at several time points with images collected in the experiment. The time values given in this figure are synchronized with the time axis of the flow rate plot in Figure 32. The relative alignment in time of the photographic images is only accurate to within several milliseconds. For direct comparison with experimental images, the computed leaflet deformations are rendered using perspective (i.e. a pinhole camera model) from a vantage point that is positioned relative to the valve and stent in a way that corresponds to the location of the tip of the borescope the experiment.

Remark 15. The use of perspective and appropriate viewer position are critical to obtaining a qualitative correspondence in the results. When the leaflets are rendered using isometric perspective (i.e. the assumption that the scene is viewed from an infinite distance, which is applied by default in many visualization programs), the ventricular sides of the leaflets are not visible when the valve is fully open.

The main qualitative difference between these sets of images is in the degree of symmetry of the leaflet deformations during the transition to the fully open state. This difference is not unexpected given that the initial condition to the computer simulation is symmetrical while the physical valve is not. The degree of asymmetry in the valve is evident from the photographs in Figure 31. As explained in Section 7.1.2, this asymmetry is mainly due to differences in the stresses introduced by manually gluing each initially-flat leaflet into the stent. The physical valve assembled for this experiment is *nominally* symmetric (as per the stated experimental procedure), so the difference in behavior between leaflets is indicative of the degree of experimental reproducibility. Differences between the deformations of the three physical leaflets therefore put a lower bound on meaningful differences between computational and experimental results. Figure 37 also shows the computational results from a different view, with contour plots of fluid velocity magnitude on slices cutting through Ω_1. This illustrates the ability of computer simulations to provide additional information about the flow field and the full 3D deformation of the leaflets that would be difficult to measure experimentally.

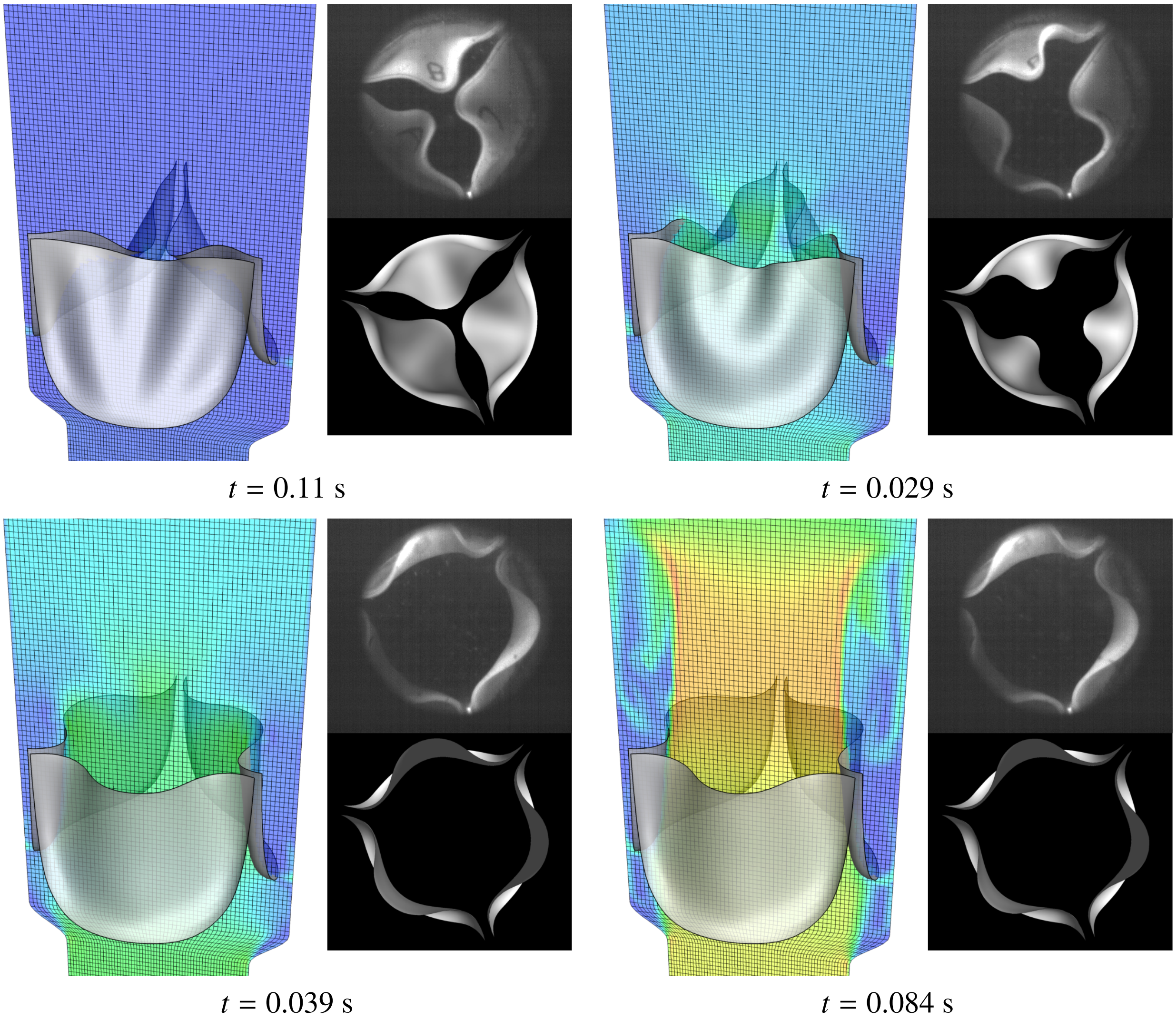

t = 0.11 s

t = 0.029 s

t = 0.039 s

t = 0.084 s

Figure 37: Several snapshots of the computed solution, compared with experimental images. At each time instant, the computed solution is shown in the left-hand frame and at the bottom of the right-hand frame. The experimental results are shown in the top of the right-hand frame. Colors indicate fluid velocity magnitude on a slice. Color scale: 0 (blue) to ≥200 cm/s (red).

The qualitative resemblance of computed leaflet deformations to the observed deformations indicates that the modeling assumptions of Section 2.1 are not wildly inappropriate for predicting the deformations of heart valve leaflets immersed in physiological flow fields and may be able to predict quantities of interest related to deformation (such as strain) with practically-useful accuracy. We see agreement with qualitative features of artificial valve leaflet deformations observed in other *in vitro* experiments as well. The computed solution at time $t = 0.029$ s shows the opening process, as characterized by reversal of leaflet curvature, beginning primarily near the attached edge, in the so-called belly region of the leaflet. This is in agreement with the observations of Iyengar et al. [142] who used images captured from multiple vantage points to reconstruct 3D deformations of valve leaflets *in vitro*. As we demonstrated earlier in [18], this behavior is *not* captured by simulations using structural dynamics alone, which underscores the importance of accounting for FSI in heart valve modeling. These preliminary results are therefore sufficient to justify the nontrivial expenses associated with more rigorous experimental validation in the future.

8. Conclusions and further work

In this work we show that divergence-conforming B-spline discretizations of incompressible flow are a practical tool for eliminating mass conservation errors from FSI computations with thin immersed structures, such as heart valve leaflets. Divergence-conforming discretizations also allow for a direct analogy to linear parabolic model problems, for which we can prove the convergence of an immersed method that we previously found effective for analyzing heart valve FSI [16].

The most immediate difficulties faced in extending div-conforming B-splines to higher-fidelity heart valve FSI models are the development of more efficient linear solution strategies for the fluid subproblem and the introduction of a turbulence model. Progress in both of these directions has already been made. The discrete de Rahm complex that the div-conforming B-spline spaces are part of can be exploited to develop highly efficient linear solvers, as originally studied by Hiptmair [143] and later, in the context of incompressible flow, by Evans [66, page 276] and Kanschat and Mao [144]. Van Opstal et al. [145] recently obtained very promising results from a variational multiscale (VMS) turbulence modeling approach [146] based on div-conforming B-splines, building on the subgrid vortex approach mentioned in [66, page 272] and [147]. We anticipate that these advances can be adapted to the problem setting explored in this paper to improve the efficiency and accuracy of immersogeometric heart valve simulations. Another way to improve the efficiency of immersogeometric computations would be to include local refinements near immersed boundaries. Local refinement of divergence-conforming spline discretizations was recently studied by Johannessen et al. [148], using LR B-splines [149].

Additional research directions suggested by this work include sharpening the *a priori* estimates derived for linear problems and possibly extending some of them to nonlinear problems. We may also be able to improve efficiency by rendering more aspects of the solution algorithm explicit, as is in many previous computations using feedback boundary conditions (as reviewed thoroughly in Section 2.5.4).

Acknowledgments

The flow loop used for the experiment described in Section 7 was developed by a team affiliated with the Center for Cardiovascular Simulation (CCS) at the University of Texas at Austin, consisting of Hugo Landaverde, Javier Solis, John G. Lesicko, Jordan L. Graves, Mitchell A. Katona, and Samuel Petter. Bruno Rego (also with CCS) performed the experiments to estimate the shear modulus of the latex used in the leaflets. Their efforts are gratefully acknowledged. Funding for this work was supported by NIH/NHLBI Grants No. R01 HL108330, R01 HL070969 and R01 HL129077. D. Kamensky was partially supported by the CSEM Graduate Fellowship. M.-C. Hsu was partially supported by the ARO Grant No. W911NF-14-1-0296. Y. Yu was partially supported by the Lehigh FRG Faculty Grant and the Simons Collaboration Grant. J.A. Evans was partially supported by AFOSR Grant No. FA9550-14-1-0113. This support is gratefully acknowledged. We thank the Texas Advanced Computing Center (TACC) at the University of Texas at Austin for providing HPC resources that contributed to this research. We would also like to thank Professor Daniele Boffi at the University of Pavia for helpful discussions on the mathematical analysis.

Appendix A. Scaling stabilization parameters to improve mass conservation

This appendix provides an *a priori* explanation of how the scaling of stabilization parameters proposed in [16, Section 4.4.2] improves approximation of hydrostatic immersed boundary FSI solutions (such as closed heart valves). If an immersed boundary induces a large pressure jump in the fluid, it is acting as a concentrated irrotational force. We isolate the effects of such a force by looking at a linear model problem: the Stokes "no-flow" problem. This problem is introduced precisely by Galvin et al. [62]. Briefly, it is a Stokes flow with homogeneous Dirichlet boundary conditions and an irrotational body force. The exact solution is hydrostatic, with a pressure field equal to the potential generating the irrotational force field. (This is also an exact solution to the nonlinear Navier–Stokes equation.) In a numerical method, if the pressure interpolation error enters the bound on the velocity error, then the discrete velocity may be nonzero. If the pressure gradient in the exact solution is very large relative to other data in the problem, then the discrete velocity solution can be very far from hydrostatic. This problem occurs quite dramatically in heart valve FSI analysis with stabilized finite element discretizations of the fluid subproblem. The effect of the pressure interpolation error on velocity manifests, in the valve problem, as poor mass conservation near the valve, which leads to a *de facto* leakage through it, even when the fluid–structure kinematic constraint is well-enforced. See [16, Section 4.4.1] for an illustration of this effect.

As mentioned in Section 1, Galvin et al. [62] investigated the phenomenon of poor mass conservation in incompressible flows with irrotational forcing using inf-sup stable pairs of velocity and pressure spaces, and found that, in the presence of large irrotational forces, it is beneficial to use unusually-high grad-div stabilization constants. Grad-div stabilization is the same thing as least squares for the incompressibility constraint (LSIC) [150], i.e. the stabilization term multiplied by τ_C in the variational multiscale (VMS) fluid subproblem formulation of [16]. Galvin et al. scaled τ_C globally by factors of up to 10^4, but found that excessive scaling could lead to bad results. When doing immersed boundary analysis with the VMS fluid formulation, there are two key departures from the setting explored by Galvin et al.:

1. We know *a priori* where the large irrotational forces (and thus large pressure interpolation errors) will be located. Specifically, we know that the forces will be in fluid elements containing the immersed structure.
2. The pressure interpolation error contributes to the velocity error not only through the Galerkin term of the weak continuity equation, but also through the appearance of the pressure gradient in the momentum residual $\mathbf{r}_{\mathrm{M}}$, in the stabilization terms. These contributions to the velocity error are controlled by the streamline upwind Petrov–Galerkin (SUPG) [78] stabilization constant τ_{M}, which is also used for pressure stabilizing Petrov–Galerkin (PSPG) [79] stabilization. We might therefore expect to benefit from modifying τ_{M} in addition to τ_{C}.

We now do some simple error analysis for the VMS formulation applied to the generic no-flow problem. The VMS analysis leading to the Navier–Stokes discretization used in [16] reduces, in the case of steady Stokes flow, to the PSPG formulation [79] augmented with LSIC. The PSPG/LSIC discrete problem is: Find $\{\mathbf{u}^h, p^h\} \in \mathcal{S}_u^h \times \mathcal{S}_p^h$ such that $\forall \{\mathbf{w}^h, q^h\} \in \mathcal{V}_u^h \times \mathcal{V}_p^h$,

$$B^{\mathrm{PSPG}}(\{\mathbf{u}^h, p^h\}, \{\mathbf{w}^h, q^h\}) = F^{\mathrm{PSPG}}(\{\mathbf{w}^h, q^h\}) \ , \tag{A.1}$$

with

$$\begin{aligned} B^{\mathrm{PSPG}}(\{\mathbf{u}^h, p^h\}, \{\mathbf{w}^h, q^h\}) = \mu \int_\Omega \nabla \mathbf{u}^h : \nabla \mathbf{w}^h \, d\Omega + \int_\Omega q^h \nabla \cdot \mathbf{u}^h \, d\Omega - \int_\Omega p^h \nabla \cdot \mathbf{w}^h \, d\Omega \\ + \sum_e \int_{\Omega^e} \tau_{\mathrm{M}}^e \nabla q^h \cdot (-\mu \Delta \mathbf{u}^h + \nabla p^h) \, d\Omega \\ + \sum_e \int_{\Omega^e} \tau_{\mathrm{C}}^e \nabla \cdot \mathbf{u}^h \nabla \cdot \mathbf{w}^h \, d\Omega \ , \end{aligned} \tag{A.2}$$

where the PSPG stabilization constant $\tau_{\mathrm{M}}^e = O(h^2/\mu)$ and the LSIC stabilization constant $\tau_{\mathrm{C}}^e = O(h^2/\tau_{\mathrm{M}}^e)$ are steady Stokes flow counterparts to the synonymous stabilization constants that appear in the unsteady Navier–Stokes VMS formulation. τ_{M}^e must obey an upper bound (derived from inverse estimates that bound higher derivatives of discrete polynomial test and trial functions in terms of lower derivatives) for B^{PSPG} to be coercive in the so-called "stability norm",

$$|||\{u, p\}|||^2 = \frac{1}{2}\mu \|\nabla \mathbf{u}\|_{L^2(\Omega)}^2 + \frac{1}{2} \sum_e \tau_{\mathrm{M}}^e \|\nabla p\|_{L^2(\Omega^e)}^2 + \frac{1}{2} \sum_e \tau_{\mathrm{C}}^e \|\nabla \cdot \mathbf{u}\|_{L^2(\Omega^e)}^2 \ , \tag{A.3}$$

introduced in [79] and extended here to include an LSIC contribution. Following the analysis of [79], we decompose the error into discrete and interpolation components. Let the exact solution be $\{\mathbf{u}, p\}$. The error is then defined to be

$$\{\mathbf{e}_u, e_p\} = \{\mathbf{u}^h - \mathbf{u}, p^h - p\} \, . \tag{A.4}$$

Adding and subtracting arbitrary discrete functions $\bar{\mathbf{u}}^h \in \mathcal{V}_u^h$ and $\bar{p}^h \in \mathcal{V}_p^h$, we obtain

$$\mathbf{e}_u = \left(\mathbf{u}^h - \bar{\mathbf{u}}^h\right) + \left(\bar{\mathbf{u}}^h - \mathbf{u}\right) = \mathbf{e}_u^h + \boldsymbol{\eta}_u \, , \tag{A.5}$$

$$e_p = \left(p^h - \bar{p}^h\right) + \left(\bar{p}^h - p\right) = e_p^h + \eta_p \, , \tag{A.6}$$

where $\boldsymbol{\eta}_u = \bar{\mathbf{u}}^h - \mathbf{u}$ is the velocity interpolation error and $\eta_p = \bar{p}^h - p$ is the pressure interpolation error. These interpolation errors are unrelated to the numerical method, and depend only on the exact solution and choice of discrete spaces.

In the particular case of the no-flow problem, we can exactly interpolate the velocity $\mathbf{u} = \mathbf{0}$ by choosing $\bar{\mathbf{u}}^h = \mathbf{0}$, so $\boldsymbol{\eta}_u = \mathbf{0}$. Thus $\mathbf{e}_u = \mathbf{e}_u^h = \mathbf{u}^h$. We can therefore bound the H^1 seminorm of the spurious flow in the discrete solution in terms of the stability norm of the discrete error:

$$\frac{1}{2}\mu |\mathbf{u}^h|^2_{H^1(\Omega)} \leq \left|\!\left|\!\left| \left\{\mathbf{e}_u^h, e_p^h\right\} \right|\!\right|\!\right|^2 \, . \tag{A.7}$$

Because the PSPG/LSIC bilinear form is, by design, coercive with unit constant in the stability norm, we have

$$\left|\!\left|\!\left| \{\mathbf{e}_u^h, e_p^h\} \right|\!\right|\!\right|^2 \leq \left| B^{\mathrm{PSPG}}\left(\{\mathbf{e}_u^h, e_p^h\}, \{\mathbf{e}_u^h, e_p^h\}\right) \right| \, . \tag{A.8}$$

Because PSPG/LSIC is strongly consistent with the exact solution, we have

$$B^{\mathrm{PSPG}}\left(\{\mathbf{e}_u, e_p\}, \{\mathbf{w}^h, q^h\}\right) = 0 \tag{A.9}$$

for all discrete test functions $\{\mathbf{w}^h, q^h\}$. Thus

$$\left|\!\left|\!\left| \{\mathbf{e}_u^h, e_p^h\} \right|\!\right|\!\right|^2 \leq \left| B^{\mathrm{PSPG}}\left(\{\boldsymbol{\eta}_u, \eta_p\}, \{\mathbf{e}_u^h, e_p^h\}\right) \right| \, . \tag{A.10}$$

Recalling that, for the no-flow problem, $\boldsymbol{\eta}_u = \mathbf{0}$, and using the definition of B^{PSPG},

$$B^{\mathrm{PSPG}}\left(\{\boldsymbol{\eta}_u, \eta_p\}, \{\mathbf{e}_u^h, e_p^h\}\right) = -\int_\Omega \eta_p \nabla \cdot \mathbf{e}_u^h \, d\Omega + \sum_e \int_{\Omega^e} \tau_{\mathrm{M}} \nabla e_p^h \cdot \nabla \eta_p \, d\Omega \, . \tag{A.11}$$

Splitting the first integral into a sum over elements and using Young's inequality in each term,

$$\left|B^{\mathrm{PSPG}}\left(\{\boldsymbol{\eta}_u, \eta_p\}, \{\mathbf{e}_u^h, e_p^h\}\right)\right| \leq \sum_e \left(\frac{\|\eta_p\|^2_{L^2(\Omega^e)}}{2\epsilon_1^e} + \frac{\epsilon_1^e \|\nabla\cdot\mathbf{e}_u^h\|^2_{L^2(\Omega^e)}}{2}\right) + \sum_e \tau_{\mathrm{M}}^e \left(\frac{\|\nabla e_p^h\|^2_{L^2(\Omega^e)}}{2\epsilon_2} + \frac{\epsilon_2 \|\nabla\eta_p\|^2_{L^2(\Omega^e)}}{2}\right) , \tag{A.12}$$

for arbitrary $\epsilon_1^e > 0$ and $\epsilon_2 > 0$. Choose $\epsilon_1^e = \tau_{\mathrm{C}}^e/2$ and $\epsilon_2 = 2$. Then terms involving the discrete errors $\mathbf{e}_u^h$ and e_p^h may be hidden behind the corresponding terms in the stability norm, and we arrive at

$$\frac{1}{2}\left|\!\left|\!\left|\{\mathbf{e}_u^h, e_p^h\}\right|\!\right|\!\right|^2 \leq \sum_e \left(\frac{\|\eta_p\|^2_{L^2(\Omega^e)}}{\tau_{\mathrm{C}}^e} + \tau_{\mathrm{M}}^e \|\nabla\eta_p\|^2_{L^2(\Omega^e)}\right) . \tag{A.13}$$

Recalling the usual asymptotic behavior of the stabilization constants (cf. [16, (16) and (17)]), let us say that

$$\tau_{\mathrm{M}}^e \sim \alpha^e \frac{h^2}{\mu} , \tag{A.14}$$

$$\tau_{\mathrm{C}}^e \sim \frac{h^2}{\tau_{\mathrm{M}}^e} \sim \frac{\mu}{\alpha^e} , \tag{A.15}$$

where $\alpha^e > 0$ is a dimensionless scalar on each element. Recalling that the stability norm bounds H^1 velocity error, we finally obtain

$$|\mathbf{u}^h|^2_{H^1(\Omega)} \leq \sum_e \frac{C\alpha^e}{\mu^2}\left(\|\eta_p\|^2_{L^2(\Omega^e)} + h^2\|\nabla\eta_p\|^2_{L^2(\Omega^e)}\right) , \tag{A.16}$$

where C is independent of α^e and h. Thus, the spurious leakage in the discrete solution can be scaled down to arbitrarily small levels by reducing α^e in elements with pressure interpolation errors. It is straightforward to see that shrinking α^e in elements with pressure interpolation errors is akin to increasing the value of s^{shell}, as defined in [16, Section 4.4.2]. This has the obvious consequence, however, of destabilizing the pressure field, and, in problems with nonzero $\mathbf{u}$, this could, based on standard PSPG error analysis [79], magnify the effects of velocity interpolation errors. We therefore feel that using div-conforming fluid discretizations is a more appealing solution to the problem of large pressure interpolation errors corrupting velocity solutions.

Appendix B. Hessian of the discrete velocity

Continuing from (40), we now derive the components of the Hessian of **u**, $u_{i,jk}$. We use the identity (cf. [73, (1.253)])

$$\frac{\partial A^{-1}_{ij}}{\partial A_{k\ell}} = -A^{-1}_{ik}A^{-1}_{\ell j}\ . \tag{B.1}$$

Proceeding again in index notation, with colors and underlines for visual clarity, we begin by applying the product rule to (40):

$$\begin{aligned} u_{i,jk} =& \left(\frac{1}{J}\right)_{,k}\left(\left(-F^{-1}_{B\ell}F_{\ell B,C}F_{iA} + F_{iA,C}\right)\hat{u}_A + F_{iA}\hat{u}_{A,C}\right)F^{-1}_{Cj} \\ &+ \frac{1}{J}\left\{\underline{\left(-F^{-1}_{B\ell}F_{\ell B,C}F_{iA} + F_{iA,C}\right)\hat{u}_A} + \underline{\underline{F_{iA}\hat{u}_{A,C}}}\right\}_{,k}F^{-1}_{Cj} \\ &+ \frac{1}{J}\left(\left(-F^{-1}_{B\ell}F_{B\ell}F_{iA} + F_{iA,C}\right)\hat{u}_A + F_{iA}\hat{u}_{A,C}\right)F^{-1}_{Cj,k}\ . \end{aligned} \tag{B.2}$$

We then expand each term, applying (39) to the term in red and the chain rule to other terms:

$$\begin{aligned} =& \left(\frac{-1}{J}F^{-1}_{Dm}F_{mD,E}F^{-1}_{Ek}\right)\left(\left(-F^{-1}_{B\ell}F_{\ell B,C}F_{iA} + F_{iA,C}\right)\hat{u}_A + F_{iA}\hat{u}_{A,C}\right)F^{-1}_{Cj} \\ &+ \frac{1}{J}\left\{\underline{\left(-F^{-1}_{B\ell,k}F_{\ell B,C}F_{iA} - F^{-1}_{B\ell}F_{\ell B,Ck}F_{iA} - F^{-1}_{B\ell}F_{\ell B,C}F_{iA,k} + F_{iA,Ck}\right)\hat{u}_A} \right. \\ & \left. \underline{+\left(-F^{-1}_{B\ell}F_{\ell B,C}F_{iA} + F_{iA,C}\right)\hat{u}_{A,D}F^{-1}_{Dk}} + \underline{\underline{F_{iA,D}F^{-1}_{Dk}\hat{u}_{A,C} + F_{iA}\hat{u}_{A,CD}F^{-1}_{Dk}}}\right\}F^{-1}_{Cj} \\ &+ \frac{1}{J}\left(\left(-F^{-1}_{B\ell}F_{\ell B,C}F_{iA} + F_{iA,C}\right)\hat{u}_A + F_{iA}\hat{u}_{A,C}\right)\frac{\partial F^{-1}_{Cj}}{\partial F_{mE}}\frac{\partial F_{mE}}{\partial x_k}\ . \end{aligned} \tag{B.3}$$

Now we apply (B.1) to the term in magenta and further expand the terms in blue using the chain rule:

$$\begin{aligned} =& \left(\frac{-1}{J}F^{-1}_{Dm}F_{mD,E}F^{-1}_{Ek}\right)\left(\left(-F^{-1}_{B\ell}F_{\ell B,C}F_{iA} + F_{iA,C}\right)\hat{u}_A + F_{iA}\hat{u}_{A,C}\right)F^{-1}_{Cj} \\ &+ \frac{1}{J}\left\{\left(-\frac{\partial F^{-1}_{B\ell}}{\partial F_{mD}}\frac{\partial F_{mD}}{\partial x_k}F_{\ell B,C}F_{iA} - F^{-1}_{B\ell}F_{\ell B,CD}F^{-1}_{Dk}F_{iA} - F^{-1}_{B\ell}F_{\ell B,C}F_{iA,D}F^{-1}_{Dk} + F_{iA,CD}F^{-1}_{Dk}\right)\hat{u}_A \right. \\ & \left. + \left(-F^{-1}_{B\ell}F_{\ell B,C}F_{iA} + F_{iA,C}\right)\hat{u}_{A,D}F^{-1}_{Dk} + F_{iA,D}F^{-1}_{Dk}\hat{u}_{A,C} + F_{iA}\hat{u}_{A,CD}F^{-1}_{Dk}\right\}F^{-1}_{Cj} \\ &+ \frac{1}{J}\left(\left(-F^{-1}_{B\ell}F_{\ell B,C}F_{iA} + F_{iA,C}\right)\hat{u}_A + F_{iA}\hat{u}_{A,C}\right)\left(-F^{-1}_{Cm}F^{-1}_{Ej}\right)F_{mE,D}F^{-1}_{Dk}\ . \end{aligned} \tag{B.4}$$

Finally, we apply (B.1) again to the first term in blue:

$$=\left(\frac{-1}{J}F^{-1}_{Dm}F_{mD,E}F^{-1}_{Ek}\right)\left(\left(-F^{-1}_{B\ell}F_{\ell B,C}F_{iA} + F_{iA,C}\right)\hat{u}_A + F_{iA}\hat{u}_{A,C}\right)F^{-1}_{Cj}$$

$$
\begin{aligned}
&+\frac{1}{J}\Big\{\Big(F^{-1}_{Bm}F^{-1}_{D\ell}F_{mD,E}F^{-1}_{Ek}F_{\ell B,C}F_{iA} - F^{-1}_{B\ell}F_{\ell B,CD}F^{-1}_{Dk}F_{iA} - F^{-1}_{B\ell}F_{\ell B,C}F_{iA,D}F^{-1}_{Dk} + F_{iA,CD}F^{-1}_{Dk}\Big)\hat{u}_A \\
&+\Big(-F^{-1}_{B\ell}F_{\ell B,C}F_{iA} + F_{iA,C}\Big)\hat{u}_{A,D}F^{-1}_{Dk} + F_{iA,D}F^{-1}_{Dk}\hat{u}_{A,C} + F_{iA}\hat{u}_{A,CD}F^{-1}_{Dk}\Big\}F^{-1}_{Cj} \\
&-\frac{1}{J}\Big(\Big(-F^{-1}_{B\ell}F_{\ell B,C}F_{iA} + F_{iA,C}\Big)\hat{u}_A + F_{iA}\hat{u}_{A,C}\Big)F^{-1}_{Cm}F^{-1}_{Ej}F_{mE,D}F^{-1}_{Dk}\,. \qquad \text{(B.5)}
\end{aligned}
$$

The expression (B.5) is in terms of derivatives of functions on the parameter space with respect to the parameters, so it is straightforward to compute all of the terms given the control point coefficients for the velocity basis functions. Note that the second derivatives of the velocity require *third* derivatives of $\boldsymbol{\phi}$.

References

[1] K. Stein, R. Benney, V. Kalro, T. E. Tezduyar, J. Leonard, and M. Accorsi. Parachute fluid–structure interactions: 3-D Computation. *Computer Methods in Applied Mechanics and Engineering*, 190:373–386, 2000.

[2] K. Takizawa and T. E. Tezduyar. Computational methods for parachute fluid–structure interactions. *Archives of Computational Methods in Engineering*, 19:125–169, 2012.

[3] K. Takizawa, B. Henicke, A. Puntel, N. Kostov, and T. E. Tezduyar. Space–time techniques for computational aerodynamics modeling of flapping wings of an actual locust. *Computational Mechanics*, 50:743–760, 2012.

[4] K. Takizawa, T. E. Tezduyar, and N. Kostov. Sequentially-coupled space–time FSI analysis of bio-inspired flapping-wing aerodynamics of an MAV. *Computational Mechanics*, 54:213–233, 2014.

[5] V. B. Makhijani, H. Q. Yang, P. J. Dionne, and M. J. Thubrikar. Three-dimensional coupled fluid–structure simulation of pericardial bioprosthetic aortic valve function. *ASAIO Journal*, 43:M387–M392, 1997.

[6] J. De Hart, G. W. M. Peters, P. J. G. Schreurs, and F. P. T. Baaijens. A three-dimensional computational analysis of fluid–structure interaction in the aortic valve. *Journal of Biomechanics*, 36:103–112, 2003.

[7] C. J. Carmody, G. Burriesci, I. C. Howard, and E. A. Patterson. An approach to the simulation of fluid–structure interaction in the aortic valve. *Journal of Biomechanics*, 39:158–169, 2006.

[8] R. van Loon, P. D. Anderson, and F. N. van de Vosse. A fluid–structure interaction method with solid-rigid contact for heart valve dynamics. *Journal of Computational Physics*, 217:806–823, 2006.

[9] M. Astorino, J.-F. Gerbeau, O. Pantz, and K.-F. Traoré. Fluid–structure interaction and multi-body contact: Application to aortic valves. *Computer Methods in Applied Mechanics and Engineering*, 198:3603–3612, 2009.

[10] R. van Loon. Towards computational modelling of aortic stenosis. *International Journal for Numerical Methods in Biomedical Engineering*, 26:405–420, 2010.

[11] S. C. Shadden, M. Astorino, and J.-F. Gerbeau. Computational analysis of an aortic valve jet with Lagrangian coherent structures. *Chaos*, 20:017512, 2010.

[12] B. E. Griffith. Immersed boundary model of aortic heart valve dynamics with physiological driving and loading conditions. *International Journal for Numerical Methods in Biomedical Engineering*, 28(3):317–345, 2012.

[13] F. Sturla, E. Votta, M. Stevanella, C. A. Conti, and A. Redaelli. Impact of modeling fluid–structure interaction in the computational analysis of aortic root biomechanics. *Medical Engineering and Physics*, 35:1721–1730, 2013.

[14] I. Borazjani. Fluid–structure interaction, immersed boundary-finite element method simulations of bio-prosthetic heart valves. *Computer Methods in Applied Mechanics and Engineering*, 257:103–116, 2013.

[15] E. Votta, T. B. Le, M. Stevanella, L. Fusini, E. G. Caiani, A. Redaelli, and F. Sotiropoulos. Toward patient-specific simulations of cardiac valves: State-of-the-art and future directions. *Journal of Biomechanics*, 46:217–228, 2013.

[16] D. Kamensky, M.-C. Hsu, D. Schillinger, J. A. Evans, A. Aggarwal, Y. Bazilevs, M. S. Sacks, and T. J. R. Hughes. An immersogeometric variational framework for fluid–structure interaction: Application to bioprosthetic heart valves. *Computer Methods in Applied Mechanics and Engineering*, 284:1005–1053, 2015.

[17] M.-C. Hsu, D. Kamensky, Y. Bazilevs, M. S. Sacks, and T. J. R. Hughes. Fluid–structure interaction analysis of bioprosthetic heart valves: significance of arterial wall deformation. *Computational Mechanics*, 54:1055–1071, 2014.

[18] M.-C. Hsu, D. Kamensky, F. Xu, J. Kiendl, C. Wang, M. C. H. Wu, J. Mineroff, A. Reali, Y. Bazilevs, and M. S. Sacks. Dynamic and fluid–structure interaction simulations of

bioprosthetic heart valves using parametric design with T-splines and Fung-type material models. *Computational Mechanics*, 55:1211–1225, 2015.

[19] A. Gilmanov, T. B. Le, and F. Sotiropoulos. A numerical approach for simulating fluid structure interaction of flexible thin shells undergoing arbitrarily large deformations in complex domains. *Journal of Computational Physics*, 300:814–843, 2015.

[20] A. Gilmanov and F. Sotiropoulos. Comparative hemodynamics in an aorta with bicuspid and trileaflet valves. *Theoretical and Computational Fluid Dynamics*, 30(1):67–85, 2016.

[21] W. Wu, D. Pott, B. Mazza, T. Sironi, E. Dordoni, C. Chiastra, L. Petrini, G. Pennati, G. Dubini, U. Steinseifer, S. Sonntag, M. Kuetting, and F. Migliavacca. Fluid–structure interaction model of a percutaneous aortic valve: Comparison with an in vitro test and feasibility study in a patient-specific case. *Annals of Biomedical Engineering*, 44(2):590–603, 2016.

[22] G. Marom. Numerical methods for fluid–structure interaction models of aortic valves. *Archives of Computational Methods in Engineering*, 22(4):595–620, 2014.

[23] D. Kamensky, J. A. Evans, and M.-C. Hsu. Stability and conservation properties of collocated constraints in immersogeometric fluid-thin structure interaction analysis. *Communications in Computational Physics*, 18:1147–1180, 2015.

[24] L. Piegl and W. Tiller. *The NURBS Book (Monographs in Visual Communication), 2nd ed.* Springer-Verlag, New York, 1997.

[25] T. J. R. Hughes, J. A. Cottrell, and Y. Bazilevs. Isogeometric analysis: CAD, finite elements, NURBS, exact geometry and mesh refinement. *Computer Methods in Applied Mechanics and Engineering*, 194:4135–4195, 2005.

[26] D. Schillinger, L. Dedè, M. A. Scott, J. A. Evans, M. J. Borden, E. Rank, and T. J. R. Hughes. An isogeometric design-through-analysis methodology based on adaptive hierarchical refinement of NURBS, immersed boundary methods, and T-spline CAD surfaces. *Computer Methods in Applied Mechanics and Engineering*, 249–252:116–150, 2012.

[27] M. Breitenberger, A. Apostolatos, B. Philipp, R. Wüchner, and K.-U. Bletzinger. Analysis in computer aided design: Nonlinear isogeometric B-Rep analysis of shell structures. *Computer Methods in Applied Mechanics and Engineering*, 284:401–457, 2015.

[28] M.-C. Hsu, C. Wang, A. J. Herrema, D. Schillinger, A. Ghoshal, and Y. Bazilevs. An interactive geometry modeling and parametric design platform for isogeometric analysis. *Computers and Mathematics with Applications*, 70:1481–1500, 2015.

[29] J. A. Cottrell, A. Reali, Y. Bazilevs, and T. J. R. Hughes. Isogeometric analysis of structural vibrations. *Computer Methods in Applied Mechanics and Engineering*, 195:5257–5297, 2006.

[30] J. A. Cottrell, T. J. R. Hughes, and A. Reali. Studies of refinement and continuity in isogeometric structural analysis. *Computer Methods in Applied Mechanics and Engineering*, 196:4160–4183, 2007.

[31] J. A. Cottrell, T. J. R. Hughes, and Y. Bazilevs. *Isogeometric Analysis: Toward Integration of CAD and FEA*. Wiley, Chichester, 2009.

[32] D. J. Benson, Y. Bazilevs, M.-C. Hsu, and T. J. R. Hughes. Isogeometric shell analysis: The Reissner–Mindlin shell. *Computer Methods in Applied Mechanics and Engineering*, 199:276–289, 2010.

[33] S. Morganti, F. Auricchio, D. J. Benson, F. I. Gambarin, S. Hartmann, T. J. R. Hughes, and A. Reali. Patient-specific isogeometric structural analysis of aortic valve closure. *Computer Methods in Applied Mechanics and Engineering*, 284:508–520, 2015.

[34] Y. Bazilevs and T. J. R. Hughes. NURBS-based isogeometric analysis for the computation of flows about rotating components. *Computational Mechanics*, 43:143–150, 2008.

[35] Y. Bazilevs and I. Akkerman. Large eddy simulation of turbulent Taylor–Couette flow using isogeometric analysis and the residual–based variational multiscale method. *Journal of Computational Physics*, 229:3402–3414, 2010.

[36] J. A. Evans and T. J. R. Hughes. Isogeometric divergence-conforming B-splines for the unsteady Navier–Stokes equations. *Journal of Computational Physics*, 241:141–167, 2013.

[37] L. De Lorenzis, İ. Temizer, P. Wriggers, and G. Zavarise. A large deformation frictional contact formulation using NURBS-based isogeometric analysis. *International Journal for Numerical Methods in Engineering*, 87:1278–1300, 2011.

[38] İ. Temizer, P. Wriggers, and T. J. R. Hughes. Three-dimensional mortar-based frictional contact treatment in isogeometric analysis with NURBS. *Computer Methods in Applied Mechanics and Engineering*, 209-212:115–128, 2012.

[39] L. De Lorenzis, P. Wriggers, and T. J. R. Hughes. Isogeometric contact: a review. *GAMM-Mitteilungen*, 37(1):85–123, 2014.

[40] J. Kiendl, K.-U. Bletzinger, J. Linhard, and R. Wüchner. Isogeometric shell analysis with Kirchhoff–Love elements. *Computer Methods in Applied Mechanics and Engineering*, 198:3902–3914, 2009.

[41] J. Kiendl, Y. Bazilevs, M.-C. Hsu, R. Wüchner, and K.-U. Bletzinger. The bending strip method for isogeometric analysis of Kirchhoff–Love shell structures comprised of multiple patches. *Computer Methods in Applied Mechanics and Engineering*, 199:2403–2416, 2010.

[42] J. Kiendl. *Isogeometric Analysis and Shape Optimal Design of Shell Structures*. PhD thesis, Lehrstuhl für Statik, Technische Universität München, 2011.

[43] D. J. Benson, Y. Bazilevs, M.-C. Hsu, and T. J. R. Hughes. A large deformation, rotation-free, isogeometric shell. *Computer Methods in Applied Mechanics and Engineering*, 200:1367–1378, 2011.

[44] E. Rank, M. Ruess, S. Kollmannsberger, D. Schillinger, and A. Düster. Geometric modeling, isogeometric analysis and the finite cell method. *Computer Methods in Applied Mechanics and Engineering*, 249-252:104–115, 2012.

[45] M. Ruess, D. Schillinger, Y. Bazilevs, V. Varduhn, and E. Rank. Weakly enforced essential boundary conditions for NURBS-embedded and trimmed NURBS geometries on the basis of the finite cell method. *International Journal for Numerical Methods in Engineering*, 95:811–846, 2013.

[46] D. Schillinger and M. Ruess. The Finite Cell Method: A review in the context of higher-order structural analysis of CAD and image-based geometric models. *Archives of Computational Methods in Engineering*, 22(3):391–455, 2015.

[47] C. A. Taylor, T. J. R. Hughes, and C. K. Zarins. Finite element modeling of blood flow in arteries. *Computer Methods in Applied Mechanics and Engineering*, 158:155–196, 1998.

[48] C. A. Taylor, T. J. R. Hughes, and C. K. Zarins. Finite element modeling of three-dimensional pulsatile flow in the abdominal aorta: relevance to atherosclerosis. *Annals of Biomedical Engineering*, 158:975–987, 1998.

[49] C. A. Taylor, T. J. R. Hughes, and C. K. Zarins. Effect of excercise on hemodynamic conditions in the abdominal aorta. *Journal of Vascular Surgery*, 29:1077–1089, 1999.

[50] H. Lan, J. Merkow, A. Updegrove, D. Schiavazzi, N. Wilson, S. Shadden, and A. Marsden. Simvascular 2.0: an integrated open source pipeline for image-based cardiovascular modeling and simulation. In *Proceedings of the 68th Annual Meeting of the APS Division of Fluid Dynamics*. American Physical Society, 2015.

[51] SimVascular. http://simvascular.github.io/. Accessed 30 April 2016.

[52] R. Khlebnikov and C. A. Figueroa. CRIMSON: Towards a software environment for patient-specific blood flow simulation for diagnosis and treatment. In C. Oyarzun Laura, R. Shekhar, S. Wesarg, M. A. González Ballester, K. Drechsler, Y. Sato, M. Erdt, and G. M. Linguraru, editors, *Clinical Image-Based Procedures: Translational Research in Medical Imaging*, pages 10–18. Springer International Publishing, Switzerland, 2016.

[53] CRIMSON. http://www.crimson.software/. Accessed 30 April 2016.

[54] C. K. Zarins, C. A. Taylor, and J. K. Min. Computed fractional flow reserve (FFTCT) derived from coronary CT angiography. *Journal of Cardiovascular Translational Research*, 6(5):708–714, 2013.

[55] Heartflow. http://www.heartflow.com/. Accessed 30 April 2016.

[56] A. Figueroa, I. E. Vignon-Clementel, K. E. Jansen, T. J. R. Hughes, and C. A. Taylor. A coupled momentum method for modeling blood flow in three-dimensional deformable arteries. *Computer Methods in Applied Mechanics and Engineering*, 195:5685–5706, 2006.

[57] K. Takizawa, Y. Bazilevs, and T. E. Tezduyar. Space–time and ALE-VMS techniques for patient-specific cardiovascular fluid–structure interaction modeling. *Archives of Computational Methods in Engineering*, 19:171–225, 2012.

[58] I. E. Vignon-Clementel, C. A. Figueroa, K. E. Jansen, and C. A. Taylor. Outflow boundary conditions for three-dimensional finite element modeling of blood flow and pressure in arteries. *Computer Methods in Applied Mechanics and Engineering*, 195:3776–3796, 2006.

[59] M. Esmaily-Moghadam, Y. Bazilevs, T.-Y. Hsia, I. E. Vignon-Clementel, A. L. Marsden, and Modeling of Congenital Hearts Alliance (MOCHA). A comparison of outlet boundary treatments for prevention of backflow divergence with relevance to blood flow simulations. *Computational Mechanics*, 48:277–291, 2011.

[60] A. L. Marsden, J. A. Feinstein, and C. A. Taylor. A computational framework for derivative-free optimization of cardiovascular geometries. *Computer Methods in Applied Mechanics and Engineering*, 197:1890–1905, 2008.

[61] C. S. Peskin and B. F. Printz. Improved volume conservation in the computation of flows with immersed elastic boundaries. *Journal of Computational Physics*, 105(1):33–46, 1993.

[62] K. J. Galvin, A. Linke, L. G. Rebholz, and N. E. Wilson. Stabilizing poor mass conservation in incompressible flow problems with large irrotational forcing and application to thermal convection. *Computer Methods in Applied Mechanics and Engineering*, 237–240:166–176, 2012.

[63] M. A. Case, V. J. Ervin, A. Linke, and L. G. Rebholz. A connection between Scott–Vogelius and grad–div stabilized Taylor–Hood FE approximations of the Navier–Stokes equations. *SIAM Journal on Numerical Analysis*, 49(1):1461–1481, 2011.

[64] L. R. Scott and M. Vogelius. Norm estimates for a maximal right inverse of the divergence operator in spaces of piecewise polynomials. *ESAIM: Mathematical Modelling and Numerical Analysis*, 19(1):111–143, 1985.

[65] D. N. Arnold, R. S. Falk, and R. Winther. Finite element exterior calculus, homological techniques, and applications. *Acta Numerica*, 15:1–155, 2006.

[66] J. A. Evans. *Divergence-free B-spline Discretizations for Viscous Incompressible Flows*. Ph.D. thesis, University of Texas at Austin, Austin, Texas, United States, 2011.

[67] J. A. Evans and T. J. R. Hughes. Isogeometric divergence-conforming B-splines for the steady Navier–Stokes equations. *Mathematical Models and Methods in Applied Sciences*, 23(08):1421–1478, 2013.

[68] Y. Bazilevs, M.-C. Hsu, and M. A. Scott. Isogeometric fluid–structure interaction analysis with emphasis on non-matching discretizations, and with application to wind turbines. *Computer Methods in Applied Mechanics and Engineering*, 249–252:28–41, 2012.

[69] J. Kiendl, M.-C. Hsu, M. C. H. Wu, and A. Reali. Isogeometric Kirchhoff–Love shell formulations for general hyperelastic materials. *Computer Methods in Applied Mechanics and Engineering*, 291:280–303, 2015.

[70] Y. Bazilevs, K. Takizawa, and T. E. Tezduyar. *Computational Fluid–Structure Interaction: Methods and Applications*. Wiley, Chichester, 2013.

[71] M. Bischoff, W. A. Wall, K.-U. Bletzinger, and E. Ramm. Models and finite elements for thin-walled structures. In E. Stein, R. de Borst, and T. J. R. Hughes, editors, *Encyclopedia of Computational Mechanics*, Volume 3: Solids and Structures, chapter 3. John Wiley & Sons, 2004.

[72] A. Buganza Tepole, H. Kabaria, K.-U. Bletzinger, and E. Kuhl. Isogeometric Kirchhoff–Love shell formulations for biological membranes. *Computer Methods in Applied Mechanics and Engineering*, 293:328–347, 2015.

[73] G. A. Holzapfel. *Nonlinear Solid Mechanics: A Continuum Approach for Engineering*. Wiley, Chichester, 2000.

[74] R. Fan and M. S. Sacks. Simulation of planar soft tissues using a structural constitutive model: Finite element implementation and validation. *Journal of Biomechanics*, 47(9):2043–2054, 2014.

[75] A. Buffa, G. Sangalli, and R. Vázquez. Isogeometric analysis in electromagnetics: B-splines approximation. *Computer Methods in Applied Mechanics and Engineering*, 199(17–20):1143–1152, 2010.

[76] A. Buffa, J. Rivas, G. Sangalli, and R. Vásquez. Isogeometric discrete differential forms in three dimensions. *SIAM Journal on Numerical Analysis*, 49(2):814–844, 2011.

[77] D. N. Arnold, D. Boffi, and R. S. Falk. Quadrilateral $H(\mathrm{div})$ finite elements. *SIAM Journal on Numerical Analysis*, 42(6):2429–2451, 2005.

[78] A. N. Brooks and T. J. R. Hughes. Streamline upwind/Petrov-Galerkin formulations for convection dominated flows with particular emphasis on the incompressible Navier-Stokes equations. *Computer Methods in Applied Mechanics and Engineering*, 32:199–259, 1982.

[79] T. J. R. Hughes, L. P. Franca, and M. Balestra. A new finite element formulation for computational fluid dynamics: V. Circumventing the Babuška–Brezzi condition: A stable Petrov–Galerkin formulation of the Stokes problem accommodating equal-order interpolations. *Computer Methods in Applied Mechanics and Engineering*, 59:85–99, 1986.

[80] R. A. Adams. *Sobolev Spaces*. Academic Press, New York, 1975.

[81] A. Düster, J. Parvizian, Z. Yang, and E. Rank. The finite cell method for three-dimensional problems of solid mechanics. *Computer Methods in Applied Mechanics and Engineering*, 197(45–48):3768–3782, 2008.

[82] G. Strang and G. J. Fix. *An Analysis of the Finite Element Method*. Prentice-Hall, Englewood Cliffs, New Jersey, 1973.

[83] A. Stavrev. The role of higher-order geometry approximation and accurate quadrature in nurbs based immersed boundary methods. Master's thesis, Technische Universität München, Munich, Germany, 2012.

[84] M.-C. Hsu, C. Wang, F. Xu, A. J. Herrema, and A. Krishnamurthy. Direct immersogeometric fluid flow analysis using B-rep CAD models. *Computer Aided Geometric Design*, 43:143–158, 2016.

[85] D. Schillinger, I. Harari, M.-C. Hsu, D. Kamensky, K.F.S. Stoter, Y. Yu, and Y. Zhao. The non-symmetric Nitsche method for the parameter-free coupling imposition of weak boundary and coupling conditions in immersed finite elements. *Computer Methods in Applied Mechanics and Engineering*, 2016. Submitted.

[86] Y. Bazilevs and T. J. R. Hughes. Weak imposition of Dirichlet boundary conditions in fluid mechanics. *Computers and Fluids*, 36:12–26, 2007.

[87] Y. Bazilevs, C. Michler, V. M. Calo, and T. J. R. Hughes. Weak Dirichlet boundary conditions for wall-bounded turbulent flows. *Computer Methods in Applied Mechanics and Engineering*, 196:4853–4862, 2007.

[88] Y. Bazilevs, C. Michler, V. M. Calo, and T. J. R. Hughes. Isogeometric variational multiscale modeling of wall-bounded turbulent flows with weakly enforced boundary conditions on unstretched meshes. *Computer Methods in Applied Mechanics and Engineering*, 199:780–790, 2010.

[89] M.-C. Hsu, I. Akkerman, and Y. Bazilevs. Wind turbine aerodynamics using ALE–VMS: Validation and the role of weakly enforced boundary conditions. *Computational Mechanics*, 50:499–511, 2012.

[90] J. Nitsche. Über ein Variationsprinzip zur Lösung von Dirichlet-Problemen bei Verwendung von Teilräumen, die keinen Randbedingungen unterworfen sind. *Abhandlungen aus dem Mathematischen Seminar der Universität Hamburg*, 36:9–15, 1971.

[91] J. C. Simo, P. Wriggers, and R. L. Taylor. A perturbed Lagrangian formulation for the finite element solution of contact problems. *Computer Methods in Applied Mechanics and Engineering*, 50(2):163–180, 1985.

[92] H. J. C. Barbosa and T. J. R. Hughes. The finite element method with Lagrange multipliers on the boundary: circumventing the Babuška-Brezzi condition. *Computer Methods in Applied Mechanics and Engineering*, 85(1):109–128, 1991.

[93] J. Chung and G. M. Hulbert. A time integration algorithm for structural dynamics with improved numerical dissipation: The generalized-α method. *Journal of Applied Mechanics*, 60:371–75, 1993.

[94] Y. Bazilevs, V. M. Calo, T. J. R. Hughes, and Y. Zhang. Isogeometric fluid–structure interaction: theory, algorithms, and computations. *Computational Mechanics*, 43:3–37, 2008.

[95] K. E. Jansen, C. H. Whiting, and G. M. Hulbert. A generalized-α method for integrating the filtered Navier–Stokes equations with a stabilized finite element method. *Computer Methods in Applied Mechanics and Engineering*, 190:305–319, 2000.

[96] M. R. Hestenes. Multiplier and gradient methods. *Journal of Optimization Theory and Applications*, 4(5):303–320, 1969.

[97] M. J. D. Powell. A method for nonlinear constraints in minimization problems. In R. Fletcher, editor, *Optimization*, pages 283–298. Academic Press, New York, 1969.

[98] H. Uzawa. Iterative methods for concave programming. In K.J. Arrow, L. Hurwicz, and H. Uzawa, editors, *Studies in Linear and Non-Linear Programming*, chapter 10, pages 154–165. Stanford University Press, Stanford, California, 1958.

[99] C. Bacuta. A unified approach for Uzawa algorithms. *SIAM Journal on Numerical Analysis*, 44(6):2633–2649, 2006.

[100] E. H. van Brummelen. Added mass effects of compressible and incompressible flows in fluid–structure interaction. *Journal of Applied Mechanics*, 76:021206, 2009.

[101] S. Balay, S. Abhyankar, M. F. Adams, J. Brown, P. Brune, K. Buschelman, L. Dalcin, V. Eijkhout, W. D. Gropp, D. Kaushik, M. G. Knepley, L. C. McInnes, K. Rupp, B. F. Smith, S. Zampini, and H. Zhang. PETSc Web page. http://www.mcs.anl.gov/petsc, 2015.

[102] S. Balay, S. Abhyankar, M. F. Adams, J. Brown, P. Brune, K. Buschelman, L. Dalcin, V. Eijkhout, W. D. Gropp, D. Kaushik, M. G. Knepley, L. C. McInnes, K. Rupp, B. F. Smith, S. Zampini, and H. Zhang. PETSc users manual. Technical Report ANL-95/11 - Revision 3.6, Argonne National Laboratory, 2015.

[103] S. Balay, W. D. Gropp, L. C. McInnes, and B. F. Smith. Efficient management of parallelism in object oriented numerical software libraries. In E. Arge, A. M. Bruaset, and H. P. Langtangen, editors, *Modern Software Tools in Scientific Computing*, pages 163–202. Birkhäuser Press, 1997.

[104] M. R. Hestenes and E. Stiefel. Methods of conjugate gradients for solving linear systems. *Journal of Research of the National Bureau of Standards*, 49(6):409–436, 1952.

[105] D. Goldstein, R. Handler, and L. Sirovich. Modeling a no-slip flow boundary with an external force field. *Journal of Computational Physics*, 105(2):354–366, 1993.

[106] J. Kim, P. Moin, and R. Moser. Turbulence statistics in fully developed channel flow at low Reynolds number. *Journal of Fluid Mechanics*, 177:133–166, 1987.

[107] L. B. Wahlbin. Local behavior in finite element methods. In P. G. Ciarlet and J. L. Lions, editors, *Finite Element Methods (Part 1)*, volume 2 of *Handbook of Numerical Analysis*, pages 353–522. North-Holland, 1991.

[108] D. B. Goldstein and T.-C. Tuan. Secondary flow induced by riblets. *Journal of Fluid Mechanics*, 363:115–151, 1998.

[109] K. Stephani and D. Goldstein. DNS study of transient disturbance growth and bypass transition due to realistic roughness. In *Proceedings of 47th AIAA Aerospace Sciences Meeting including The New Horizons Forum and Aerospace Exposition*, AIAA Paper 2009-585, Orlando, Florida, 2009.

[110] J. S. Strand and D. B. Goldstein. Direct numerical simulations of riblets to constrain the growth of turbulent spots. *Journal of Fluid Mechanics*, 668:267–292, 2011.

[111] C. J. Doolittle, S. D. Drews, and D. B. Goldstein. Near-field flow structures about subcritical surface roughness. *Physics of Fluids*, 26:124106, 2014.

[112] E. M. Saiki and S. Biringen. Numerical simulation of a cylinder in uniform flow: Application of a virtual boundary method. *Journal of Computational Physics*, 123(2):450–465, 1996.

[113] E. M. Saiki and S. Biringen. Spatial numerical simulation of boundary layer transition: effects of a spherical particle. *Journal of Fluid Mechanics*, 345:133–164, 1997.

[114] W.-X. Huang, S. J. Shin, and H. J. Sung. Simulation of flexible filaments in a uniform flow by the immersed boundary method. *Journal of Computational Physics*, 226(2):2206–2228, 2007.

[115] S. J. Shin, W.-X. Huang, and H. J. Sung. Assessment of regularized delta functions and feedback forcing schemes for an immersed boundary method. *International Journal for Numerical Methods in Fluids*, 58(3):263–286, 2008.

[116] W.-X. Huang and H. J. Sung. An immersed boundary method for fluid–flexible structure interaction. *Computer Methods in Applied Mechanics and Engineering*, 198(33–36):2650–2661, 2009.

[117] J. Ryu, S. G. Park, B. Kim, and H. J. Sung. Flapping dynamics of an inverted flag in a uniform flow. *Journal of Fluids and Structures*, 57:159–169, 2015.

[118] E. Uddin, W.-X. Huang, and H. J. Sung. Actively flapping tandem flexible flags in a viscous flow. *Journal of Fluid Mechanics*, 780:120–142, 10 2015.

[119] LS-DYNA Finite Element Software: Livermore Software Technology Corp. http://www.lstc.com/products/ls-dyna. Accessed 30 April 2016.

[120] M. Souli, Y. Sofiane, and L. Olovsson. ALE and fluid/structure interaction in LS-DYNA. In *Proceedings of Emerging Technology in Fluids, Structures, and Fluid–Structure Interactions*. ASME, 2004.

[121] M. Souli, N. Capron, and U. Khan. Fluid structure interaction and airbag ALE for out of position. In *Proceedings of the ASME Pressure Vessels and Piping Conference*. AMSE, 2005.

[122] M. Souli, J. Wang, I. Do, and C. Hao. ALE and fluid structure interaction in LS-DYNA. In *Proceedings of the 8th International LS-DYNA Users Conference*, 2011.

[123] A. Haufe, K. Weimar, and U. Göhner. Advanced airbag simulation using fluid-structure-interaction and the Eluerian method in LS-DYNA. In *Proceedings of the LS-DYNA Anwenderforum*, 2004.

[124] G. G. Chew, I. C. Howard, and E. A. Patterson. Simulation of damage in a porcine prosthetic heart valve. *Journal of Medical Engineering & Technology*, 23(5):178–189, 1999.

[125] C. Lee. Stability characteristics of the virtual boundary method in three-dimensional applications. *Journal of Computational Physics*, 184(2):559–591, 2003.

[126] L. C. Evans. *Partial Differential Equations (Graduate Studies in Mathematics, Vol. 19)*. American Mathematical Society, Providence, Rhode Island, 2002.

[127] J.-L. Guermond and P. Minev. High-order time stepping for the incompressible Navier–Stokes equations. *SIAM Journal on Scientific Computing*, 37(6):A2656–A2681, 2015.

[128] J. Shen. On error estimates of the penalty method for unsteady Navier–Stokes equations. *SIAM Journal on Numerical Analysis*, 32(2):386–403, 1995.

[129] J. L. Guermond and J. Shen. Velocity-correction projection methods for incompressible flows. *SIAM Journal on Numerical Analysis*, 41(1):112–134, 2003.

[130] I. Ramière. Convergence analysis of the Q1-finite element method for elliptic problems with non-boundary-fitted meshes. *International Journal for Numerical Methods in Engineering*, 75(9):1007–1052, 2008.

[131] B. Kallemov, A. P. S. Bhalla, B. E. Griffith, and A. Donev. An immersed boundary method for rigid bodies. *Communications in Applied Mathematics and Computational Science*, 11(1):79–141, 2016.

[132] D. Boffi, F. Brezzi, and M. Fortin. Finite elements for the Stokes problem. In D. Boffi and L. Gastaldi, editors, *Mixed Finite Elements, Compatibility Conditions, and Applications*, Lecture Notes in Mathematics, pages 45–100. Springer-Verlag Berlin Heidelberg, 2008.

[133] T. E. Tezduyar, S. Sathe, R. Keedy, and K. Stein. Space–time finite element techniques for computation of fluid–structure interactions. *Computer Methods in Applied Mechanics and Engineering*, 195:2002–2027, 2006.

[134] C. Hesch, A. J. Gil, A. Arranz Carreño, and J. Bonet. On continuum immersed strategies for fluid-structure interaction. *Computer Methods in Applied Mechanics and Engineering*, 247-248:51–64, 2012.

[135] A.J. Gil, A. Arranz Carreño, J. Bonet, and O. Hassan. An enhanced immersed structural potential method for fluid–structure interaction. *Journal of Computational Physics*, 250:178–205, 2013.

[136] T. Wick. Flapping and contact FSI computations with the fluid–solid interface-tracking/interface-capturing technique and mesh adaptivity. *Computational Mechanics*, 53(1):29–43, 2014.

[137] C. Kadapa, W. G. Dettmer, and D. Perić. A fictitious domain/distributed Lagrange multiplier based fluid–structure interaction scheme with hierarchical B-spline grids. *Computer Methods in Applied Mechanics and Engineering*, 301:1–27, 2016.

[138] MUMPS: a MUltifrontal Massively Parallel sparse direct Solver. http://mumps.enseeiht.fr/. Accessed 24 April 2016.

[139] T. J. R. Hughes, A. Reali, and G. Sangalli. Efficient quadrature for NURBS-based isogeometric analysis. *Computer Methods in Applied Mechanics and Engineering*, 199:301–313, 2010.

[140] I. Babuška and J. T. Oden. Verification and validation in computational engineering and science: basic concepts. *Computer Methods in Applied Mechanics and Engineering*, 193(36–38):4057–4066, 2004.

[141] D. K. Hildebrand. Design and evaluation of a novel pulsatile bioreactor for biologically active heart valves. Master's thesis, University of Pittsburgh, Pittsburgh, United States, 2003.

[142] A. K. S. Iyengar, H. Sugimoto, D. B. Smith, and M. S. Sacks. Dynamic in vitro quantification of bioprosthetic heart valve leaflet motion using structured light projection. *Annals of Biomedical Engineering*, 29(11):963–973, 2001.

[143] R. Hiptmair. Multigrid method for H(div) in three dimensions. *Electronic Transactions on Numerical Analysis*, 6:133–152, 1997.

[144] G. Kanschat and Mao Y. Multigrid methods for h(div)-conforming discontinuous Galerkin methods for the Stokes equations. *Journal of Numerical Mathematics*, 23(1):51–66, 2015.

[145] T. M. van Opstal, J. Yan, C. Coley, J. A. Evans, T. Kvamsdal, and Y. Bazilevs. Isogeometric divergence-conforming variational multiscale formulation of incompressible turbulent flows. *Computer Methods in Applied Mechanics and Engineering*, 2016. Submitted.

[146] Y. Bazilevs, V. M. Calo, J. A. Cottrel, T. J. R. Hughes, A. Reali, and G. Scovazzi. Variational multiscale residual-based turbulence modeling for large eddy simulation of incompressible flows. *Computer Methods in Applied Mechanics and Engineering*, 197:173–201, 2007.

[147] J. A. Evans. The method of subgrid vortices: an isogeometric structure-preserving approach to variational multiscale modeling of turbulence. In *Proceedings of the 18th International Conference on Finite Elements in Flow Problems*, Taipei, Taiwan, 2015.

[148] K. A. Johannessen, M. Kumar, and T. Kvamsdal. Divergence-conforming discretization for Stokes problem on locally refined meshes using LR B-splines. *Computer Methods in Applied Mechanics and Engineering*, 293:38–70, 2015.

[149] K. A. Johannessen, T. Kvamsdal, and T. Dokken. Isogeometric analysis using LR b-splines. *Computer Methods in Applied Mechanics and Engineering*, 269:471–514, 2014.

[150] P. Hansbo and A. Szepessy. A velocity-pressure streamline diffusion finite element method for the incompressible Navier–Stokes equations. *Computer Methods in Applied Mechanics and Engineering*, 84:175–192, 1990.